

**UNIVERSITÀ DEGLI STUDI DI NAPOLI
FEDERICO II**



DIPARTIMENTO DI INGEGNERIA INDUSTRIALE

Dottorato di Ricerca in Ingegneria Aerospaziale, Navale e della Qualità

**THE PROBLEM OF THE VERIFICATION AND VALIDATION
PROCESSES OF CFD SIMULATIONS OF PLANING HULLS**

Simone Mancini

Tutor

Prof. Ing. Claudio Pensa

Coordinatore

Prof. Ing. Luigi De Luca

XXVIII Ciclo

All models are wrong, but some are useful

George BOX

Page Left Intentionally Blank

THE PROBLEM OF THE VERIFICATION AND VALIDATION PROCESSES OF CFD SIMULATIONS OF PLANING HULLS

simone.mancini@unina.it

Department of Industrial Engineering, University of Naples Federico II, P.le V. Tecchio n. 80, 80125 Napoli (ITALY)

ABSTRACT

In the context of Computational Fluid Dynamic (CFD) application in ship hydrodynamic field it is well known that the numerical simulations of planing crafts are significantly less reliable rather displacement hulls. For this reason it is important to perform a comprehensive approach to the verification and validation (V&V) methodologies and procedures in order to obtain high-quality results of CFD simulations of planing hulls.

In the first stage of this work, an assessment of the accuracy and effectiveness of different simulations setups and techniques for planing craft is performed, paying particular attention to the different techniques of moving mesh, such as the single moving grid, overset/chimera grid, and morphing mesh, and to the problems related to the air-water interface models, such as the *numerical ventilation* of the hull bottom.

In the second stage the results of the V&V study for four different hull models are reported at four Froude numbers (Fr). The Unsteady Reynolds Average Navier Stokes (URANS) code results are validated using benchmark experimental data obtained for three warped hulls, characterized by systematic variation of the slenderness ratio (L/B) and for one monohedral hull with comparable L/B .

Grid independence, iteration, time-step, and statistical convergence analysis for response variables (resistance coefficients, wetted surfaces, and dynamic trim angles) are performed using the main uncertainty estimation methods available in the literature. The same procedures are repeated for the wave profiles analysis.

The results of this work show that is possible to improve the reliability of the numerical simulation of the planing craft reducing the errors and uncertainties related to the predictions of resistance, running attitude and wave pattern. It should be note that the error has a significant hull geometry dependency. Moreover the results of the V&V study highlight that the sources of errors investigated have different importance on the numerical error and uncertainty and the modelling of the physics of the planing craft is a critical point to improve the reliability of the numerical simulation.

Keywords: CFD, planing craft simulation, verification & validation, overset grid, (U)RANS simulations, ship hydrodynamics

CONTENTS

ABSTRACT	4
INTRODUCTION.....	6
THE VERIFICATION AND VALIDATION PROCESS	8
1. Introduction	8
2. Sources of error and uncertainty	8
3. Uncertainty analysis methods	10
4. Deterministic methods	10
5. Probabilistic methods	11
a. Statistical methods	12
MC Methods	12
Latin Hypercube Sampling (LHS).....	13
Stochastic Collocation (SC)	13
b. Non-statistical methods	14
Moment Methods	14
Spectral Methods.....	14
6. Solution verification methodology in ship hydrodynamics.....	15
7. Verification procedures	16
a. Generalized Richardson Extrapolation (RE) method	17
b. Observed order of accuracy	18
8. Methods for uncertainty estimation	18
a. The Grid Convergence Index (GCI) method.....	19
b. The Correction Factor (CF) method.....	19
c. The Modified GCI method	20
d. Least Square Root (LSR) – GCI Method.....	20
9. Verification procedure for iterative convergence.....	22
10. Solution validation.....	22
PHYSICAL MODEL OF PLANING HULL	24
1. Resistance model of the planing hulls.....	24
2. CFD application on planing hull: literature overview	27
BENCHMARK EXPERIMENTAL DATA	30
1. The Naples warped hard chine systematic series (NSS)	30
2. The systematic series of DIN (SS-DIN)	33

NUMERICAL METHODS	35
1. Governing Equations	35
2. Spatial discretization schemes	36
3. The Finite Volume Method (FVM)	37
4. Pressure-velocity coupling method.....	38
5. Temporal discretization schemes.....	39
6. The Free Surface Models.....	40
a. VOF discretization schemes	41
b. Normalized Variable Diagram (NVD).....	42
c. HRIC scheme	44
7. The Numerical Ventilation problem	45
8. The Rigid body motion.....	46
9. Dynamic meshing.....	47
a. Moving grid.....	47
b. Overset/Chimera grid method.....	49
c. Smoothing/Morphing mesh	51
MODELING ANALYSIS	54
1. Introduction	54
2. Response variables	54
3. Moving meshes technique analysis.....	55
4. Computational domain and boundary condition	56
a. Moving Grid	56
b. Morphing grid.....	56
c. Overset/Chimera grid	57
5. A detail: the design of the grid refinement of air-water interface	59
6. Physics modeling, time-step and coordinate system	60
7. Results of moving meshes technique analysis	61
a. Interpolation schemes	63
b. VOF Schemes.....	64
c. Turbulence Model Analysis.....	67
8. Summary of modeling analysis results	68
NUMERICAL ANALYSIS.....	69
1. Introduction	69
2. Iterative convergence analysis	70
3. Time-step convergence analysis	71

4. Grid independence analysis	72
5. Statistical convergence analysis.....	75
6. Response variables validation.....	77
7. Summary of numerical analysis results	78
WAVE PROFILE V&V	80
1. Introduction	80
2. Estimating uncertainties for point-variables	80
3. Wave cut V&V for C1 model.....	81
4. Wake refinement extension	84
FURTHER ANALYSIS	86
1. Morphing mesh-grid independence analysis.....	86
2. Monohedral hull (SS-DIN).....	88
a. Grid independence analysis	89
b. MONO vs C5.....	90
CONCLUSIONS	92
APPENDIX A: Time-step convergence analysis results	94
APPENDIX B: Grid independence analysis and Validation results	95
APPENDIX C: C1 model – wave pattern comparison	98
APPENDIX D: Grid independence analysis - percentage error between CFD and EFD data	99
APPENDIX E: Visualization of streamlines and pressure on the hull bottom.....	100
APPENDIX F: Summary of calm water resistance, sinkage and trim CFD V&V studies	102
REFERENCES.....	103
FIGURES INDEX.....	111
TABLE INDEX	114
ACRONYMS	115
NOMENCLATURE.....	117
ACKNOWLEDGEMENTS	120

Page Left Intentionally Blank

Page Left Intentionally Blank

1

INTRODUCTION

Nowadays the Computational Fluid Dynamics (CFD) is widely used in all engineering field. However the application of CFD modeling as an engineering tool can be justified only on the basis of its accuracy and the level of confidence in its results. The CFD development was initially focused on new functionality and improved understanding without the need to make very precise statements relating to confidence levels. However engineering industry usually works within limitations of the current state of knowledge, as long the confidence limits are known. Hence the assessment of uncertainty in experimental data, for example, is a well-established practice, and the relevant techniques form part of every engineer's basic education.

In the CFD analysis a widespread practice is compute the solution on a single simulation, neglecting the analysis of the reliability of the results. However this practice does not result in an accurate analysis. Therefore all practical CFD models are known only at a certain level of accuracy and the reliability of the CFD analysis reduces when uncertainties and errors are neglected. Once it is recognized that errors and uncertainty are unavoidable aspects of CFD modeling, it is necessary to establish rigorous procedures to quantify the level of confidence of the results. These procedures are the verification and validation (V&V) processes. The process of verification involves quantification of the errors and the process of validation involves quantification of the input uncertainty and physical model uncertainty.

As for the other engineering fields, the CFD for ship hydrodynamics in just over 20 years has surpassed all expectations in reaching significant progress and capabilities. The hull resistance prediction is the oldest application of CFD in ship hydrodynamics and in these years many simulations are carried out for a wide range of applications and conditions. Other than drag, sinkage and trim, local flow fields such as boundary layer and wake, and wave patterns are also predicted. Different geometries including tankers, container ships, surface combatants, and small vessels are studied at a range of very small to large Fr .

The accuracy of hull resistance simulations improved significantly over the last 20 years. A statistical analysis, as reported in Stern et al. [1], shows that in the 2010 Gothenburg Workshop [2], [3] the average error of the results of all resistance test simulations is 2.1 % rather than 4.7 % which was the average error evaluated during the Gothenburg Workshop 2005. Furthermore the uncertainty related to the simulation is around the 4.0%. This improvement is reached for the displacement or "conventional" ship.

The results of the main V&V works available in literature essentially on "conventional" hulls are reported in Appendix F.

A preliminary assessment of the V&V procedures was conducted on the displacement hulls, in particular, on a surface combatant ship, Figure 1 (a), and a SWATH hull, Figure 1 (b). The results of these preliminary studies are showed in the V&V state of art reported in Appendix F.

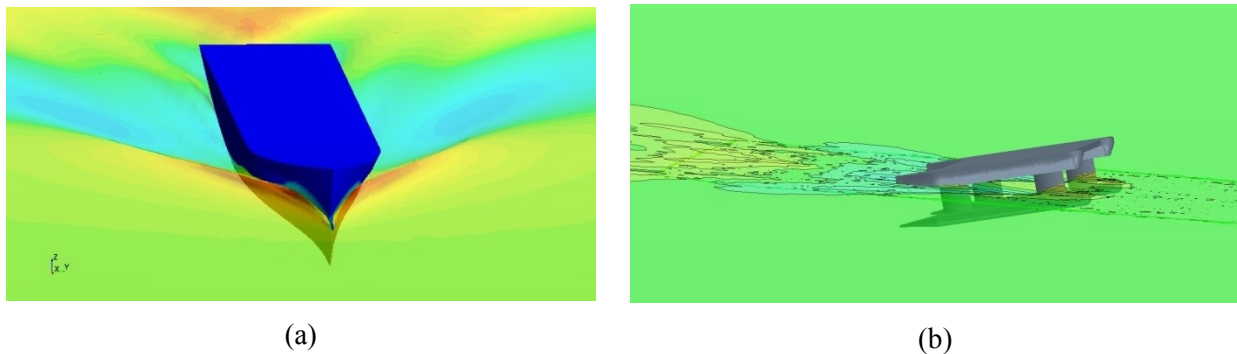


Figure 1 (a) Visualizations of Surface Combatant Ship, source: De Luca et al. [4]; and (b) SWATH hull, source: Begovic et al. [5]

The errors of the results mentioned above, however; are not applicable to the planing hull or in general to the high speed craft (HSC). For this reason the ITTC in the last CFD Committee Report stated: “For unconventional ships such as multi-hulls, planing boats, and new-concept hulls, it is a little harder to assess the state of the matters due to scarcity of relevant publications. [...] They found that mean prediction error of less than 10% could be achieved compared to the model-scale and full-scale test results. [4]”

For planing craft, the largest errors in the resistance evaluations are related to the errors in the evaluation of dynamic trim. This interpretation is based on the observed magnitudes of the errors of the numerically predicted trim and on the well-known relationship between dynamic trim and resistance at high speed, *i.e.*, $R_T = L \operatorname{tg} \tau + R_V$. In this equation, given by Sottorf [5], τ is the dynamic trim, R_V is the viscous resistance of the bare hull and $L \operatorname{tg} \tau$ is the resistance induced to the lift. This equation is valid for totally planing crafts but it also effectively describes the dependency of the trim on the resistance components, also for HSC not totally planing. Moreover it is worth noting that, in the small trim angle range, R_V also is influenced by the trim because of the significant variations of the wetted surfaces; therefore an incorrect quantification of the trim results in errors in both of the resistance components. The difficulty in identifying the dynamic trim is strictly due to the difficulties in identifying the center of pressure, or, generally, the pressure distribution on the hull bottom. The identification of pressure distribution is affected significantly by the edge effects and by the percentage of hydrodynamic lift to sustain the hull. Both of these are strongly related to the slenderness ratio (L/B) and to the deadrise angle (β).

These considerations highlight the adequacy of performing a V&V study, using models of hulls that have geometric differences that are essentially due to variations of the L/B and the β .

The purpose of this study indeed aims to reach a quantitative evaluation of the reliability of the results of the resistance test simulations of planing hull using the CFD and in particular the (U)RANS based codes. Specifically, the purpose is to carry out an estimation of the modeling and numerical limits of (U)RANS methods and obtain also, compatibly with the results, a direction to follow therefore improving the models.

2

THE VERIFICATION AND VALIDATION PROCESS

In this chapter a detailed analysis reports of the different verification and validation methodologies, with an emphasis on the procedures used in the field of Computational Fluid Dynamics (CFD). Furthermore different verification methodologies are reviewed and their shortcomings and criticisms are discussed.

1. Introduction

The significant increase of the use of CFD in engineering applications leads inevitably to a need to establish the accuracy to the numerical results. This goal can be achieved thanks to the verification and validation (V&V) processes. These processes respectively provide the numerical and modeling errors.

A widely known method which performs uncertainty quantification systems is the probabilistic method, such as the Monte Carlo (MC) method. However, the main limitations of the probabilistic method are associated to time cost and computational effort.

To date, performing model runs for realistic hydrodynamics problems that require the solution of complex flow fields is prohibitively expensive.

This is one of the motivations for the research of alternative methods and procedures.

2. Sources of error and uncertainty

It is important to distinguish between errors and uncertainties associated with the modeling and simulation process. These terms are commonly used interchangeably in the scientific literature, and can be defined in many forms depending on the application. For CFD simulations, the definition given by Oberkampf and Blotner [8] is adopted. They define uncertainty as a potential deficiency in any phase or activity of modeling and simulation process that is due to a lack of knowledge and error is defined as a recognizable deficiency in any phase or activity of modeling and simulation that is not due to a lack of knowledge.

They also divide group sources of error and uncertainty in five categories:

1. Physical modeling
2. Representation errors
3. Discretization and solution errors
4. Computer round-off error.
5. Programming errors

In Figure 2 the position of the errors can be observed in a simulation workflow. The five categories of errors listed above can be grouped into two key processes that characterize the simulation workflow and determine the two main macro-groups of sources of error and uncertainty: the physical modeling process and discretization solution process.

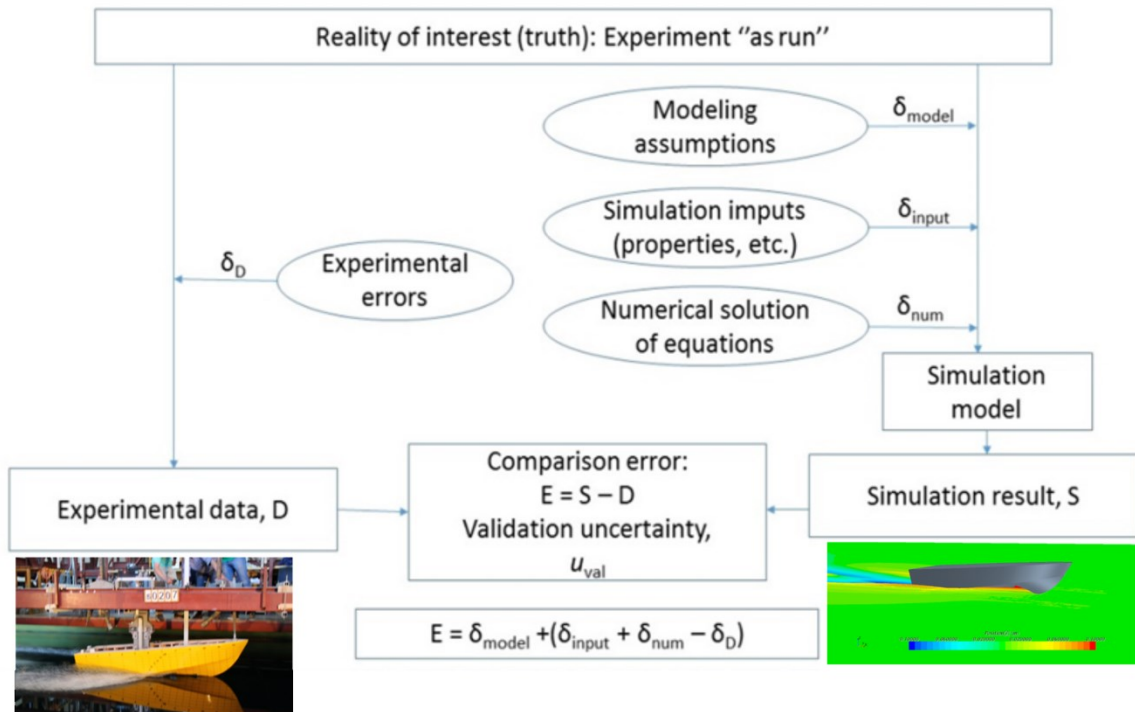


Figure 2 Simulation workflow with sources of error

The physical modeling process is classified as a source of error and uncertainty according to the definition given by Oberkampf and Blottner [8]. The physical modeling uncertainties arise from mathematical assumption and approximations of the physical problem (such as geometry, mathematical equation, coordinate transformation, boundary conditions, air–water interface, and turbulence models) and incorporation of previous data (such as fluid properties) into the model.

The discretization and solution process are classified as sources of error and uncertainty that can be quantified and reduced using available methods in the literature. Discretization (or numerical) error arises from the numerical solution of the mathematical equations (such as discretization, artificial dissipation, iterative and grid convergence, lack of conservation of mass, momentum, and energy, internal and external boundary no-continuity and computer round-off), as mentioned in Stern et al. [9].

According to Stern et al. [7], the approximation used in numerical simulations will result in error δ_S , which is the difference between a simulation value S and the truth T . However, the true values of simulation quantities are rarely known. Only the experimental data D and the relative error δ_D can be known, as in Figure 2.

An uncertainty U is an estimate of an error such that the interval $\pm U$ contains the true value of δ_S at the 95% confidence level. And so the δ_S is the sum of modeling and numerical errors, as reported in the following equation.

$$\delta_S = S - T = \delta_{SM} + \delta_{SN} \quad (1)$$

The above formula can be re-expressed for the simulation uncertainty as follow

$$U_S^2 = U_{SM}^2 + U_{SN}^2 \quad (2)$$

Where U_S is the simulation uncertainty, U_{SM} , and U_{SN} are respectively the simulation modeling uncertainty and simulation numerical uncertainty.

3. Uncertainty analysis methods

Before dealing with the detailed analysis of the calculation techniques of simulation uncertainty and error, it is appropriate to address a brief digression on the available methods for the uncertainties estimation.

The two main approaches for the uncertainties quantification are deterministic (or non-probabilistic) and probabilistic methods.

4. Deterministic methods

In the deterministic approach, uncertainties are often represented by the widest error bounds of model parameters and inputs. The maximum error bounds of model outputs must then be necessarily computed since the probability structure of the model inputs or parameters are not taken into account.

Furthermore, the propagating error using deterministic approaches is based on the assumption that each model input interval contains its entire uncertainty. This assumption may not always be the case. For example, an estimate of the standard deviation of available experimental data may be less (or possibly much less) than the width of the uncertainty model input interval. The main deterministic methods for uncertainty analysis are interval analysis and propagation of error using sensitivity derivatives.

In interval analysis the value of a variable is replaced by a pair of numbers representing the maximum and minimum values that the variable is expected to take. Interval arithmetic rules are then used to perform mathematical operations with the interval numbers.

The other method is the propagation of error using sensitivity analysis. It has been in use for many years in the literature (e.g. Green et al. [10]). The purpose of sensitivity analysis is to estimate the rate of change in model outputs with respect to changes in model inputs. Furthermore, it can also be used to assess the relative contributions of the model inputs and parameters uncertainty to the model outputs uncertainty. The desired method of choice depends upon the type of sensitivity measured, user-defined accuracy, and computational cost.

In the CFD community, the desired choice for sensitivity analysis is the local gradient approximation. The estimate of the model sensitivity is given by gradients or partial derivatives at a local point in the temporal and spatial domain. If k is a set of m parameters (k_1, k_2, \dots, k_m), and u is a vector of n output variables (u_1, u_2, \dots, u_n), then the sensitivity, S^* , is given by

$$S_{ij}^* = \frac{\partial u_i}{\partial k_j} \quad (3)$$

Where ∂k_j is the error associated with parameter k_j , then a deterministic approximation to the output error, δu_i , is given by:

$$\delta u_i = \sqrt{\sum_{j=1}^n (S_{ij}^*)^2 \delta k_j} \quad (4)$$

Where $i = 1, 2, \dots, n$ and $j = 1, 2, \dots, m$.

An example in CFD of this technique is presented in the work of Pelletier et al. [11].

There are several methods for computing sensitivity derivatives. The desired method of choice depends upon the difficulty of implementation and accuracy of the results. The main approaches for computing sensitivity derivatives are:

- Finite Difference,
- Complex Variable Formulation,
- Discrete Adjoint Method.

More details of these approaches were reported in Perez [12].

5. Probabilistic methods

The probabilistic methods can be divided into statistical and non-statistical methods.

- Statistical methods use a large number of values of the input variables to calculate them repeatedly for the output ones. A sampling method is used to generate the input values from a distribution. Statistics, such as the mean and variance, of the output values can then be calculated. The classic example of a statistical method is the Monte Carlo method. However these methods are computationally expensive.
- Non-statistical methods use an analytical treatment of the uncertainty and are much less computationally expensive. Examples of these methods are the moment (or perturbation) method and stochastic differential equation method.

In the probabilistic approach, uncertainty is represented by the probability of the random event. Furthermore, probabilistic analysis is the prevalent choice for uncertainty analysis of physical systems when estimates of the probability distribution of uncertain model inputs are available.

Uncertainties associated with model inputs can be quantified by probability distributions, and an estimate of the model's output probability distribution can be obtained. Note that this process consists of two stages.

The first stage involves the determination of the probabilistic distribution of the model inputs and parameters, and model formulation. Probability distributions of model inputs are estimated via statistical techniques that use available data or a representative number of samples.

The second stage involves the propagation of uncertainty through models. The main aim of uncertainty propagation is to compute the probability distribution of model outputs. The output probability distribution can then be used to estimate statistical parameters of interest (e.g., mean and variance of model outputs).

The main techniques for propagating uncertainty through models can be grouped in two macro-groups: statistical and non-statistical methods.

a. Statistical methods

All of the statistical methods are based on sampling methods. The sampling-based methods involve running a model at a set of sampled points, and using the model results at the sampling points in order to relate the model inputs and outputs.

The advantage of these methods is that the model equations or existing code is treated as a black box (*i.e.*, no modification of the model equations or code is required). For this reason, sometimes, these methods are called Non-Intrusive methods.

Widely used sampling based methods are: Monte Carlo (MC), Latin Hypercube Sampling (LHS), and Stochastic Collocation (SC). These methods are discussed below.

MC Methods

The MC is a statistical method. The main advantage of the MC methods is that the model equations or existing code are treated as a black box. The simplest of all MC methods, referred to as standard (or basic) MC, involves the sampling of input random variables from their known or assumed probability density function (PDF), and computing deterministic model output for each of the sample input values.

The procedure for the basic MC method involves three steps: for each input variable, a set of values is generated by randomly sampling the known or assumed PDF for each set of random input data, executing a deterministic mathematical model and combine the output data use the statistics of the output data set (mean, variance, skewness, kurtosis, etc.), to define its probability density function.

It is important to note that while the MC method converges to the exact stochastic solution as the number of samples goes to infinity, the convergence of the mean error estimate is slow because the standard deviation of the mean scales inversely with the square root of the number of samples. Hence thousands or millions of data samples may be required to get the required accuracy. Since this method requires a large number of

sample or model runs, it's not suitable for computationally intensive problems. The time and resources required by this method may be prohibitively expensive for realistic hydrodynamics problems.

The MC method has been applied to some very small CFD simulations with the aim to demonstrate the method, as in Walters and Huysse [13].

In order to reduce the computational effort, modifications of the basic MC method have been developed. These efficiency improvements are known as variance reduction techniques. One of the modified MC methods is the LHS. It is popular because it is easy to implement and reduce the computation time while still providing the required accuracy in the particular situations described below.

Latin Hypercube Sampling (LHS)

Substantial computational efficiency over the basic MC method is accomplished by the use of the modified MC method. The number of necessary solutions is reduced in the modified MC method compared to the basic MC method by efficient sampling from the input probability distribution. One such widely used modified MC method is the LHS developed by McKay [14].

In this method, the range for each input uncertain parameter of a model is divided into non-overlapping intervals on the basis of equal probability. Thus, only one value from each interval is selected at random with respect to the PDF in the interval. Note that the LHS method has a smaller variance than the standard MC method. Hence, the convergence of LHS method is much faster than the standard MC. Since the whole parameter space, consisting of all the uncertain parameters, is partitioned into cells of equal probability, random samples are generated from all the ranges of possible values. Consequently, this feature gives insight about the extremes of the probability distributions of the outputs. Note that this feature is not contained in the basic MC method, where there may be cases that do not include the extremes of the random sampling. However, the drawback of the LHS method is that the number of samples for realistic hydrodynamic problems could still be too large and expensive.

Stochastic Collocation (SC)

Another uncertainty quantification method is the Stochastic Collocation (SC). This method was developed in order to overcome the drawback of the MC methods and is based on a polynomial approximation of the response.

The SC method is a widely used example, which is based on sampling Gauss quadrature points and using Lagrangian polynomial interpolation in probability space. However, due to the structured grid of the quadrature points in multiple random dimensions, the spectral convergence of the SC method reduces significantly with an increasing number of uncertainties, as shown in Figure 3. More information on this method is available in Witteveen et al. ([15], [16])

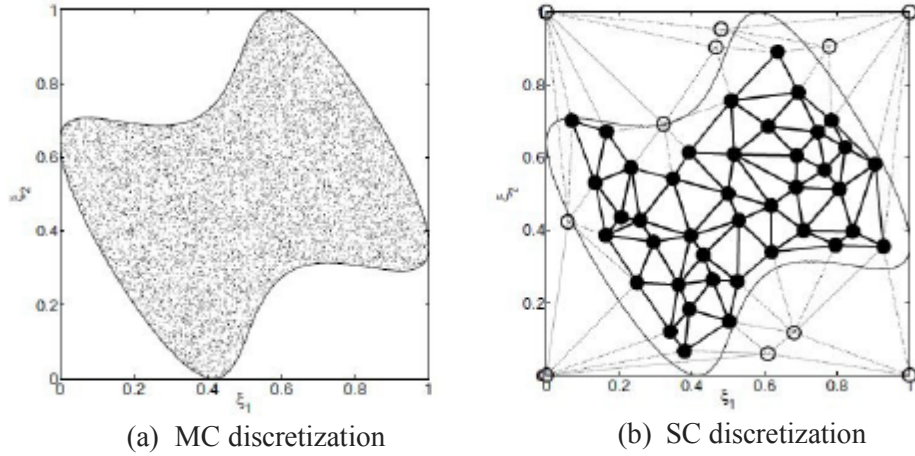


Figure 3 Examples of discretization by the MC and SC methods, source: Witteveen et al. [16]

b. Non-statistical methods

Moment Methods

Uncertainty analysis in CFD simulation using moment methods have appeared in the literature in the last twenty years (e.g. Huyse [17]). Moment methods involve using the truncated Taylor series expanded about the expected value of the inputs. For example, if $u = u(\xi)$ is expanded about mean values of $u(\xi)$, the first-order moment approximation of the Taylor series is:

$$u(\xi_1, \xi_2) = u(\bar{\xi}_1, \bar{\xi}_2) + \frac{\partial u}{\partial \xi_1} (\xi_1 - \bar{\xi}_1) + \frac{\partial u}{\partial \xi_2} (\xi_2 - \bar{\xi}_2) \quad (5)$$

Note that first-order first moment (FOFM) approximation is the deterministic value evaluated at the mean of the input (ξ). The first-order second moment (FOSM) method requires the computation of sensitivity derivatives. to estimate the variance (second moment) of the output is equal to the variance of the input parameter multiplied by the square of the first sensitivity derivative evaluated at the mean value of the input. For cases involving relatively large variations in the input random variables, increased accuracy of the model output statistics is obtained using higher order moment formulas. This requires the estimation of higher order derivatives which may be impractical in terms of the accuracy and implementation of the method, and the computational resources required.

Spectral Methods

Spectral methods, otherwise known as polynomial chaos expansions, used to model and propagate uncertainty in stochastic computational simulations by several researchers, e.g. Ghanem and Spanos [18], Xiu and Karniadakis [19], and Patterson et al. [20].

An important concept of spectral representation of uncertainty is that one may decompose a random function (or variable) into separable deterministic and stochastic components. Each variable in the equations of the mathematical model, such as pressure or velocity, is expanded into an infinite series using Hermite

polynomials. In theory the series is infinite, but for practical problems it must be truncated to a finite series. The first term in the series represents the mean value of the variable. The second term represents the Gaussian random fluctuations around the mean value. The third and higher terms represent non-Gaussian random fluctuations. In this way the random behavior is decomposed into a finite number of orthogonal modes of fluctuation.

This concept is similar to the modes of vibration of a mechanical system which occur at particular points in the frequency spectrum.

6. Solution verification methodology in ship hydrodynamics

In ship hydrodynamic field the uncertainty quantification is based on the deterministic method, and in particular on sensitivity derivatives.

In the following paragraphs an overview of the overall verification and validation approach used in ship hydrodynamics is provided, including methodology and procedures. Stern et al. [9] and ITTC uncertainty analysis in CFD [21] should be consulted for detailed presentation and discussions.

As aforementioned, solution verification is the process to estimate U_{SN} . Solution verification is mathematical activities, with no consideration of the agreement of the numerical model results with physical data from experiments (which is the concern of validation).

The U_{SN} is estimated by the solution verification process. The most important numerical errors and uncertainties are due to use of iterative solution methods and specification of various input parameters such as spatial and time-step sizes and other parameters (e.g. artificial dissipation). The errors and uncertainties are highly dependent on the specific application (geometry and conditions).

The errors due to specification of input parameters are decomposed into error contributions from iteration number δ_I , grid size δ_G , time step δ_{TS} , and other parameters δ_P , which gives the following expressions for the simulation numerical error (equation 6), and uncertainty (equation 7).

$$\delta_{SN} = \delta_I + \delta_G + \delta_{TS} + \delta_P = \delta_I + \sum_{j=1}^J \delta_j \quad (6)$$

$$U_{SN}^2 = U_I^2 + U_G^2 + U_{TS}^2 + U_P^2 = U_I^2 + \sum_{j=1}^J U_j^2 \quad (7)$$

According to Stern et al. [9] and ITTC uncertainty analysis in CFD [21], it is possible to estimate the sign and the magnitude of the simulation numerical error, when conditions permit. This complete estimation of the error is called corrected error and, obviously, is possible to compute the uncertainty in this estimation, called corrected uncertainty U_{SN}^* . Consider the corrected case, error estimate δ_{SN}^* and simulation numerical uncertainty can be divided as equations 8 and 9.

$$\delta_{SN}^* = \delta_I^* + \sum_{j=1}^J \delta_j^* \quad (8)$$

$$U_{SN}^{*2} = U_I^{*2} + \sum_{j=1}^J U_j^{*2} \quad (9)$$

7. Verification procedures

The verification process for many common input parameters (e.g. grid spacing, time-step and artificial dissipation) are conducted using the multiple solutions method. In order to do this it is necessary to use a minimum of three solutions ($m = 3$) which have been uniformly refined with an increment Δx_k such that defines a constant refinement ratio r_k

$$r_k = \frac{\Delta x_{k_m}}{\Delta x_{k_{m-1}}} \quad (10)$$

ITTC Guidelines [21] recommend for the industrial application refinement ratio (r_k) between $\sqrt{2}$ and 2.

Next a convergence ratio R_k was defined to give information about convergence/divergence of a solution. This is achieved by considering the solution changes ε_{ijk} for the input parameter k between three solutions ranging, from fine S_{k1} to medium S_{k2} and coarse S_{k3} , in order to determine R_k .

$$\begin{aligned} \varepsilon_{21k} &= S_{k2} - S_{k1} \\ \varepsilon_{32k} &= S_{k3} - S_{k2} \\ R_k &= \varepsilon_{21k} / \varepsilon_{32k} \end{aligned} \quad (11)$$

According to the ITTC guidelines [21] and the extended versions reported in some works, e.g. Stern et al. [22], four different cases of R_k may occur:

1. Monotonic convergence: $0 < R_k < 1$;
2. Oscillatory convergence: $R_k < 0$, $|R_k| < 1$;
3. Monotonic divergence: $R_k > 1$;
4. Oscillatory divergence: $R_k < 0$, $|R_k| > 1$.

In the Case 1 the generalized Richardson Extrapolation (RE) is used to assess the uncertainty U_k or the error estimate δ_k and the corrected uncertainty U_k^* , as shown in the next paragraphs.

For oscillatory convergence (Case 2) U_k is estimated by determining the error between the minimum (S_L) and maximum (S_U) values of the oscillation. Equation 12 is valid only in the asymptotic regime.

$$U_K = \left| \frac{1}{2} (S_U - S_L) \right| \quad (12)$$

Oscillatory convergence could be erroneously recognized instead of Case 1 or 3. Therefore it is often necessary to investigate more than three solutions to get a sensible assessment of the error δ_k .

In the case of monotonic or oscillatory divergence (cases 3 and 4), it is not possible to estimate errors or uncertainties.

a. Generalized Richardson Extrapolation (RE) method

As stated above, in case of monotonic convergence the generalized RE was used to determine the error δ_k with respect to refinement ratio r_k and order-of-accuracy. The RE method, as indicated by Roy [23], is based on the series expansion of the discretization error, as below reported.

$$\delta_{RE} = S_i - S_0 = q_i \Delta x_i^p + \dots \approx q_i \Delta x_i^p \quad (13)$$

Where δ_{RE} is the error evaluated by generalized RE method, q_i is the coefficient of the i^{th} order error term and S_0 is the exact solution, generally not known.

The assumptions that are required for using RE are that the solutions are smooth, and the higher order terms in the discretization error series expansion are small, and uniform meshes are used. The second assumption regarding the higher-order terms are true in the asymptotic range if Δx_i is sufficiently small so that the lower-order terms in the expansion not dominate.

The RE method can be generalized to p^{th} - order of accuracy with solutions on a fine value (Δx_{k2}) and a coarse value (Δx_{k1}), which are different by a factor of r_k . The discretization error equations can be written as:

$$\begin{aligned} S_1 &= S_0 + q_1 \Delta x_k^p + O(\Delta x_k^{p+1}) \\ S_2 &= S_0 + q_1 (r_k \Delta x_k)^p + O([r_k \Delta x_k]^{p+1}) \end{aligned} \quad (14)$$

Neglecting the higher-order terms, these two equations can be solved for S_0 to give:

$$S_0 = S_1 + \frac{S_1 - S_2}{r_k^p - 1} \quad (15)$$

Which is generally a $(p+1)$ - order accurate estimate. Again, it should be emphasized that RE relies on the assumption that the solutions are asymptotic (*i.e.*, the observed order of accuracy matches the formal order).

b. Observed order of accuracy

When the exact solution is not known (which is generally the case for solution verification), as above mentioned, at least three numerical solutions are required in order to calculate the observed order of accuracy (p_k). Considering a p^{th} - order accurate scheme with numerical solutions on a fine value (Δx_{k3}), a medium value (Δx_{k2}), and a coarse value (Δx_{k1}). For the case of a constant r_k , it is possible to write:

$$\Delta x_{k_1} = \Delta x_k, \Delta x_{k_2} = r_k \Delta x_k, \Delta x_{k_3} = r_k^2 \Delta x_k \quad (16)$$

The three discretization error equations can be written as

$$\begin{aligned} S_1 &= S_0 + q_1 \Delta x_k^p + O(\Delta x_k^{p+1}) \\ S_2 &= S_0 + q_1 (r_k \Delta x_k)^p + O([r_k \Delta x_k]^{p+1}) \\ S_3 &= S_0 + q_1 (r_k^2 \Delta x_k)^p + O([r_k^2 \Delta x_k]^{p+1}) \end{aligned} \quad (17)$$

Neglecting the higher-order terms, these three equations can be used to solve for p_k to give.

$$p_k = \frac{\ln(S_3 - S_2)}{\ln(r_k)} \quad (18)$$

Note that here the observed order of accuracy is calculated and does not need to be assumed (as with RE). For the case of non-constant grid refinement factors, more information for this case can be found in Stern et al. [9].

8. Methods for uncertainty estimation

When the monotonic convergence is reached δ_k , U_k , and p_k can be evaluated by different solution verification methods. The general form of the uncertainty evaluation can be written as shown in equation 19.

$$U_k = F_S \left(\frac{\mathcal{E}_{21k}}{r_k^{p_k} - 1} \right) \quad (19)$$

The various solution verification methods differ in the procedure for determining the safety factor (F_S) and p_k .

a. The Grid Convergence Index (GCI) method

A method for the uncertainties estimation using generalized RE is the GCI method. This approach was proposed by Roache ([24], [25]), where the error estimation based on RE method is multiplied by a F_S to bound the simulation error for the uncorrected case (equation 20) and corrected case (equation 21).

$$U_k = F_S |\delta_{RE_k}| \quad (20)$$

$$U_k = (F_S - 1) |\delta_{RE_k}| \quad (21)$$

The exact value for factor of safety is somewhat ambiguous. Roache recommends for careful grid studies (tree or more grids) a fixed percentage of the error estimate (e.g. 25 % of δ_{RE}), and therefore $F_S=1.25$. Unlike the other methods, in the GCI the uncertainty of the error is estimated regardless of how close solutions are to the asymptotic range. There are different variants of the GCI method such as the GCI_1 , GCI_2 , GCI_3 and GCI_{OR} , etc., more details are reported in Stern et al. [1]. The choice of F_S in the different GCI methods requires user judgement calls, for which no single guideline is currently available.

b. The Correction Factor (CF) method

Another method for uncertainty estimation is the Correction Factor (CF) method. The correction factor is a variable factor of safety (C_k) and is used to include the effect of higher-order terms neglected earlier (by the GCI method). The C_k is defined as follows:

$$C_k = \frac{r_k^{p_k} - 1}{r_k^{p_{th}} - 1} \quad (22)$$

With p_{th} as estimation of the theoretical order of accuracy. The error δ_k is defined by replacing F_S with C_k .

$$\delta_k = C_k \delta_{RE_k} = C_k \left(\frac{\mathcal{E}_{21_k}}{r_k^{p_k} - 1} \right) \quad (23)$$

The correction C_k makes a single term estimate which roughly accounts for higher order terms. Depending how close the error δ_k is to the asymptotic range ($C_k \rightarrow 1$), the expression to assess the uncertainties takes different forms, according to the revised formulation delivered by Wilson et al. [26]. However the uncertainty is always calculated by the sum of the absolute value of the improved error estimate and the absolute value of the amount of the correction, as reported in equations 24 and 25 for the uncorrected and corrected case.

$$U_k = \begin{cases} [2|1-C_k|+1]|\delta_{RE_k}| & |1-C_k| \geq 0.125 \\ [9.6(1-C_k)^2+1.1]|\delta_{RE_k}| & |1-C_k| < 0.125 \end{cases} \quad (24)$$

$$U_k^* = \begin{cases} [1-C_k]|\delta_{RE_k}| & |1-C_k| \geq 0.25 \\ [2.4(1-C_k)^2+0.1]|\delta_{RE_k}| & |1-C_k| < 0.25 \end{cases} \quad (25)$$

c. The Modified GCI method

As reported in Stern et al. [1], the GCI and CF methods have two deficiencies. The first one is that the uncertainty estimates for $p_k > p_{th}$ are unreasonably low in comparison to those with the same distance to the asymptotic range for $p_k < p_{th}$. The second one is that there is no statistical evidence for what confidence level the GCI and CF methods can actually achieve.

For these reasons Xing and Stern [27] developed a comprehensive review of the GCI method. They tried to remove the two deficiencies previously indicated for the GCI and CF methods. The best error estimate is used to construct the uncertainty for uncorrected case (equation 26).

$$U_k = \begin{cases} [F_{S1}P + F_{S0}(1-P)]|\delta_{RE_k}| & 0 < P \leq 1 \\ [F_{S1}P + F_{S2}(P-1)]|\delta_{RE_k}| & P > 1 \end{cases} \quad (26)$$

Where P is equal to the ratio between predicted and theoretical order of accuracy ($P = p_k/p_{th}$); $F_{S0} = 2.45$, $F_{S1} = 1.6$ and $F_{S2} = 14.8$ are recommended values based on statistical analysis.

d. Least Square Root (LSR) – GCI Method

Another review of the GCI method was proposed by Eça and Hoekstra ([28] and [29]). This approach is based on a Least Squares Root (LSR) method applied on the GCI method. The LSR method is used to minimize the square root of the squares of the residuals of equation 27, in other words the method is used to find values of S_0 , q and p_k which minimize the function:

$$f(S_0, q, p_k) = \sqrt{\sum_i^{n_g} (S_i - (S_0 + q r_k^{p_k}))^2} \quad (27)$$

Where n_g is the number of the grids available.

The minimum of $f(S_0, q, p_k)$ is found by setting its derivatives with respect to S_0 , q , and p_k equal to zero. The standard deviation of the fit (U_S) is given by:

$$U_S = \sqrt{\frac{\sum_i^{n_g} (S_i - (S_0 + q r_k^{p_k}))^2}{n_g - 3}} \quad (28)$$

Using the S_0 , q , and p_k , it is possible to calculate the δ_{RE} using directly the equation 13, and, obviously, when $n_g = 3$ the U_S is equal to zero. The error estimation were performed by the generalized RE method, when the monotonic convergence was achieved.

Furthermore Eça and Hoekstra have tried to overcome the drawbacks of the other procedures above mentioned and, in particular, have observed that the classification approach based on R_k , is not as straightforward, because the data may exhibit scatter, in particular in the hydrodynamics field. Indeed the cases are classified by the estimated order of accuracy p_k , instead of R_k . The convergence condition is given as follows:

- $p_k > 0$: monotonic convergence
- $p_k < 0$: monotonic divergence
- $p_k^* < 0$: oscillatory divergence
- Otherwise: oscillatory convergence.

Where p_k^* is the estimated order of accuracy evaluated by the equation 27 using $S_i^* = |S_{i+1} - S_i|$, instead of S_i . The only condition which allows an error estimation based on RE is the monotonic convergence.

In other cases one must rely on alternative uncertainty quantification, which is based on the maximum difference between all the solutions available (Δ_M).

If p_k is between 1 and 2 the GCI was applied with the F_S equal to 1.25. If $p_k < 1$, δ_{RE} tends to become over-conservative and so was taken the minimum of δ_{RE} and Δ_M .

For super-convergence, *i.e.* p_k higher than the theoretical order of accuracy (p_{th}), the values of δ_{RE} are not reliable. In most of these cases, the observed super-convergence is not real and it is merely a consequence of the numerical shortcomings affecting the estimation of p_k .

If more than 3 grids are available, this is easily identified from the very strong dependence of p_k on the data points selected. Therefore, in case of super-convergence the error estimation with generalized RE method was performed with p_k replaced by its theoretical value.

It is possible to summarize the proposed procedure for the estimation of the numerical uncertainty, as follows for monotonic convergence:

- $U_k = 1.25\delta_{RE} + U_S$, for $0.95 \leq p_k < 2.05$;
- $U_k = \min(1.25\delta_{RE} + U_S, 1.25\Delta_M)$, for $p_k < 0.95$;
- $U_k = \max(1.25\delta_{RE} + U_S, 1.25\Delta_M)$, for $p_k > 2.05$.

If monotonic convergence is not observed:

- $U_k = 3\Delta_M$

More detailed about this method are reported in Eça and Hoekstra ([28], [29]) and the criticisms of this approach are highlighted in Tao and Stern [30].

9. Verification procedure for iterative convergence

The verification process for iterative convergence cannot be performed by using the multiple solutions method, as for many others input parameters (e.g. grid spacing, time-step and artificial dissipation). Methods for estimation of iterative errors and uncertainties can be based on graphical, as discussed below or theoretical approaches and are dependent on the type of iterative convergence:

1. Oscillatory.
2. Convergent.
3. Mixed oscillatory/convergent.

For the oscillatory convergence case (Case 1), the deviation of the variable from its mean value provides estimates of the iterative uncertainty based on the range of the maximum S_U and minimum S_L values.

$$U_I = \left| \frac{1}{2}(S_U - S_L) \right| \quad (29)$$

For the convergent case (Case 2), a curve-fit of an exponential function can be used to estimate U_I or δ_I and U_I^* as the difference between the value and the exponential function from a curve fit for large iteration number (S_∞)

$$U_I = |S - S_\infty| \quad (30)$$

$$\delta_I = S - S_\infty \quad (31)$$

For the mixed convergent/oscillatory case (Case 3), the amplitude of the solution envelope decreases as the iteration number increases, the solution envelope is used to define the maximum S_U and minimum S_L values in the i^{th} iteration, and to estimate U_I or δ_I and U_I^* .

$$\delta_I = S - \frac{1}{2}(S_U - S_L) \quad (32)$$

10. Solution validation

Solution validation is a process for assessing simulation modeling uncertainty U_{SM} by using benchmark experimental data D and, when conditions permit, estimating the sign and magnitude of the modeling error δ_{SM} itself.

$$E = D - S = \delta_D - (\delta_{SM} + \delta_{SN}) \quad (33)$$

$$U_V^2 = U_D^2 + U_{SN}^2 \quad (34)$$

For validation purpose the comparison error E between the benchmark experimental data D and the simulation result S is determined in order to assess modeling uncertainty U_{SM} , where E is the comparison error, δ_D is the difference between an experimental data and the truth and U_V is the validation uncertainty.

To determine whatever a value has been validated, E is compared with U_V .

When $|E| < U_V$, the combination of all of the errors in D and S is smaller than U_V , and validation is achieved at the U_V interval. The level of confidence in the CFD model is indicated by the magnitude of the validation uncertainty.

If $|E| > U_V$, the combination of all errors in both the simulation and in the experimental data is greater than the validation uncertainty. Then validation has not been achieved for this validation uncertainty level.

In the case that $U_V \ll |E|$, the δ_{SM} highlights the need to improve the simulation modeling.

3

PHYSICAL MODEL OF PLANING HULL

This chapter delineates the basic functioning of the planing hulls, in order to describe which the critical issues are for the CFD simulations of planing hulls. In addition a detailed literature overview on the application of CFD codes, and in particular of RANS based method, on simulation of planing hulls is reported.

1. Resistance model of the planing hulls

A brief introduction of the classical models may be useful to describe the behavior of hulls, with a special focus on the partial or total hydrodynamic sustained hulls.

The nature of the forces operating in the flow around hulls is quite articulated. Ships are actually means of transportation balanced between two fluids and, exactly because of this separation between the two fluids; resistances due to forces of different nature are generated.

There are three main acting forces: viscous, inertial and gravitational. In order to simplify the complexity of the physical model, the forces due to the surface tension are not taken into account here.

When evaluating the resistance, usually the resolution of the effects is operated. The resolution of resistances into different parts leads necessarily to some mistakes in terms of mutual interaction of forces of a different nature. First, there should be a resolution of resistance into two parts: a component linked to viscosity phenomena, causing viscous resistance and a second one linked to gravitational phenomena, causing wave resistance. The forces with a viscous nature depend, obviously, on the viscosity and density as well as on the shape of the ship, as any other component of resistance.

The wave drag is linked to the energy dispelled by the pressure gradients active close to the free surface and is released through the wave systems generated on the surface.

Despite the pressure acting on the hull surface, it is responsible of one of the component of the resistance; it is, potentially, an important tool, which reduces both main components of the resistance. Conforming the bottom of the hull to assure a significant angle of incidence of the water on all the speed range, the pressure on the bottom triggers off a virtuous circle that increase the lift with speed. As the speed increases, the lift takes the place of the buoyancy and the underwater volume and wetted surface decrease. The main consequences of these variations are the reduction of both components of the resistance that are strongly dependent on the dimensions of the wetted surface on which tangential and perpendicular stresses work.

As above mentioned, the dynamic of the planing crafts is strongly dependent on the angle of incidence of the water on the hull bottom, that is determined not only by speed, but also by the hull form as seen by the water, *i.e.* the trim under speed.

The heavy influence of the trim on the resistance is highlighted by the dynamic of a flat plate sailing on a liquid surface. The flat plate by definition has no volume and therefore it is in a purely hydrodynamic equilibrium: if W is the weight of the plate, L the hydrodynamic lift, R_y the vertical component of the integral of the pressures, and R_x the longitudinal component of the integral of the pressures, then:

$$R_y = L = W \quad (34)$$

As mentioned for the general case, forces with a viscous nature act on the plate, alongside with forces linked to pressures initiated by the plate sailing on the free surface. By using the simplified model of the flat plate, the viscous forces are turned into pure friction forces, R_t , tangent to the plate and turn the resultant of the pressure range into a component orthogonal to the plate. This, in addition to the fact that the plate is intended to be fully lifted by hydrodynamic pressures, leads us to the Sottorf formula reported in [7] with reference to Figure 4.

$$R_x = W \tan \tau + \frac{R_t}{\cos \tau} \quad (35)$$

The Sottorf formula clearly shows the effects of the longitudinal trim on the resistance due to the lift. It should also be considered that the R_t component depends on the size of the wetted surface; the smaller the trim, the higher it will be.

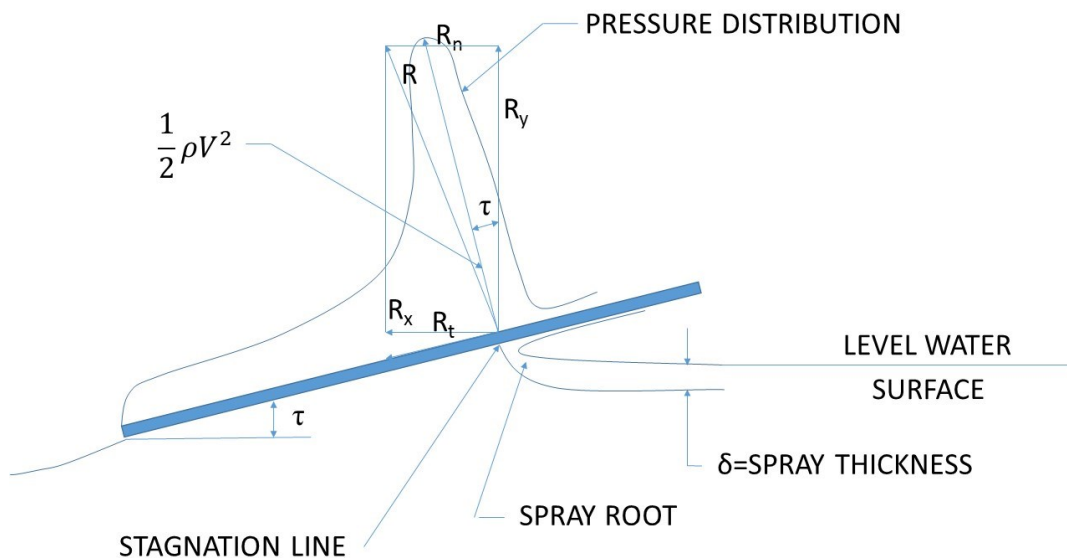


Figure 4 Forces applied on the flat plate

The Figure 4 shows the spray root and the pressure distribution resulting from it. The term “wetted area” designates that portion of the wetted area over which water pressure is exerted and excludes the forward thrown spray sheet. The wetted area used in this sense is often designed in the literature as the ‘pressure area’ and, geometrically, includes the wetted area of the bottom hull aft of the stagnation line.

When shifting from an indefinite plate to a plate with definite size, a transversal pressure gradient due to the continuity and the congruency of the same on the edges of the plate is determined on its bottom. These gradients are responsible of the three-dimensional nature of the flow. In a kinematic perspective this leads to a divergent streamline, shown in the following Figure 5.

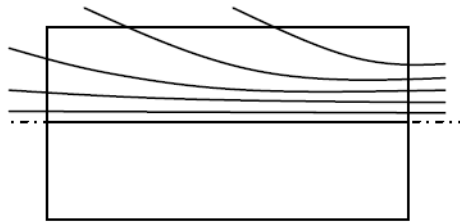


Figure 5 Transversal flow on the flat plate

The simplified model, in spite of the differences between the flat plate and a real hull bottom, is strictly corresponds to the actual physics of planing hulls, if the craft is totally hydro-dynamically sustained. Nevertheless, the Sottorf formula does not clarify the influence of hull form on the resistance. In particular, it has to take into account the two main geometrical characteristics influencing the phenomena: the slenderness ratio and the deadrise angles. These elements influence the divergence of the streamlines and, consequently, the pressure distribution on the hull bottom. Both of these increase the divergence of the streamlines by the increasing of the transversal pressure gradient.

Referring to the above explained considerations on the dimension of the wetted surface and on the different roles that its parts play (pressure and spray areas), the Figure 6 shows the streamlines, the shape, and position of the various part of the wetted surface.

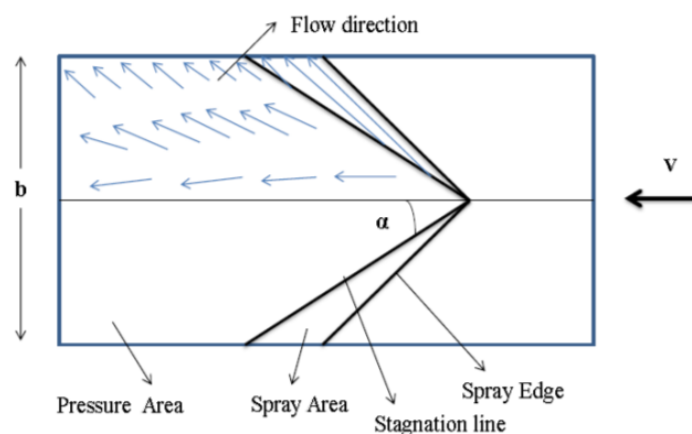


Figure 6 The projected area of a planing hull, source: Savitsky [31]

The pressure area is limited by wetted chine length, wetted keel length and stagnation line and it is the part of hull for which all hydrodynamic equations for lift, drag and center of pressure are applicable. The spray area is forward of stagnation line. This area is the part of the hull bottom still in contact with water delimited by the stagnation line and the spray edge. Both areas can be easily identified in a monohedral hull reported in Figure 7 (a).

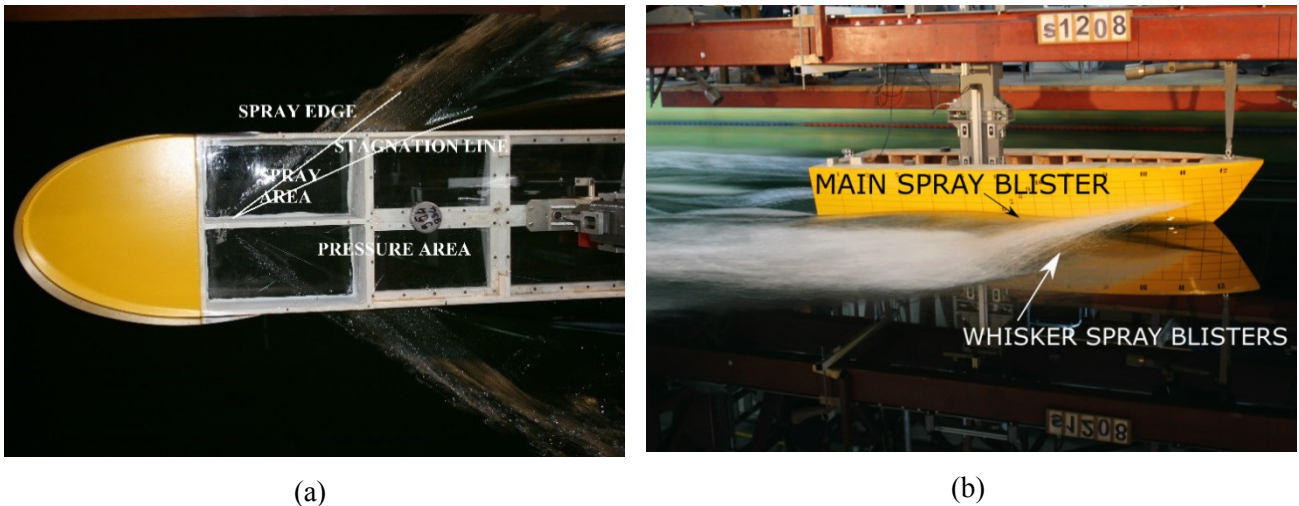


Figure 7 (a) The projected area of a planing hull, source: Begovic et al. [32]; (b) Blisters spray visualization

Capturing accurately the dynamic of the planing hull is a challenge for CFD simulations. Furthermore, in addition to the difficulties for the RANS based codes in determining the actual pressure distribution (extremely high gradients in small size), it has to consider the complexity/limit for the RANS solver to evaluate the spray sheet zone (on the hull) and the blisters spray (around the hull), Figure 7 (b). These matters will be examined in the Chapter 5.

2. CFD application on planing hull: literature overview

The evaluation of planing hull performance by CFD methods started recently and still today there are some significant levels of criticality in the use of CFD software for such evaluation in particular in terms of the running attitude.

One of the first applications of CFD in this hydrodynamic field is conducted by Caponneto [33]: in this application, a RANS solver is used to investigate a planing hull in which the displacement and center of gravity are unknown. Different hull positions were tested, a combination of three trim angles and three sinkages is performed for each speed. Then, interpolation is used to specify the running attitude of the vessel. Azcueta [34] uses commercial software (COMET) to simulate the planing hull. The steady state flow computations efficiently creates a complete resistance curve in one time - from zero to maximum speed of ship - instead of doing the computations for only one speed at a time. The dynamic trim, dynamic sinkage and resistance also are computed for the entire Fr -range.

Subramanian et al. [35] investigated the pressure and resistance characteristics of a single-chine planing craft. They used two hull forms, *i.e.*, one with a propeller tunnel and one without, and they compared the results with the towing tank test.

Brizzolara and Serra [36] investigated the accuracy of RANS codes in the prediction of planing surfaces. They used a wedge-shaped planing hull to analyze simulations in which the running trim angle is varied systematically. They compared their results with the available experimental data, as well as to the results achieved by Savitsky [37] and Shuford [38]. The capability of numerical methods to provide accurate results for planing surfaces was confirmed by the results that were obtained, *i.e.*, an average of 10 % error in predicting the total resistance and 5 % error in predicting the total lift.

The importance of dynamic equilibrium calculations in predicting a vessel performance is addressed by all of the authors mentioned above. Brizzolara and Villa [39] paid particular attention to this problem by developing an external Java/C++ routine to change the position of the hull during the non-stationary time step iterations to converge faster and better on the hydrodynamic equilibrium of the hull, thereby avoiding the unrealistic forces caused by the initial impulsive acceleration.

Su et al. [40] used an unsteady RANS solver and predicted the resistance and running attitude of a planing vessel at very high speeds, and they found an average error of 15 % when they comparing the numerical and experimental results.

Ozdemir et al. [41] analyzed a high speed craft with different turbulent models. They investigated the effects of turbulent models on solution and compared the experimental result with the result obtained from CFD analyses.

In Ghadimi et al. [42] RANS solver is implemented to model the motion of a planing hull in calm water with $k-\epsilon$ turbulent model and the steady state solution of a planing hull is investigated. It reports that numerical settings are inadequate to determine the performance of planing hull at very high speed condition.

In Fu et al. [43] the results from a collaborative research effort involving the different CFD codes were presented and discussed in which they examined the hydrodynamic forces, moments, hull pressures, accelerations, motions, and the multiphase free surface flow field generated by a planing craft at high speed ($Fr = 1.8 - 2.1$) in calm water and waves. A comparison of numerical data and experimental data for prismatic hull forms in a still water condition indicated that, at high Fr , the trim was under-predicted and the resistance over-predicted.

In Kansadamy et al. [44] a V&V full scale analysis was conducted for two high-speed semi-planing foil-assisted catamarans, and the comparison of the resistances showed that the error was in the range of 9.6 % to 15.5 % and the comparison of the trims indicated that the error was in the range of -44.1 to 0.8 %.

Yousefy et al. [45] conducted a comprehensive study on the existing numerical techniques for planing craft and they used several different commercially-available CFD software programs to determine the flow field around the planing hull.

Mousaviraad et al. [46] carried out a planing hull validation studies using one hull model of the historical benchmark experiments of Fridsma [47]. The simulation conditions include calm water in deep and shallow

conditions with fixed and free to sinkage and trim motions, as well as regular and irregular head waves in deep water free to heave and pitch motions. For simulations in calm deep water free to sinkage and trim, grid studies showed that refined grid density on the hull, especially over the spray root area, chines, and transom stern are necessary for accurate solutions. Detailed verification and validation studies are carried out for one speed ($Fr = 0.89$) with satisfactory results since monotonic convergence and validation are achieved for total resistance and trim (not for sinkage). For resistance, validation is achieved at the interval of $U_G = 3.8\%S$ with $E = 0.97\%D$. For trim validation is achieved at the interval of $U_G = 6.38\%S$ with $E = 5.1\%D$. The comparison error for resistance and trim are reported in the Figure 8.

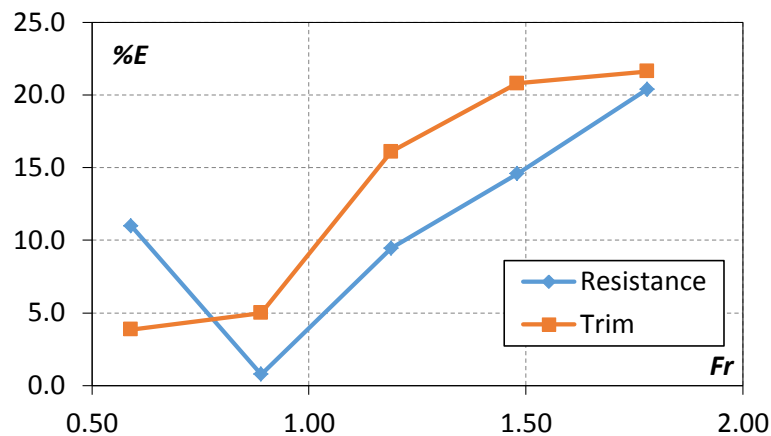


Figure 8 Comparison errors for whole Fr -range and for the finest grid used ($16.9 \cdot 10^6$ cells), source: Mousaviraad et al. [44]

Furthermore the authors highlighted that the non-accurate resolution of the tail of the main spray area was a cause of the simulation errors and, so, a very high grid resolution is required to accurately capture the details of the spray flow.

This overview evidences that for planing hull simulations estimating performance is still affected by relatively high error percentages. Furthermore the importance of dynamic equilibrium calculations in vessel performance prediction has been addressed by all of the above authors. The procedure used, changed over the years, according of the improvements in simulation techniques and computing capability, starting from the resolution of the flow around the hull with systematic variations of the model's position and attitude, and going to the dynamic simulation of the planing hull by moving mesh approach.

Then planing hull performance is the most sensitive to hull position (in particular respect to the displacement hull), making the additional equilibrium calculations essential. This problem is studied in the current work by using the Dynamic Fluid Body Interaction (DFBI) approach coupled with different moving mesh techniques.

4

BENCHMARK EXPERIMENTAL DATA

As explained in the introduction, for planing craft the largest errors in the resistance evaluations are related to the errors in the computing of pressure distribution on the bottom. This affects the dynamic trim and, consequently, the horizontal component of the lift (pressure resistance: $W \tan \tau$) and the viscous resistance through the errors in the wetted surface evaluation. Contrary to what happens on an indefinite plate, the difficulties in the identification of the pressure distribution are strictly related with the 3D nature of the flow due to the transversal pressure gradient working on a realistic hull bottom whose width is finite. This gradient is directly proportional to the slenderness ratio (L/B) and depends on the deadrise angle (β).

To take into account these elements, the V&V study reported in this work was performed to compare the numerical and experimental data of four models: three of the Naples Systematic Series (NSS) and one of the DIN Series. All of these models are presented hereunder.

1. The Naples warped hard chine systematic series (NSS)

The models of the NSS are chosen to highlight the influence of the L/B on the reliability of the numerical procedure. The NSS is composed of five models, four of which derived from the parent hull (C1), shown in Figure 9. The derived hulls are obtained scaling depth and breadth by the same reduction factors, with the aim of maintaining the homothetic forms of all of the transversal sections. These transformations increased the L/B .



Figure 9 Transversal and longitudinal sections of the C1 model

The three models chosen for the V&V procedure, *i.e.*, C1, C3, and C5, are characterized by the minimum, average and maximum values of L/B . Table 1 shows the main dimensions of the models.

Table 1 Main data of the five models of NSS

Model	C1	C2	C3	C4	C5
L_{OA} (m)	2.611	2.611	2.611	2.611	2.611
L_{WL} (m)	2.400	2.400	2.400	2.400	2.400
B_{WL} (m)	0.743	0.660	0.581	0.497	0.413
Δ (kg)	106.07	96.82	86.23	63.13	43.62
S_{WS} (m ²)	1.70	1.50	1.38	1.18	0.960
τ_S (deg)	0.0	0.0	0.0	0.0	0.0
L/B	3.45	3.89	4.45	5.19	6.25
$L/\nabla^{1/3}$	5.11	5.27	5.48	6.08	6.87

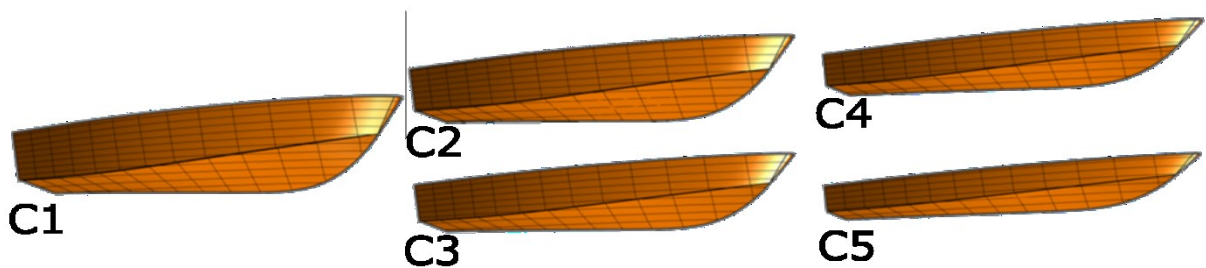


Figure 10 The five models of NSS

To assure the high quality of the benchmark-data (small U_D values), the ITTC's recommendations [37] are followed in order to maintain the highest quality of the experimental procedures.



Figure 11 Towing Tank of Naval division of DII

The tests are performed in the towing tank at the Naval Division of the *DII* of the Università degli Studi di Napoli "Federico II." The main dimensions of the towing tank are: length 136.0 m, width 9.0 m, and depth 4.5 m.

The models are tested, at Reynolds number (Re) $> 3.5 \times 10^6$, without turbulence stimulators, and they are restrained to avoid the effects of surge, sway, yaw and roll; they could undergo pitch and heave. The towing force was applied horizontally at the towing points, the coordinates of which are shown in Table 2.

Table 2 Towing point positions for the three models that are analyzed; T_H is the distance between the towing point and the base line; T_L is the longitudinal position equal to the longitudinal position of center of buoyancy (LCB).

<i>Model</i>	<i>C1</i>	<i>C3</i>	<i>C5</i>
T_H (m)	0.191	0.154	0.134
T_L (m)	0.945	0.945	0.945

All of the measurements are sampled at 500 Hz. Resistance, trim, and sinkage are analyzed in both the time and in frequency domain to assure the validity of each test. Moreover, before each test, the residual waves are measured to minimize noise and to make the tests comparable among all models.

The total error was evaluated according to ITTC's procedure [38], which recommends a criterion for the estimation of the total error of the total resistance coefficient (C_T) This method allows an evaluation of the propagation of the error due to the measurements of resistance, temperature, speed, and geometries of the models [39]. The procedure shows that the error is influenced mostly by the quality of the measurement of the load cell and, with less effect, by the estimations of the wetted surface. The total estimated errors are ± 0.1 N on resistance measurement, ± 0.05 degree on trim, ± 0.001 m/s on speed and ± 0.01 kg on weights. The detailed analysis of these errors that was done on models with comparable dimensions was reported in De Luca and Pensa [40].

The friction resistance coefficient (C_F) was evaluated according to the ITTC '57 friction line.

$$C_F = \frac{0.075}{(\log(Re) - 2)^2} \quad (36)$$

The Re was evaluated using the dynamic wetted keel length (L_K), as above indicated.

$$Re = \frac{L_k V}{\nu} \quad (37)$$

Finally, wave elevations are measured by two capacitive probes (still in comparison to the earth). The data logger was synchronized with the motion of the model in order to identify its actual position in respect to the wave pattern. Probe measurements are sampled at 100 Hz. The tests of wave cuts are performed on the C1 Model displacing 106.07 kg. The wave heights are measured at $V = 4.00, 5.00, 6.00,$ and 7.00 m/s ($Fr = 0.824, 1.031, 1.237,$ and 1.443 respectively), at 1.125 and 1.625 m from the centre-line of the hull.

2. The systematic series of DIN (SS-DIN)

The hull forms of the NSS models are strongly characterized by the warp of the bottom (*i.e.*, the reduction of β from the bow to the stern). To complete the V&V study a monohedral hull can be tested, in order to evaluate the influence of β on the generation of the transversal gradient of pressure. The monohedral model of the Systematic Series DIN (SS-DIN) was analyzed. This choice is significant also for the lower deadrise angle of the DIN model (17 deg instead of 23 deg, the mean value of NSS models). Some effects of the different bottom hull forms are shown in Appendix E.

Begovic and Bertorello [32] developed the SS-DIN of hard chine planing hull forms that is composed of four models: three warped and one monohedral. The profiles of the models are reported in Figure 12 and the models particulars are given in Table 3.

The models have the same transversal section with 16.7 deg deadrise angle at 0.25 L from the stern. Warped models had deadrise angle linearly varying along the hull length. The aim of the experimental program is the evaluation of the effect of deadrise angle variation along the hull length on hydrodynamic resistance and on seakeeping. The models have clear polycarbonate bottom to allow flow visualization and accurate wetted surface assessment.

Resistance tests were performed for speed coefficient C_V ranging from 0.56 to 3.92 and for two load coefficient values: $C_V = 0.428$ and 0.392.

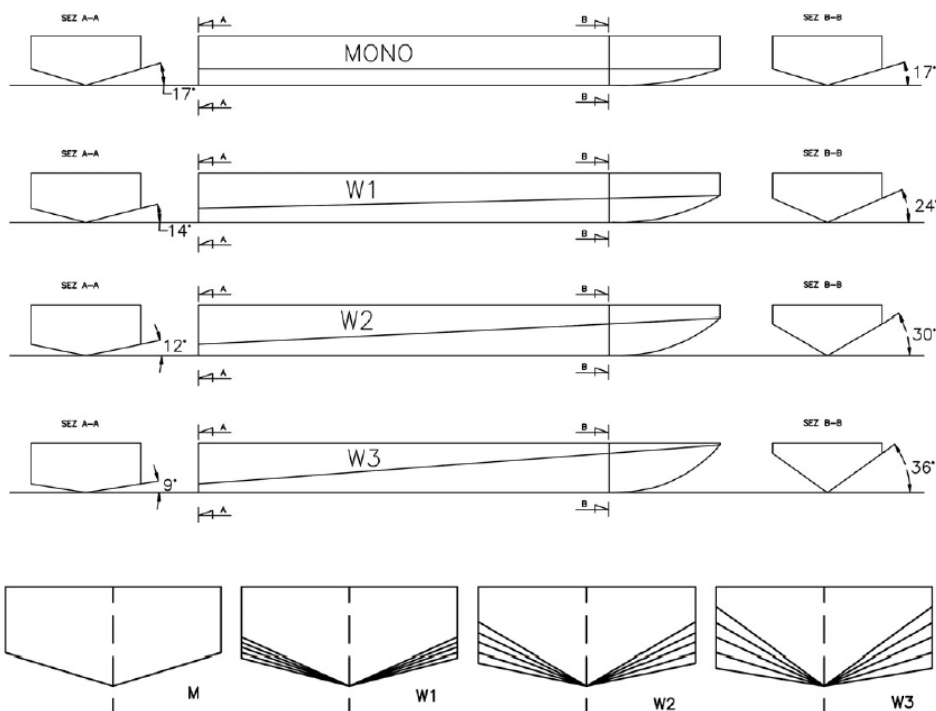


Figure 12 The profiles of Systematic Series DIN models, source: Begovic et al. [24]

Table 3 Main data of the SS-DIN models, source: Begovic et al. [24]

<i>Model</i>	<i>MONO</i>	<i>WARP 1</i>	<i>WARP 2</i>	<i>WARP 3</i>
L_{OA} (m)	1.900	1.900	1.900	1.900
B (m)	0.424	0.424	0.424	0.424
T_{AP} (m)	0.096	0.106	0.110	0.108
Δ_1 (N)	319.697	320.383	319.697	318.520
LCG (m)	0.697	0.660	0,609	0.586
τ (deg)	1.660	1.660	1,660	1.660
Δ_2 (N)	286.354	287.531	287,433	289.885
Fr	0.788 – 1.464	0.788 – 1.464	0.788 – 1.464	0.788 – 1.464
C_V	0.564 – 3.660	0.564 – 3.660	0.564 – 3.660	0.564 – 3.660
β	16.70	14.31 – 23.75	11.59 – 30.11	9.09 – 35.75
L/B	4.48	4.48	4.48	4.48
$L/\nabla_1^{1/3}$	6.00	5.99	6.00	6.00
$L/\nabla_2^{1/3}$	6.22	6.21	6.21	6.20

5

NUMERICAL METHODS

In this chapter the main aspects of the mathematical model of the CFD codes are described, and in particular the commercial code CD-Adapco Star CCM+, which is used to represent the physical model occurring in the typical hydrodynamics problems, focusing on the resistance test simulation of planing hull.

After the outline of the governing equations of the flow solver, aspects of the spatial and time discretization, the rigid body motion solver, the coupling with the flow simulation, and the dynamic mesh are treated in detail. All topics exposed are relevant for the consideration made in the following chapters.

1. Governing Equations

The governing equations for the fluid flow are the continuity and Navier – Stokes (NS) equations. Flows in the laminar regime are completely described by these set of equations and for simple cases the continuity and NS equations can be solved analytically. More complex flows can be tackled numerically with CFD techniques such as the Finite Volume Method (FVM) without additional approximations.

However many flows of engineering significance, and in particular in ship hydrodynamic field, are turbulent. Fluid engineers need access to viable tools capable of representing the effect of turbulence. The analysis of the physics of turbulence and its modeling in CFD is beyond the scope of the current work. Information about this topic is available in many texts, e. g. in Versteeg and Malalasekera [52]. It is important to note that the turbulence causes the appearance in the flow of eddies with a wide range of length and time scales that interact in a dynamically complex way. There are many numerical methods to capture the effects due to the turbulence. The methods can be grouped into the following three categories:

- Turbulence models for RANS equations (effect of turbulence on mean flow properties);
- Large Eddy Simulation (LES) (intermediate form of turbulence calculations);
- Direct Navier Stokes (DNS) (compute the mean flow and all turbulent velocity fluctuations).

For the most engineering purposes it is unnecessary to resolve the details of the turbulent fluctuations. CFD users are almost always satisfied with information about time-averaged properties of the flow (e.g. mean velocities, mean pressure, mean stresses, etc.). Therefore, the vast majority of the turbulent flow computation in the ship hydrodynamic field has been and will continue in the next years to be carried out with procedures based on the RANS equations.

In the RANS method the solver is applied to the following group of equations which express the mass continuity and the NS with a Reynolds time-average approach. The RANS equations can be expressed, in the typical hydrodynamic applications, as an incompressible flow as follows

$$\begin{cases} \nabla \cdot V = 0 \\ \rho \frac{\partial V}{\partial t} = -\nabla P + \mu \Delta V + \nabla \cdot T_{RE} + S_M \end{cases} \quad (38)$$

Where V is the Reynolds averaged flow velocity vector, P is the average pressure field, μ is the dynamic viscosity, T_{Re} is the tensor of Reynolds stresses and S_M is the vector of momentum sources.

The component of T_{Re} is computed using the selected turbulence model, in agreement with the Boussinesq hypothesis:

$$\tau_{ij}^{Re} = \mu_t \left(\frac{\partial V_i}{\partial x_j} + \frac{\partial V_j}{\partial x_i} \right) - \frac{2}{3} \rho k \delta_{ij} \quad (39)$$

Where μ_t is the turbulent viscosity, k is the turbulent kinetic energy. There are a lot of turbulence models that can be used to close the hydrodynamic problem in the RANS method. In particular in the hydrodynamic field, the widely used turbulence models are those two-equation models, such as the $k-\omega$ SST [53] and the Realizable $k-\epsilon$.

Finally, in order to discretize the physical model, the RANS solver is based on the FVM.

2. Spatial discretization schemes

The convection and diffusion terms in equation 38 are discretized using different numerical schemes that estimate the face values of the flow variables. Most often, diffusion terms are discretized by using a Central Differencing (CD) scheme where the face values are calculated by interpolation between the closest cells. In order to discretize the convection terms, the flow direction has to be taken into account.

The easiest way is to let the face value between two cells be equal to the value of the first upstream cell which is done in the first order upwind scheme. In the second order upwind scheme, the face value is calculated from the two closest upwind cells.

It is usually recommended to start a numerical solution process with lower order schemes, such as the first order upwind scheme, since they are very stable. However, the low accuracy of these schemes can lead to a high degree of unphysical diffusion in the solution, known as numerical diffusion.

The second order upwind scheme is often considered as a suitable discretization scheme since it exhibits a good balance between numerical accuracy and stability.

3. The Finite Volume Method (FVM)

The FVM is a numerical method of discretizing a continuous Partial Differential Equation (PDE), into a set of algebraic equations. The first step of the discretization is to divide the computational domain into a finite number of volumes, forming what is called a mesh or a grid. Next, the PDE is integrated in each volume by using the divergence theorem, yielding an algebraic equation for each cell. In the cells' centers, cell-averaged values of the flow variables are stored in so called nodes. This implies that the spatial resolution of the solution is limited by the cell size since the flow variables do not vary inside a cell. The FVM is conservative, meaning that the flux leaving a cell through one of its boundaries is equal to the flux entering the adjacent cell through the same boundary. This property makes it advantageous for problems in fluid dynamics.

All the CFD models that use fully three-dimensional viscous formulations are typically of the FVM formulation, which need the computational domain to be discretized into a finite number of three dimensional volumes. The solution mesh may be created using either a structured or unstructured approach. The structured approach requires a 1:1 mapping of grid points in the domain. Unstructured mesh thus greatly simplifies mesh generation for complex geometries, and allows higher quality meshes to be created which result in greater numerical accuracy and faster computation times. The pros and cons of the two different mesh types were summarized in Table 4.

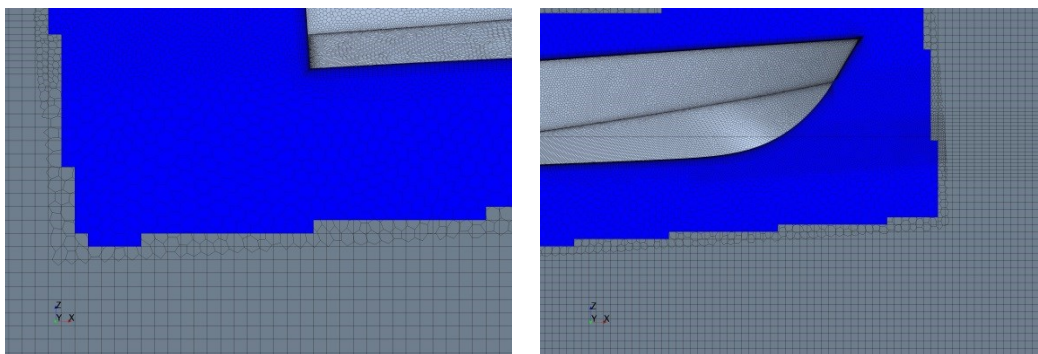


Figure 13 Example of structured (green) and unstructured (blue) mesh

The structured mesh is the fastest and uses the least amount of memory for a given number of cells. Multi-part or multi-region meshes with a conformal mesh interface are allowed. The structured meshing model employs in 3D cases the hexahedral cell shape in order to build the core mesh. In CD-Adapco Star CCM+, the Delaunay method is used to construct the mesh, which iteratively inserts points into the domain, forming high-quality hexahedral in the process. The resulting mesh strictly conforms to the triangulation of the surface at the domain boundary, so the quality of the original surface mesh must be good to ensure a good quality volume mesh.

The unstructured meshes provide a balanced solution for complex mesh generation problems. They are relatively easy and efficient to build, requiring no more surface preparation than the equivalent hexahedral mesh. They also contain approximately five times fewer cells than a hexahedral mesh for a given starting

surface. Multi-region meshes with a conformal mesh interface are allowed. The unstructured meshing model generally utilizes an arbitrary tetrahedral cell shape in order to build the core mesh.

The CD-Adapco Star CCM+ code has the distinction of use the polyhedral cell shape for unstructured mesh.

Table 4 Pros and cons of the structured and unstructured mesh type, source CD-Adapco User's Guide [54]

	Structured	Unstructured
Geometric Flexibility	less	greater
Adaptability of grid	less	greater
Suitability to the calculation of viscous flows (cells with a high aspect ratio)	greater	less
Deformable Grid	less	greater
Amount of Memory Required	greater	less
CPU Power Required	greater	less

4. Pressure-velocity coupling method

The RANS equations contain one continuity equation and three momentum equations, if a 3D system is considered. There are four unknown variables in these equations, the pressure and the three velocity components. The problem is that there is no equation for the pressure, so the continuity equation must be used as an indirect equation for the pressure. This is achieved by using a pressure-velocity coupling, which can be either segregated or coupled. The properties of these two groups of algorithms will be described briefly; a more thorough explanation has been given by Versteeg and Malalasekera [49].

The semi-implicit method for pressure linked equations (SIMPLE) is a segregated algorithm that solves each equation separately. This model solves the flow equations (one for each component of velocity, and one for pressure) in a segregated, or uncoupled, manner. The linkage between the momentum and continuity equations is achieved with a predictor-corrector approach. First, a pressure is assumed and the velocities are calculated from the momentum equations. If the continuity equation is not satisfied by these velocities, the pressure is modified and the velocities are calculated again.

The complete formulation can be described with a SIMPLE-type algorithm. This model has its roots in constant density flows. Although it can handle mildly compressible flows and low Rayleigh number natural convection flow, but it is not suitable for shock-capturing, high Mach number, and high Rayleigh-number applications.

5. Temporal discretization schemes

For transient problems, the transport equation must also be discretized in time. This is done by integrating the PDE over a time step (Δt) in addition to the spatial discretization. In order to solve this integrated equation, the cell values of the flow variables must be evaluated at a certain time.

Implicit time integration means that the flow variables are evaluated at the future time, $t+\Delta t$. Since these are not known in the current time step, implicit time integration requires iteration. In comparison to explicit time integration, where the flow variables are evaluated at the current time so that iteration is avoided, implicit time integration is more computationally expensive. On the other hand, implicit time integration is unconditionally stable, meaning that it is stable for all time step sizes. The implicit unsteady model is the only unsteady model available with the SIMPLE segregated flow algorithm. The unsteady model is required in simulations with:

- Time-varying boundary conditions;
- Moving mesh problems;
- Free surface problems;
- Transient heat transfer.

In the implicit unsteady approach, each time-step involves some number of inner iterations to converge the solution for that given instant of time. The number of inner iterations in the time-step is harder to quantify. Generally, this number is determined by observing the effect that it has on results. Smaller time steps generally mean that the solution is changing less from one time step to the next; fewer inner iterations are then required.

The Courant Friedrichs Lewy (CFL) number is a helpful indication for selecting the time step size: for time accurate simulations, the CFL number should be one on average in the zone of the interest. This value implies that the fluid moves by about one cell per time step.

There is an optimal balance of time-step size and number of inner iterations for a given problem and desired transient accuracy (Figure 14). If the convergence of iterations is slow, the time-step is too large and there are significant temporal discretization errors. Generally is better to reduce the time step than to perform much iteration within a large time step.

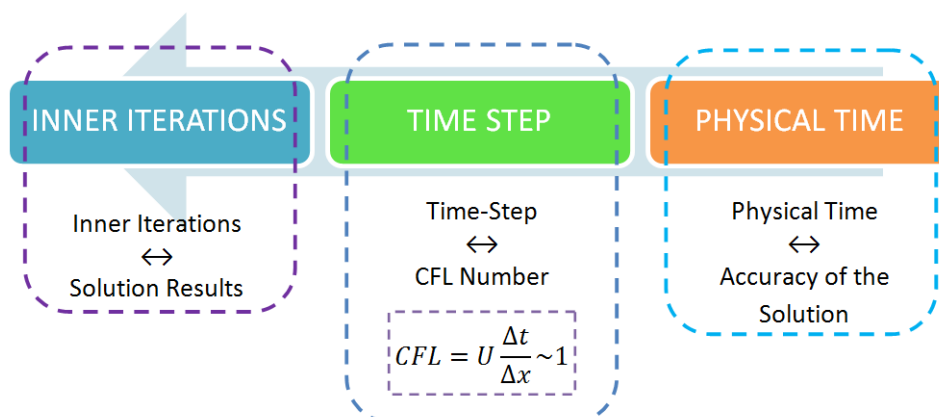


Figure 14 Time Step Setup

6. The Free Surface Models

As above mentioned, for ship hydrodynamic problems a peculiarity is the presence of water free-surface. For simulation of viscous free surface flow, several different theoretical models exist. Since large differences in the treatment of the water surface exist. A popular classification of water surface models is reported in Wackers et al. [55].

- Fitting methods, where the grid is deformed and free-surface boundary conditions are applied to a boundary of the grid. These methods are usually solved in an iterative process, where alternately the flow field is computed and the grid is deformed to match the current shape of the wave surface.
- Interface Capturing methods with reconstruction. For these methods the grid is not necessarily deformed; the interface is defined as a surface that cuts through the grid. Initially, this surface was defined by convecting marker particles on the surface with the flow field. Later, variants of the volume of fluid (VOF) method used the convected value of the water volume fraction in cells to determine the surface location. The latest addition to these methods is the level-set method, where the plane is defined by a convected continuous function.
- Interface Capturing methods without reconstruction. For these methods, like the original VOF method as formulated by Hirt and Nichols [56], a volume fraction equation determines the amount of each fluid in the cells and local fluid properties are set as a mixture of the two pure-fluid properties according to this volume fraction. No attempt is made to reconstruct the interface; instead it appears as a numerical discontinuity in the volume fraction.

The comparison of the different free-surface simulation techniques available in the existing CFD codes are reported in the report of Gothenburg 2010 workshop [2], as shown in Figure 15. The VOF method is by far most popular choice. Level-set method is slightly popular and formed the second largest group (5 codes, 17%). Only 3 of the 33 existing codes (9%) used the free-surface fitting methods.

Gothenburg 2010 - Free Surface Models

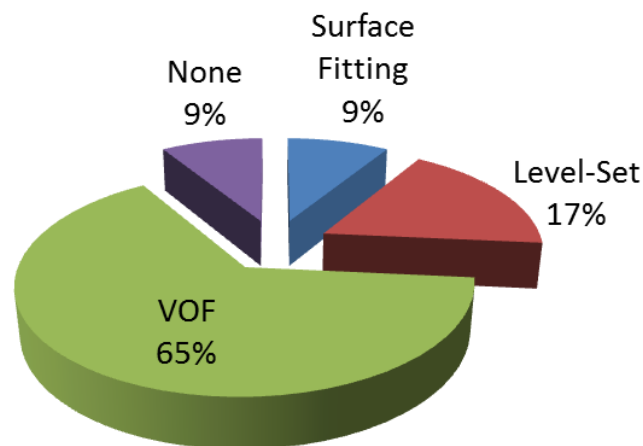


Figure 15 Gothenburg Workshop 2010 – free surface models in the widely used CFD codes, source:

Bohm [57]

a. VOF discretization schemes

As above mentioned, the VOF method is the widely used free-surface scheme and the CD-Adapco Star CCM+ uses this method. The VOF employs the concept of an equivalent fluid. This approach assumes that the (two) fluid phases share the same velocity and pressure fields thereby allowing them to be solved with the same set of governing equations describing momentum and mass transport as in a single phase flow. The volume fraction α_i of the i^{th} phase describes to which level the cell is filled with the respective fluid.

$$\alpha_i = \frac{V_i}{V} \quad (40)$$

The VOF approach is suitable, when the grid is fine enough to resolve the interface between two immiscible fluids and it is a simple multiphase model. The free surface is then defined as the isosurface at which the volume fractions take the value of 0.5, as shown in Figure 16. It is important to note, that this location is not at the control volume center but rather interpolated to the geometrical value.

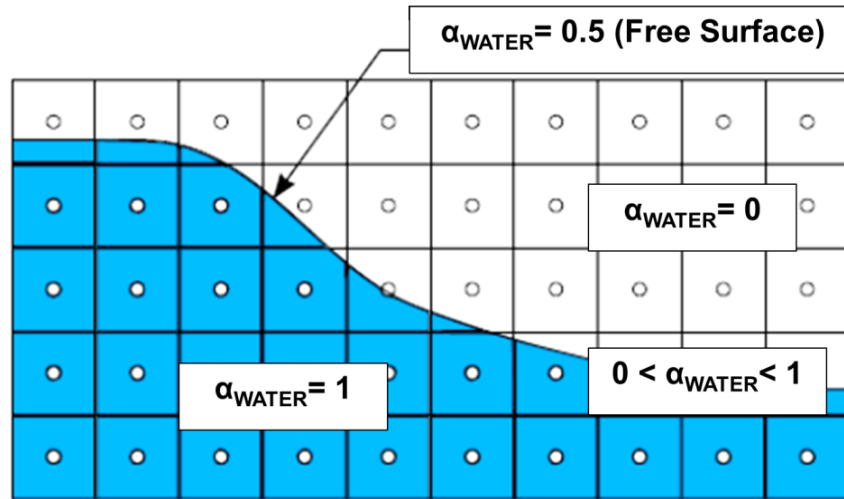


Figure 16 Visualization of air and water volume fractions and related free-surface, source: CD-Adapco User's Guide [54]

To simulate wave dynamics, one has solved an equation for the filled fraction of each control volume in addition to the equations for conservation of mass and momentum. Assuming incompressible flow, the transport equation of volume fractions is described by the following conservation equation.

$$\frac{\partial}{\partial t} \int_V \alpha_i dV + \int_V \alpha_i (V - V_b) n dS = 0 \quad (41)$$

The physical properties of the equivalent fluid within a control volume are then calculated as functions of the physical properties of the phases and their volume fractions.

$$\begin{cases} \rho = \sum_i \rho_i \alpha_i \\ \mu = \sum_i \mu_i \alpha_i \\ 1 = \sum_i \alpha_i \end{cases} \quad (42)$$

Strict conservation of mass is crucial, but this is easily obtained within this method as long as it is guaranteed that equation 42 is fulfilled.

The critical issue for this kind of methods is the discretization of the convective term. Low-order terms like for instance first order upwind are known to smear the interface and introduce artificial mixing of the two fluids. Therefore higher order schemes are preferred. The goal is to derive schemes which are able to keep the interface sharp and produce a monotone profile over the interface. All of these schemes are based on the Normalized Variable Diagram (NVD) and the Convection Boundedness Criterion (CBC).

b. Normalized Variable Diagram (NVD)

The NVD provides a framework for the development of convective schemes which in combination with the CBC guarantees boundedness of the solution. In context of the NVD, boundedness allows to create convection schemes which are both stable and accurate. All elementary schemes have certain advantages and disadvantages. Pure upwind schemes are stable but diffusive. The central differencing scheme is more accurate but introduces propagating dispersion which may lead to unphysical oscillations in large regions of the solution. Therefore, practical schemes are often designed as a blending of upwind, downwind and central differencing schemes to obtain the desired properties. The advantage of the NVD is its simplicity. For a 1 D case the NVD takes the following form.

The Figure 17 shows three cells in the vicinity of a cell face f , across which the velocity v_f is known. The nodal variable values are labelled, α_D , α_C and α_U , representing the downwind, central, and upwind positions relative to each other.

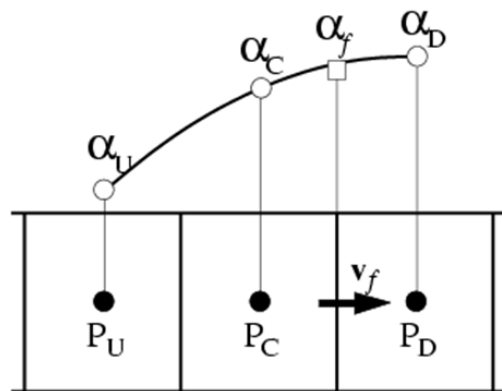


Figure 17 Upwind, downwind, and central cells that are used in the analysis

The normalized variable $\xi(r, t)$ in the vicinity of face f is defined as:

$$\xi(r, t) = \frac{\alpha(r, t) - \alpha_U}{\alpha_D - \alpha_U} \quad (43)$$

And the normalized face value:

$$\xi_f = \frac{\alpha_f - \alpha_U}{\alpha_D - \alpha_U} \quad (44)$$

With this definition any differencing scheme using only nodal values at point U, C and D to evaluate α_f may be written as

$$\xi_f = \xi_f(\xi_C) \quad (45)$$

To avoid that the solution oscillates unphysical, α_C has to be locally bounded between α_U and α_D :

$$\alpha_U \leq \alpha_C \leq \alpha_D \quad (46)$$

If this criterion is satisfied for every point in the solution domain, then no unphysical oscillations will occur, for example, the phase volume fraction cannot become negative, or larger than unity.

According to the CBC, a numerical approximation of ξ_f is bounded, if are achieved the following conditions:

- For $0 \leq \xi_C \leq 1$ the bounded region lies above the line $\xi_f = \xi_C$ and below $\xi_f = 1$.
- For $\xi_C \leq 0$ and $\xi_C > 1$, $\xi_f = \xi_C$.

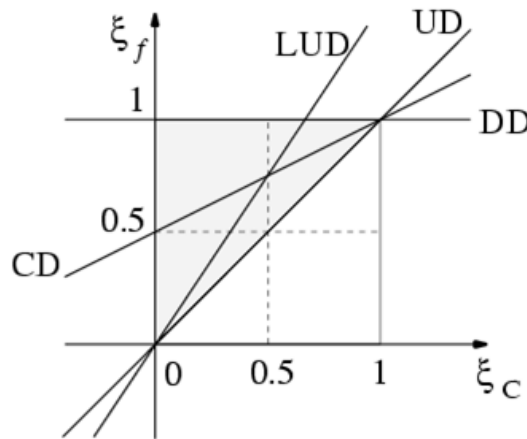


Figure 18 The NVD with the linear schemes: Central Differencing (CD) and Linear Upwind Differencing (LUD): the shaded area shows the zone for which the CBC is valid.

Observing the Figure 18, it has to be noted that, with exception of UD, none of these linear schemes (CD and LUD) fulfil the boundedness criterion. So it can be concluded that the linear schemes either lack stability or accuracy. The need for boundedness, stability and accuracy consequently led to the desire to combine the advantages of the different linear schemes. This led to the development of nonlinear schemes.

Lower order numerical schemes are bounded but will smear out the interface due to numerical diffusion while higher order schemes are more accurate but less stable.

A combination of higher and lower order schemes is often used like in HRIC and the Compressive schemes used in CD-Adapco STAR CCM+ and in most commercial and not CFD codes. More details about the different Interface Capturing schemes are available in Wackers et al. [55].

c. HRIC scheme

The High-Resolution Interface Capturing (HRIC) scheme is designed to mimic the convective transport of immiscible fluid components, resulting in a scheme that is suited for tracking sharp interfaces, that is an important quality of an immiscible phase mixture (for example, air and water).

The HRIC scheme, based on the Compressive Interface Capturing Scheme for Arbitrary Meshes (CICSAM) introduced by Ubbink [58] and developed by Muzafferija and Peric [59], uses a combination of upwind and downwind interpolation. Its aim is to combine the compressive properties of the downwind differencing scheme with the stability of the upwind scheme. The blending of the schemes in each cell is a function of the volume fraction distribution over the neighboring cells. The value of the flow variable is then corrected by the local value of the CFL number.

The bounded downwind scheme is formulated as:

$$\xi_f = \begin{cases} \xi_c & \text{if } \xi_c < 0 \\ 2\xi_c & \text{if } 0 \leq \xi_c \leq 0.5 \\ 1 & \text{if } 0.5 \leq \xi_c \leq 1 \\ \xi_c & \text{if } 1 \leq \xi_c \end{cases} \quad (47)$$

Since the amount of one fluid convected through a cell face shall be less or equal than amount available in the donor cell, the calculated value of ξ_f is corrected with respect to the local CFL number. The correction takes the form of equation below reported and effectively controls the blending between HRIC and UD scheme with two limiting Courant numbers CFL_L and CFL_U which normally takes values of 0.5 and 1.0 respectively.

$$\xi_f^* = \begin{cases} \xi_f & CFL < CFL_L \\ \xi_C + (\xi_f - \xi_C) \frac{CFL_U - CFL}{CFL_U - CFL_L} & CFL_L \leq CFL \leq CFL_U \\ \xi_C & CFL_U < CFL \end{cases} \quad (48)$$

Effectively, this correction implies that the HRIC scheme is used for a local CFL smaller than the CFL_L limiter and UD scheme for CFL equal or greater than the CFL_U limiter. Between those values a blending of both schemes is used. This correction is applied to improve robustness and stability when large time variation of the free surface shape is present and the time step is too big to resolve it.

The HRIC scheme is the currently most successful advection schemes and widely used in many CFD codes. Nevertheless various authors, including Andrilion and Alessandrini [60] and Ferziger and Peric [61], have found that the local CFL dependency scheme can cause the spread of the free surface interface, and this could be the main cause of the artificial mixing of air and water. This problem is nominally known as Numerical Ventilation (NV).

7. The Numerical Ventilation problem

For the typical ship hydrodynamic problems the NV problem in the VOF method causes that all the forces evaluated in these cells are not corrected. For example, as shown in Figure 19, if in a cell on the bottom of the hull the VOF values is equal to 0.5 instead of the physic value of 1.0 (fully water) the viscosity in this region will be just an half of the water viscosity plus an half of the air viscosity and so far the shear force calculated in this cell will be just an half of the real one; the same happens for buoyancy and for all the other calculated values. That could lead to important divergence problems on the hull bottom. Indeed the VOF method fills the mesh cells cut by the free surface, with a fraction of water (between 0% and 100%) and the complement of air, so that, those cells have a hybrid fluid obtained by a relative mixture of the two fluids, air and water, with material proprieties, density and viscosity, that correspond to the weighted average of filling ratio of each fluid in the cell. The transport equation, then, diffuses the mixture from partially filled cells to the contiguous ones, bringing the flow mixture below the entire hull bottom.

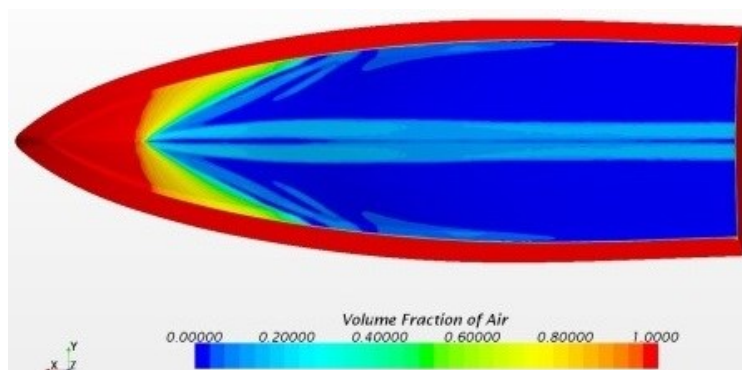


Figure 19 Example of numerical ventilation problem on the bottom of the planing hull

This problem can be reduced through a very high refinement of cells around the free surface in the spray region in order to minimize a non-physical inclusion of air under the hull; however the mesh improvements not resolve it at all as indicated by Federici [62].

In this work different ways of solution of the NV problem are investigated, such as the artificial suppression of the abnormal mixing of air and water on the hull bottom, similarly to what proposed by Viola et al. [63], and the modify of HRIC scheme through the removal of the local CFL dependency, as proposed in Bohm [57].

8. The Rigid body motion

The 6 Degrees of Freedom (6-DOF) models solve for the rigid body motion of an object exposed to fluid forces. The 6-DOF body is created with a Dynamic Fluid Body Interaction (DFBI) motion. This approach is suitable for the hydrodynamic simulations that required capability to capture the changing of position of position of the hull during the simulation.

The model DFBI is used to simulate the motion of a rigid body in response to pressure and shear forces that the fluid exerts on the body. The code calculates the resultant force and moment acting on the body due to all influences, and solves the governing equations of rigid body motion to find the new position of the rigid body relative to the body local coordinate system, as reported in CD-Adapco User's Guide [54]:

$$\begin{aligned} m \frac{dv}{dt} &= f \\ I \frac{d\vec{\omega}}{dt} + \vec{\omega} \times I \vec{\omega} &= n \end{aligned} \tag{49}$$

Where:

- m is the mass of the body.
- f is the resultant of the forces acting on the body.
- v is the speed of the center of mass.
- I is the tensor of the moments of inertia.
- $\vec{\omega}$ is the angular velocity.
- n is the moment of the resultant force acting on the body.

The force and the resulting moment acting on the body are obtained by the fluid pressure and shear forces acting on each face of the boundaries of the body. The workflow of the rigid body motion technique is shown in Figure 20.

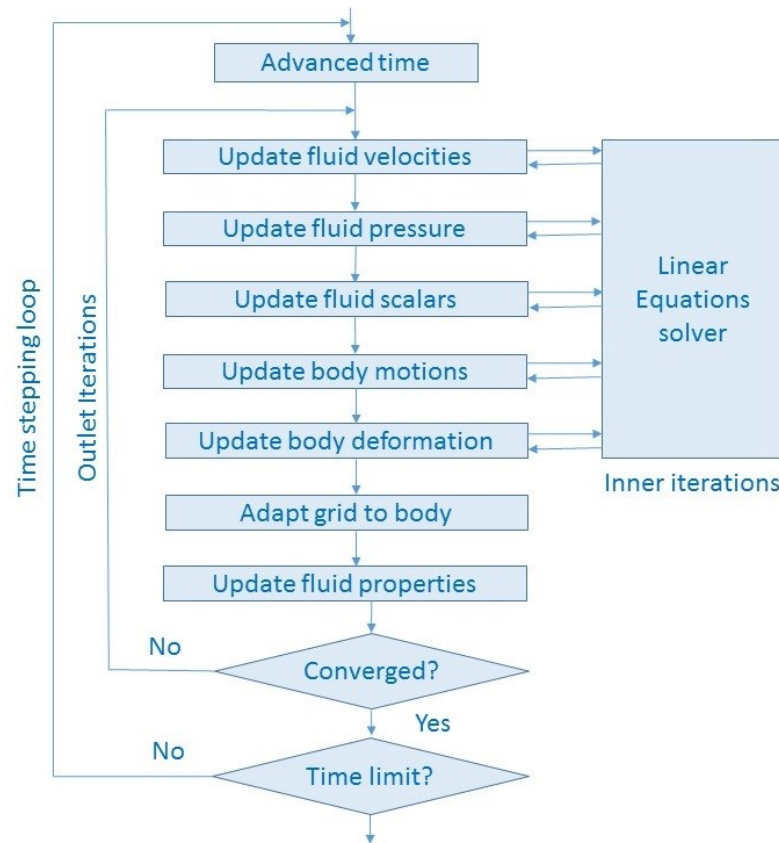


Figure 20 Workflow of rigid body motion

9. Dynamic meshing

To be able to handle motion, the mesh structure has to change dynamically with the moving object. There are different methods for the dynamic movement of the mesh. The three that are most suitable for hull simulations are the simple moving grid, the diffusion-based smoothing method/morphing grid, and the Overset/Chimera grid. The concepts of the three methods are described in the following sections.

a. Moving grid

Within this method, the entire grid is moved according to the motions of the rigid body. The grid itself is not altered but instead kept rigid. This approach bears several advantages. Since only the flow variables have to be corrected according to the body motion, the method is very robust and the computational effort overhead is small. On the other side, the method is only applicable for the motion of one rigid body.

As regards the application of this technique to the simulation of resistance test of planing hull, there are two main and significant drawbacks.

The first one is the care which has to be taken to smoothly resolve the free surface interface. Figure 21 shows a plane of a grid with the free water surface included. One can see that the grid pattern on the stern of the hull follows the free surface contour, while increasing the trim angle grid pattern no longer follows the water free surface.

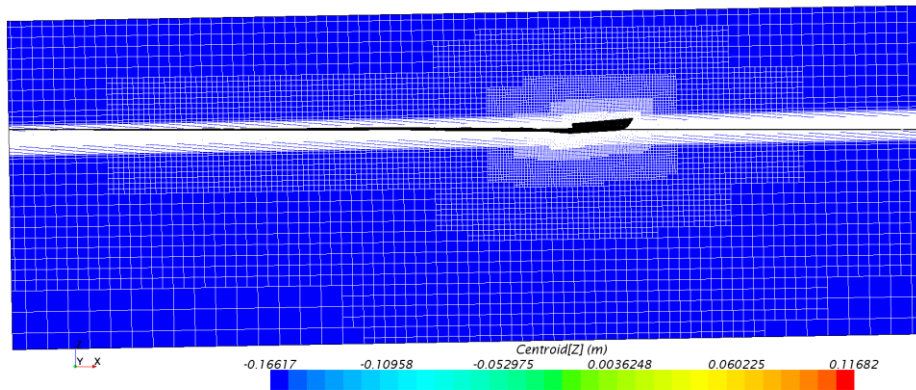


Figure 21 Resistance test simulation of planing hull using moving grid with free-surface and mesh visualization

The second drawback is connected with the first one. Indeed during the simulation of resistance test, in particular for planing hull, there is, in the initial phase, oscillations of the trim and sinkage of the hull caused the variation of height of the water plane at the inlet and outlet boundaries, as reported by Viola et al. [63]. Such oscillations introduce a “fake-wave” into the computational domain, which can induce additional oscillation of the trim, sinkage, and resistance of the hull. This “fake-wave” can affect the convergence significantly.

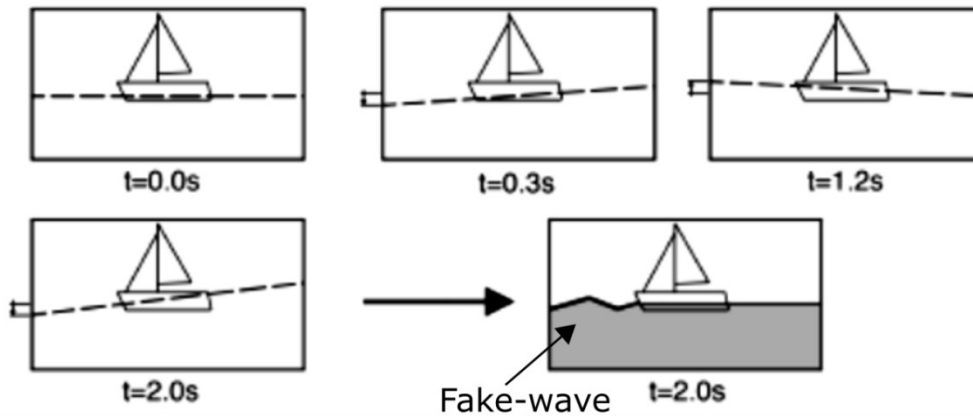


Figure 22 Schematic drawing of the free surface perturbation and “fake-wave” due to the moving grid for inlet boundary, source: Viola et al. [63]

In order to minimize the generation of “fake-wave” and to avoid that the grid pattern no longer follows the water free surface, there are some tricks. For example:

- The upstream inlet face should be as close as possible to the boat and the hull.
- If the final sink and trim are known, these values should be used as the initial conditions for positioning the hull.
- Use of the damping function on the wave surface near the boundaries.

- The pitching inertia can be increased respect the experimental (and real) value to speed up the convergence.
- Extension of the height of the grid refinement for the water free surface (high increase of number of cells).

However some of these tricks can be a source of error, increase uncertainty, reduce the reliability of the simulation, and increase the computational effort. For these reasons alternative solutions to the simple moving grid technique are checked.

b. Overset/Chimera grid method

The overset/chimera grid method uses two regions of meshes, one for the moving part and one for the stationary background. The moving part, referred to as the overset mesh, uses the mesh rotation and translation method where the fluid mesh is replaced with a rigid body mesh. All cells maintain their shape and the mesh motion is described by a displacement vector and rotation angles. In the case when having a solid that interacts with the fluid, the position of the mesh is determined by solving the equations of the motion and rotation of the body.

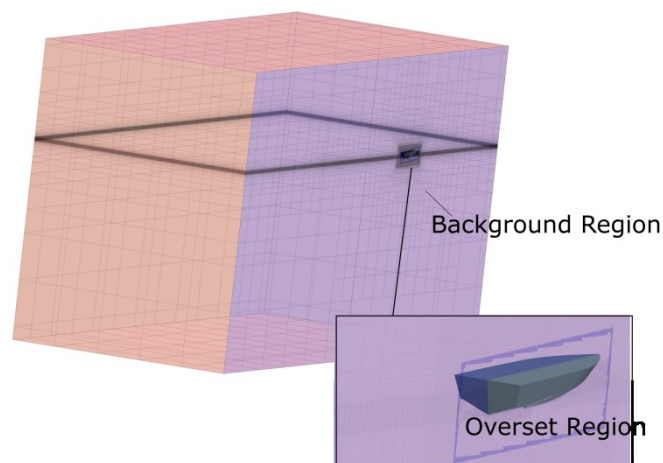


Figure 23 The overset/chimera grid with the two regions: moving region (overset) and stationary region (background)

It is important to observe that this approach is not a conventional way to rank the performances of the hulls in the still water condition. Only a few researchers have used this approach, e.g. Carrica et al. [64] and Bertorello et al. [5]. Usually this technique is used for numerical simulation of maneuvering tests, roll decay tests and to estimate the ship's response to waves, e.g. Tezdogan et al. [65], Begovic et al. [66], and Swidan et al. [67].

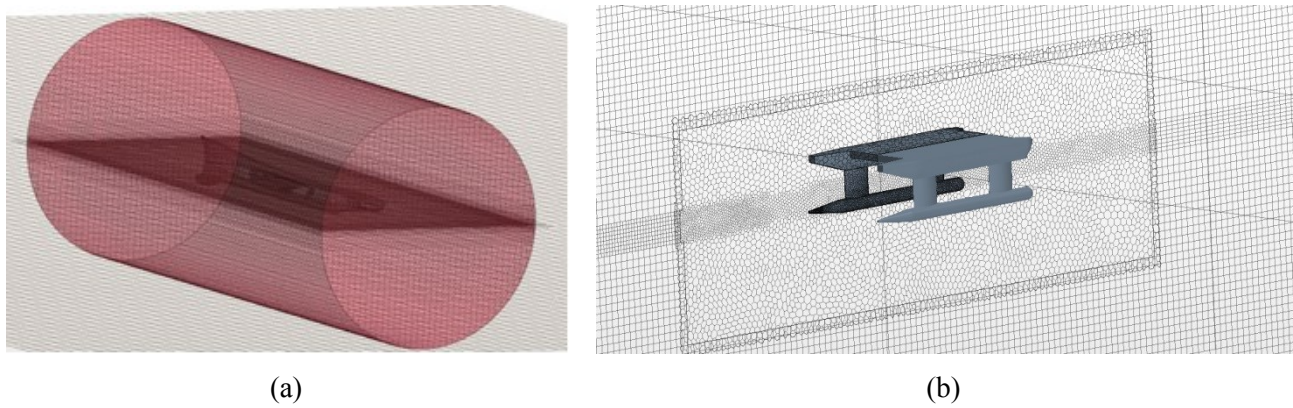


Figure 24 Particular of overset region in two different test cases: (a) Roll damping assessment [52] and (b) resistance in still water for SWATH hull [50]

To establish the connectivity between the background and the overset regions, a two-step overset assembly process takes place in the following way. The cells around the interface of the overset mesh are identified and labelled as donor cells. Then the cells in the background closest to the donor cells are identified and set as acceptor cells. These cells have to form a continuous layer of cells around the overset mesh. The background cells that are completely covered by the overset region are inactivated (the hole cutting process). The donor and acceptor cells transfer information between the meshes. Each acceptor cell has one or more donor cells. The set of donor cells depends on the interpolation option chosen and on the number of active cells in the donor region around the acceptor cell centroid.

As reported in CD Adapco User's Guide [54], the interpolation schemes are:

1. Distance-weighted, where the interpolation factors are inversely proportional to the distance from acceptor to donor cell center, resulting in the closest cell giving the largest contribution. This involves 3 donor cells (in 2D case) or 4 (in 3D case).
2. Least squares, consider mapping data from faces of the background mesh to faces of the overset mesh using a least squares scheme. Assuming a face in a cell of the background mesh (Face 0), as the closest to a face (Face A) of the target cell (in the overset region). The neighbors of Face 0 are defined as any face that shares at least one vertex with Face 0. These neighbors are included as part of the interpolation stencil. The solver uses the second-order terms of a Taylor series expansion as a "cost function" to approximate the error of the function distribution at assigned point. It then minimizes the cost function in equation for the function at the target point A.
The drawback of a neighbor-based least squares scheme is that some of the faces of the background mesh that the target face imprints upon are not included in the stencil. More details of the neighbor-based least squares scheme are reported in CD Adapco User's Guide [54].
3. Linear interpolation using shape functions spanning a triangle (in 2D case) or a tetrahedron (in 3D case) defined by centroids of the donor cells. This option is more accurate, but also more expensive in terms of calculation effort.

The interpolation function is built directly into the coefficient matrix of the algebraic equation system.

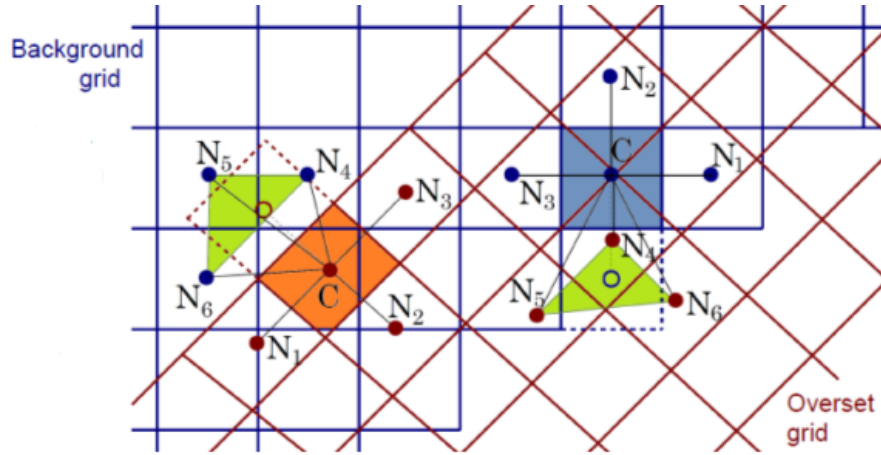


Figure 25 Connectivity between the background and the overset regions, source: *CD-Adapco User's Guide [54]*

In the Figure 25, two acceptor cells are shown using dashed lines, one in the background mesh and one in the overset mesh. The fluxes through the cell face between the last active cell and the acceptor cell are approximated in the same way as between two active cells.

However, whenever the variable value at the acceptor cell centroid (marked by the open symbols in the Figure 25) is calculated by the weighted variable values at the donor cells using the following expression:

$$\varphi_{\text{acceptor}} = \sum \alpha_i \varphi_i \quad (50)$$

Where α_i is the interpolation weighting factor, φ_i is the value of the dependent variable φ at donor cells N_i and subscript i runs over all donor nodes of an interpolation element (denoted by the green triangles in the figure). This way, the algebraic equation for the cell “C” in the above figure involves three neighbor cells from the same mesh (N_1 to N_3) and three cells from the overlapping mesh (N_4 to N_6).

The advantage with the overset method is that only a certain part of the mesh is moving without requirement for altering the grid topology. A drawback is that the interpolation between the meshes can cause numerical errors and increase the computational effort. The pros and cons of the overset mesh were reported in Table 5.

c. Smoothing/Morphing mesh

The dynamic meshing can be incorporated using smoothing methods, also called morphing mesh technique, where the cells are moved with a deforming boundary while the number of cells and their connectivity remain unchanged. The morphing mesh is suitable for complicated and arbitrary relative motion and for relatively small boundary deformations, while larger deformations may require generation of new cells in order to maintain a high quality mesh. One smoothing method is the diffusion-based smoothing, where the motion of the cells is modelled as a diffusive process.

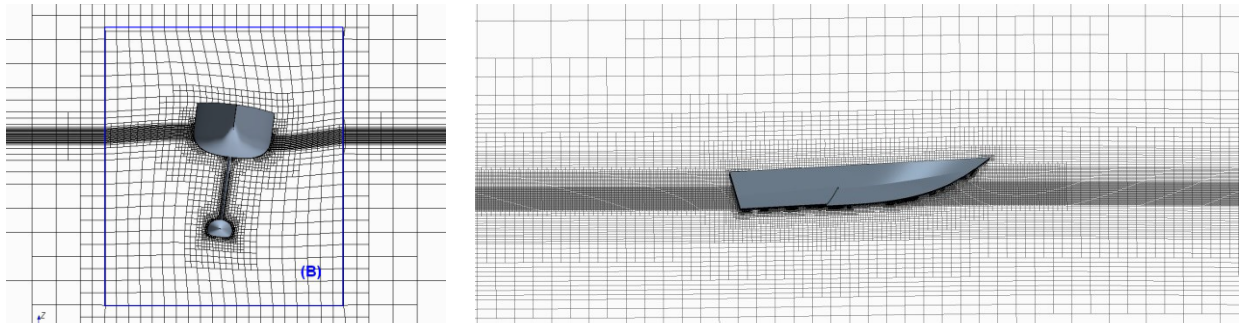


Figure 26 Examples of application of smoothing/morphing mesh in marine hydrodynamics application: (left) sail yacht, source: Bohm [45]; (right) planing hull simulation

Traditionally the morphing mesh can be used to model scenarios where components deform and change shape, e.g. in marine application field: Kang et al. [68] and Biancolini and Viola [69]. However this technique was never used in ship hydrodynamics for resistance test simulations.

The morphing mesh can be employed easily for the rigid body motion case. During the process of morphing, the mesh vertices are redistributed in response to the movement of a set of control points. The morpher solver, as reported in CD-Adapco User's Guide [54], takes the control points and their associated displacements and generates an interpolation field. The interpolation field is then used to displace the vertices of the mesh based on Radial Basis Functions (RBF) method.

To generate the interpolation field, a system of equations is solved, using the control vertices and their specified displacements: for every control vertex i , its displacement d_i' is approximated with the combination:

$$d_i' = \sum_{j=1}^n \lambda_j \sqrt{r_{ij}^2 + c_j^2} + y \quad (51)$$

$$r_{ij} = \|x_i - x_j\|$$

Where r_{ij} is the magnitude of the distance between two vertices, λ_j is the expansion coefficient, x_i the position of i -vertex, n is the number of control vertices, c_j the basis constant, and y a constant value. More details about the RBF method and the morphing mesh technique are reported in de Boer et al. [70] and Biancolini [71]. At the moment wide information about computational effort for morphing grid are not available in literatures, as reported in Table 5.

Table 5 Pros and cons of the overset and morphing mesh, source CD-Adapco User's Guide [54]

	Chimera/Overset Grid	Morphing Grid
Geometric Flexibility	greater	greater
Adaptability of grid	less	greater
Suitability to the calculation of viscous flows (cells with a high aspect ratio)	greater	greater
Deformable Grid	greater	medium
Amount of Memory Required	greater	uncertain
CPU Power Required	greater	uncertain

6

MODELING ANALYSIS

This section reports the preliminary analysis of C1 model, at the displacement condition of 106.7 kg, to determine the best configuration setup, in relation to accuracy of the results and the computational effort required, as well as to reduce the δ_{SM} .

The variables analyzed were C_T , C_F , dynamic trim angle (τ) and dynamic wetted surface (S_w), and the details of the numerical approaches used in this study for all performed simulations are reported.

1. Introduction

The planning of simulations performed for the modeling analysis was reported in following figure (Figure 27). All simulations are carried out using 64 CPU at the high performance computing center (SCoPE) of the Università degli Studi di Napoli "Federico II".

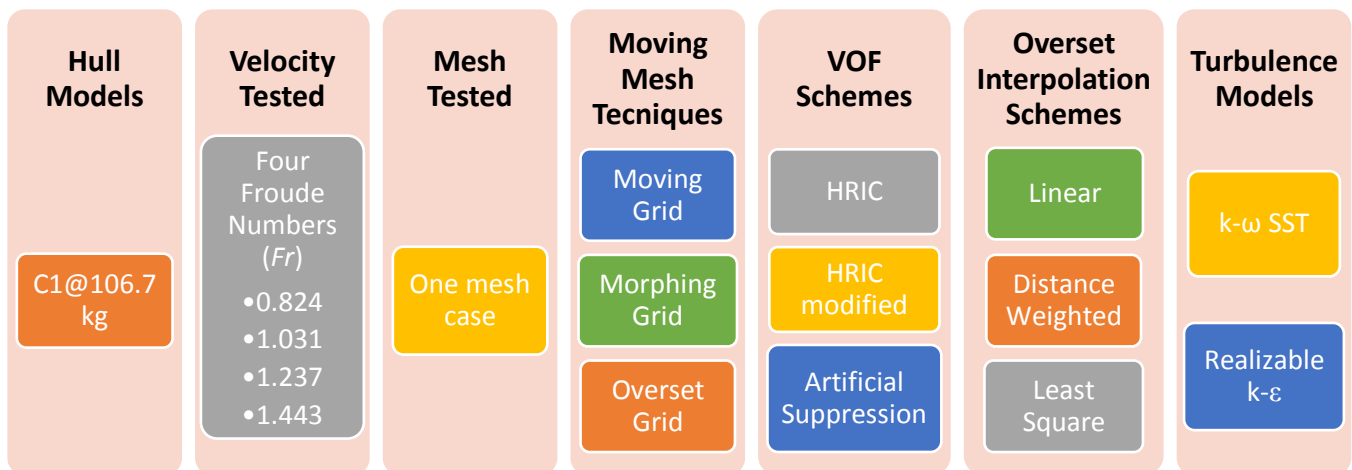


Figure 27 Summary of the tests for the modelling analysis

2. Response variables

The response variables, which are analyzed in the simulations, are resistance coefficients, dynamic wetted surface (S_w), and trim angle (τ). The resistance coefficients are the followings:

- Total resistance coefficient (C_T).
- Frictional resistance coefficient (C_F).

Evaluated using the formulae:

$$C_T = R_T / 0.5 \rho S_{ws} V^2 \quad (52)$$

$$C_F = R_F / 0.5 \rho S_{ws} V^2 \quad (53)$$

The C_T and C_F are evaluated using the static wetted surface (S_{ws}).

3. Moving meshes technique analysis

As mentioned in the Chapter 3 for an accurate evaluation of the planing hulls performance in resistance test simulation it is also necessary to evaluate the running attitude of the hull.

As stated in Chapter 5, the DFBI approach allows coupling the rigid body motion to the Navier Stokes equations. The rigid body motion can be simulated by means of the different techniques presented in the Chapter 5. The moving grid is the simplest and most widely used. However, the previously exposed drawbacks suggest the moving grid method to the least suitable for the simulations of resistance test of the planing hulls. For these reasons the alternative solutions to the simple moving grid are evaluated. The configurations tested are:

- Moving grid (MG).
- Morphing Grid (MHG).
- Overset Grid (OG)

For the overset mesh case two different mesh topologies are compared:

- Trimmed (structured mesh) for the background region – Trimmed (structured mesh) for the overset region (OG-TT);
- Trimmed (structured mesh) for the background region – Polyhedral (unstructured mesh) for the overset region (OG-TP).

The main characteristics of the different grids tested are reported in Table 6. All these techniques are compared in order to identify the best technique in terms of reduction of simulation modeling error (δ_{SM}) and in terms of computational effort.

Table 6 Grid base size dimension and total number of cells for the four different configurations of the grids that are tested

	Moving Grid (MG)	Morphing Grid (MHG)	Overset Grid (OG – TT)	Overset Grid (OG – TP)
Hull	0.047 L_{WL}	0.047 L_{WL}	0.375 L_{WL}	0.375 L_{WL}
Background	N. A.	N. A.	0.958 L_{WL}	0.958 L_{WL}
Number of cells	1855777	1855777	2173806	759046

The results of this analysis and the calculation time required by the different grids are shown below.

4. Computational domain and boundary condition

a. Moving Grid

As reported in Chapter 5, in the moving grid case the rigid body motion of the hull should be modelled by rigidly moving the grid with respect to the free surface. As mentioned above, this technique presents shortcomings when is used for the simulation of resistance test of the planing hull. However this technique was taking into account in particular for the simple use. The boundary conditions used and the domain dimensions are the same for the morphing mesh case, see Figure 28 and Figure 29.

In order to minimize the problems exposed in the previous chapter, the hull at the starting point has an initial trim angle of 2° aft and the damping function on the wave-surface at inlet, outlet and sides boundaries was used, as indicated in De Luca et al. [72].

b. Morphing grid

Differently from what happens for the overset grid method, the morphing grid method does not require additional settings. The dimensions of the calculation domains and the boundary conditions are illustrated respectively in Figure 28 and Figure 29. All the dimensions of the calculation domains are in compliance with the ITTC prescriptions [73].

In the simulation of the moving meshes, the morphing technique is combined with rigid motions, as mentioned above. Since morphing strategies can lead to poor quality cells, it is important to keep under control the topological deformations that can take place both on the surface mesh and into the volume cells, by means of specific mesh quality metrics.

In order to minimize the topological deformations of the grid domain, the hull at the starting point has an initial trim angle of 2° degree aft (as for moving grid case).

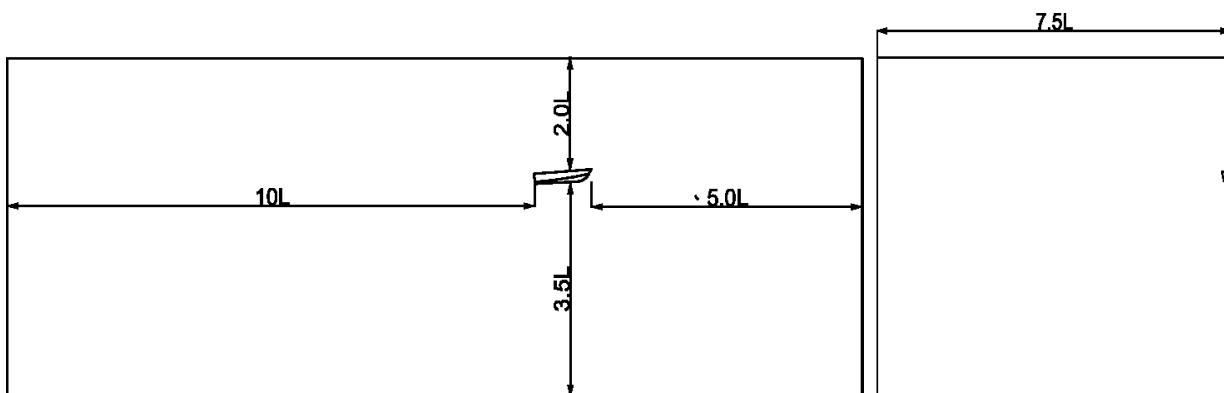


Figure 28 Morphing and moving grid case. Front (left) and side (right) view of the dimensions of the domain (L is waterline length of the ship)

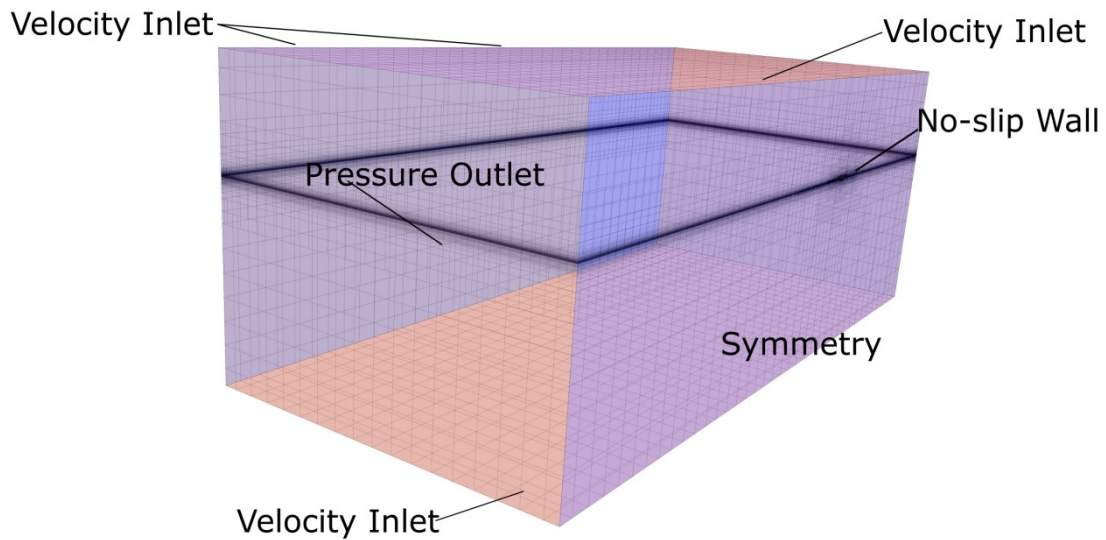


Figure 29 Boundary conditions for the morphing and moving grid cases

c. Overset/Chimera grid

As mentioned above, the overset mesh technique required two different regions, *i.e.*, the background and overset regions. In ship hydrodynamics applications, it is important to note that no defined recommendations in terms of domain dimensions are available for the overset region. The dimensions of the overset region gathered from experience.

Instead for the background region usually it is in compliance with the ITTC’s CFD recommendations [74]. Figure 30 shows the dimensions of all of the computational domains.

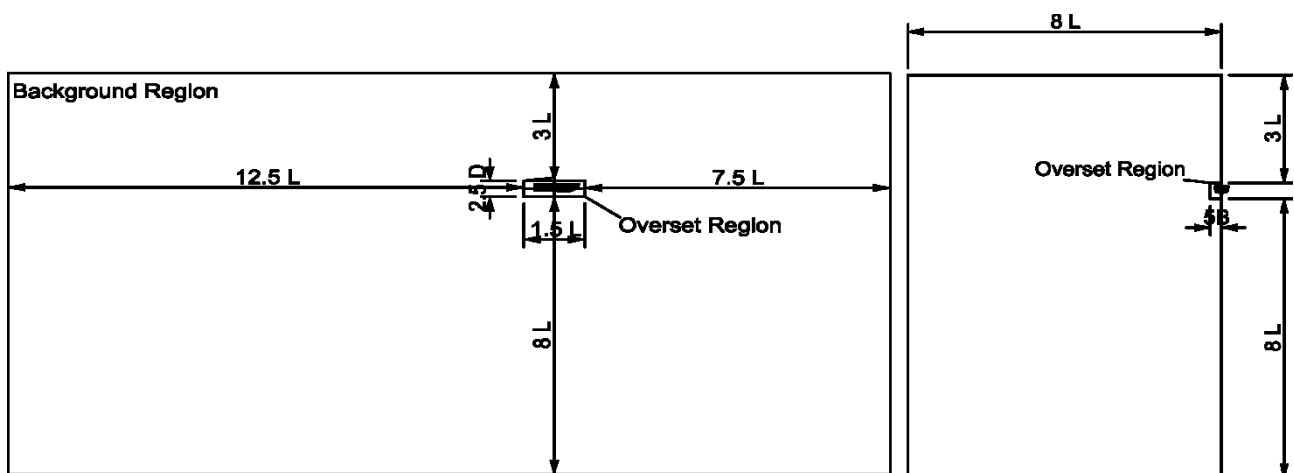


Figure 30 Overset grid: Front (left) and side (right) view of the dimensions of the domain (B : half beam of the ship, L : waterline length of the ship, D : height of the ship)

Figure 31 shows a general view of the computation domain and the notations of the selected boundary conditions. In order to reduce the computational effort, only half of the hull was modelled, so a symmetry

plane is located in the center line of the domain. The Figure 32 shows the different mesh topologies, structured and unstructured, used in the OG case.

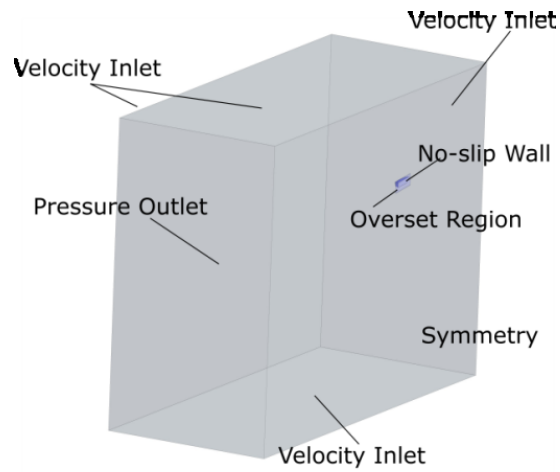


Figure 31 General view of OG Case of the two regions with the boundary conditions

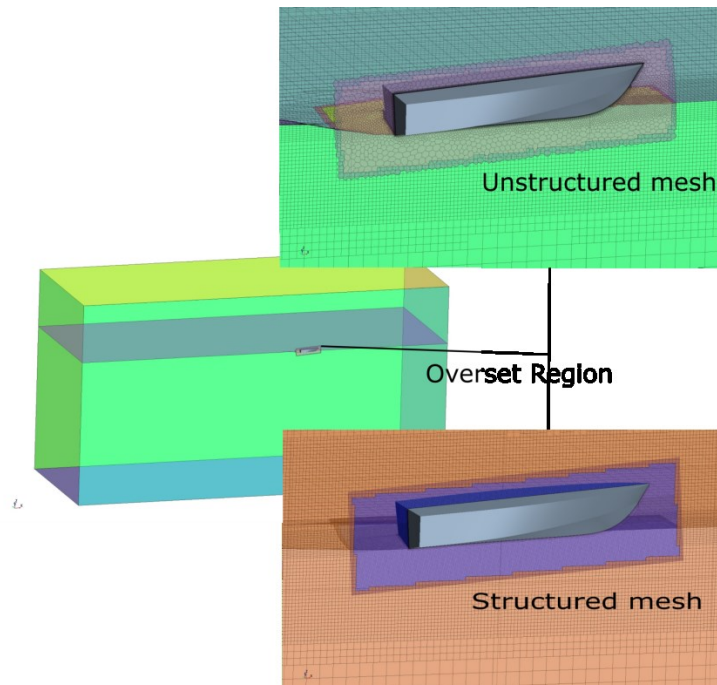


Figure 32 The background and overset regions with polyhedral (unstructured) mesh and trimmed (structured) mesh respectively.

5. A detail: the design of the grid refinement of air-water interface

In the preliminary stage, it is important to identify a suitable height for the grid refinement of the air-water interface. An assessment of the height of air-water interface (H) was made using equation 54, delivered by Savitsky and Morabito [75] for a different use: the evaluation of centerline profile of surface wave contours associated with the forebody wake of the stepped hulls.

Nevertheless the equation 54 is suitable for an estimation of stern wake height at the centerline for a planing hull, as shown in Figure 33 ($H = H_1$).

$$H_1 = 0.17(K + 0.03L_K \tau^{1.5}) \sin \left[\frac{\pi}{C_V} \left(\frac{x}{3} \right)^{1.5} \right] \quad (54)$$

Where $K = 1.5$ for $\beta = 10^\circ$, and $K = 2.0$ for $\beta = 20^\circ$ and 30° , H_1 is the surface height, C_V is the speed coefficient (equal to Fr_V) and x is the distance aft of transom.

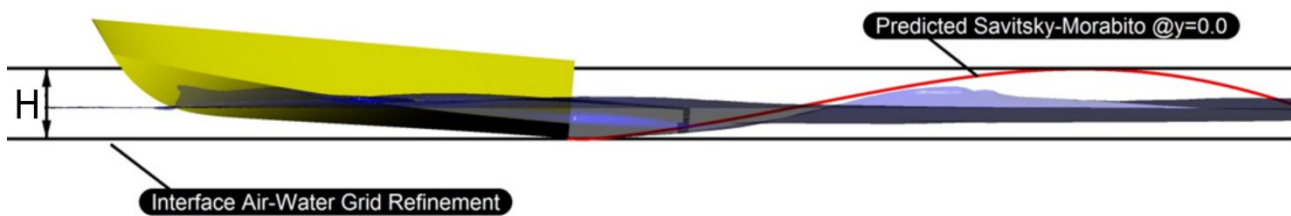


Figure 33 Comparison of CFD free surface elevation and centerline free surface profile evaluated according to Savitsky and Morabito [75]

As illustrated above, the equation 54 is useful to define in a preliminary stage the height of the refinement zone for the free-surface, in order to avoid that during the simulation the grid refinement does not follow the free surface. This allows evaluating adequately the wave height generated from the planing hull.

This analysis to be more effective must be performed for the most critical speed, namely the one that determines the greatest variation of trim, according to the speed range of validity of the equation 54 indicated by Savitsky and Morabito [75].

6. Physics modeling, time-step and coordinate system

To solve the time-marching equations, the implicit solver is used to find the field of all hydrodynamic unknown quantities. The implicit solver is used in conjunction with an iterative solver to solve each time step. The velocity–pressure coupling and overall solution procedure was based on the SIMPLE method to conjugate the pressure field and the velocity field. The discretized algebraic equations are solved by using a point-wise Gauss-Seidel iterative algorithm, and the Algebraic Multi-Grid (AMG) method was used to accelerate the convergence of the solution. As suggested previously, the free surface was modelled with the VOF technique. A segregated flow solver was used for all of the simulations.

The calculations are performed by the commercially CFD code CD-Adapco STAR-CCM+.

The DFBI model was used with the aim of simulating the planing craft's behavior with the hull free to move in the pitch and heave directions. As mentioned in the previous Chapter, the DFBI model allowed the RANS solver to evaluate the force and moments on the hull and to solve the governing equations of the rigid body motion in order to relocate the rigid body.

The coordinate system for all simulations is imposed in the same position of the reference frame system of the towing tank acquisition system; the coordinates were shown in Table 2

The time-step used in the simulations is a function of the speed of the hull, according to the following ITTC equation [74]:

$$\Delta t = 0.01/0.005 \frac{l}{V} \quad (55)$$

Where V is the speed of the hull and l is a characteristic length value. In these simulations l is assumed to be equal to L_k . Furthermore the time-step is a function of the grid density in order to keep the CFL number constant.

Two different turbulence models (Realizable k - ϵ and k - ω SST) are used to turbulence closure of the RANS equations. These models are the most wide used turbulence models for ship hydrodynamics applications.

The wall function was used for the near wall treatment. The all wall y^+ wall treatment is used for all of the simulations. It is a hybrid approach that attempts to emulate the high y^+ wall treatment for coarse meshes (for $y^+ > 30$), and the low y^+ wall treatment for fine meshes (for $y^+ \approx 1$). It also formulated with the desirable characteristic of producing reasonable answers for meshes of intermediate resolution (for y^+ in the buffer layer), [54]. This approach is considered to be a reasonable compromise between the describing the boundary layer with acceptable quality and the time required for the calculation.

In the next section more details are provided about the values of wall y^+ on the hull that are reported in Table 13 and shown in Figure 44. All of the properties of the numerical solver are summarized in Table 7.

Table 7 Summary of the numerical simulation setup

Pressure link	Pressure	Convection Term	Temporal Discretization	Time-step (s)	Iteration per time-step	Turbulence Model	Overset Interpolation Scheme
SIMPLE	Standard	2 nd Order	1 st Order	Function of velocity and grid	5	Realizable k- ϵ - k- ω SST	Linear

7. Results of moving meshes technique analysis

The results of the modeling analysis and the calculation time required by the different grids are reported below. As shown in Figure 35, all computational results coincide well with the experimental data. For all the grids that are tested, the percentage error between the EFD and the CFD data is lower for the total resistance coefficient than for the other response variables. For C_T and τ the trend of percentage error increased with the Fr , different trend was observed for C_F and S_W that have a minimum for $Fr = 1.031$ and 1.237 .

Figure 34 shows that the OG-TP mesh case is the less onerous in terms of the computational time required. The OG-TP case appears to be the best solution since it allows obtaining sufficiently accurate results with the lower calculation times due to the smaller number of cells.

However the morphing grid technique presents accurate results, in particular in the evaluation of C_T and τ , but this technique was discarded due to the very high computational effort (Figure 34).

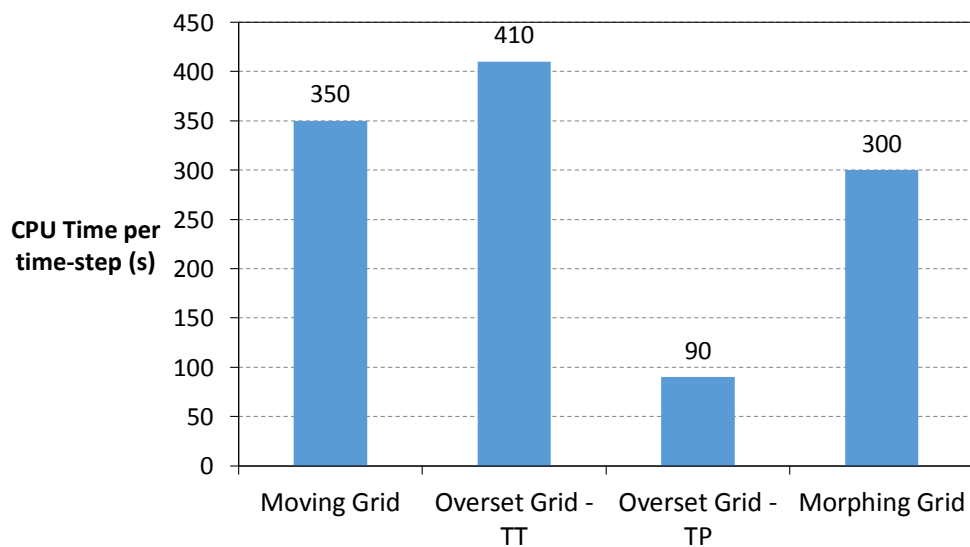


Figure 34 Calculation time required for the different moving mesh techniques

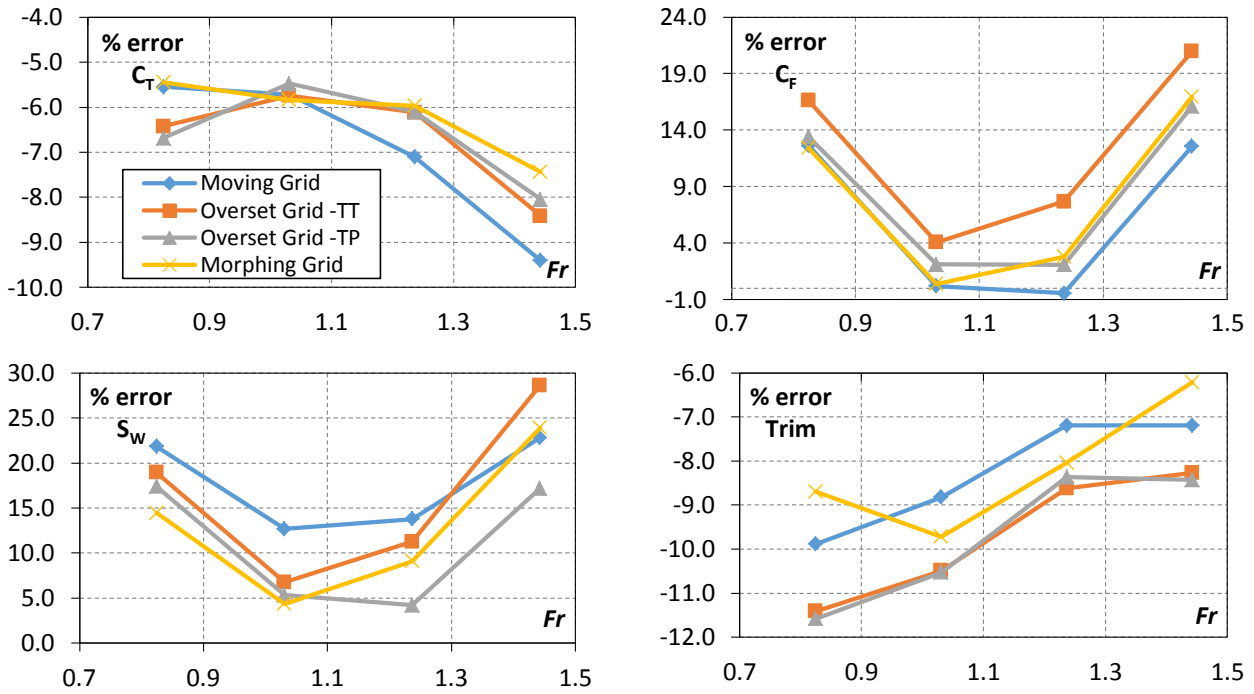


Figure 35 Percentage comparison errors between CFD simulation and EFD for the different configurations that are tested

Table 8 Results of simulations with different moving mesh solutions

Total Resistance Coefficient					
<i>Fr</i>	<i>MG</i>	<i>OG-TT</i>	<i>OG-TP</i>	<i>MGH</i>	<i>Exp.</i>
	*10 ³				
0.824	12.56	12.45	12.41	12.58	13.30
1.031	9.80	9.79	9.82	9.78	10.39
1.237	7.71	7.80	7.80	7.81	8.30
1.443	6.89	6.96	6.99	7.04	7.60

Frictional Resistance Coefficient					
<i>Fr</i>	<i>MG</i>	<i>OG-TT</i>	<i>OG-TP</i>	<i>MGH</i>	<i>Exp.</i>
	*10 ³				
0.824	3.38	3.50	3.40	3.37	3.00
1.031	2.92	3.04	2.98	2.93	2.92
1.237	2.83	3.06	2.90	2.92	2.85
1.443	3.11	3.35	3.21	3.23	2.77

Trim					
<i>Fr</i>	<i>MG</i>	<i>OG-TT</i>	<i>OG-TP</i>	<i>MGH</i>	<i>Exp.</i>
	(deg)	(deg)	(deg)	(deg)	(deg)
0.824	4.00	3.93	3.93	4.05	4.44
1.031	4.98	4.89	4.89	4.93	5.46
1.237	4.58	4.51	4.52	4.54	4.94
1.443	3.99	3.94	3.93	4.03	4.30

Wetted Surface					
<i>Fr</i>	<i>MG</i>	<i>OG-TT</i>	<i>OG-TP</i>	<i>MGH</i>	<i>Exp.</i>
	(m ²)				
0.824	1.68	1.64	1.62	1.58	1.38
1.031	1.48	1.40	1.38	1.37	1.31
1.237	1.35	1.32	1.24	1.29	1.19
1.443	1.25	1.31	1.19	1.26	1.02

a. Interpolation schemes

As stated in the previous chapter, in order to choose a proper setup to simulate the planing hull particular attention is direct to the interpolation schemes (required with the overset mesh technique). The overset grid approach must establish connectivity between the background and the overset regions, so an assembly process must take place through an interpolation scheme. As reported in CD-Adapco User’s Guide [54], the interpolation schemes options are:

1. Distance-weighted
2. Least squares
3. Linear.

Figure 36 shows the results of the simulations performed with the different interpolation schemes for the OG-TP grid configuration. The Figure 36 shows that the best solution for the interpolation scheme is the linear interpolation.

As matter of fact, the linear interpolation is very suitable for basically stationary phenomena, in which there is little variation of the moving grid respect to the background mesh. According to CD Adapco User’s Guide [54], the linear interpolation schemes are more accurate, but they are also the most expensive scheme in terms of calculation effort, as shown in Figure 37.

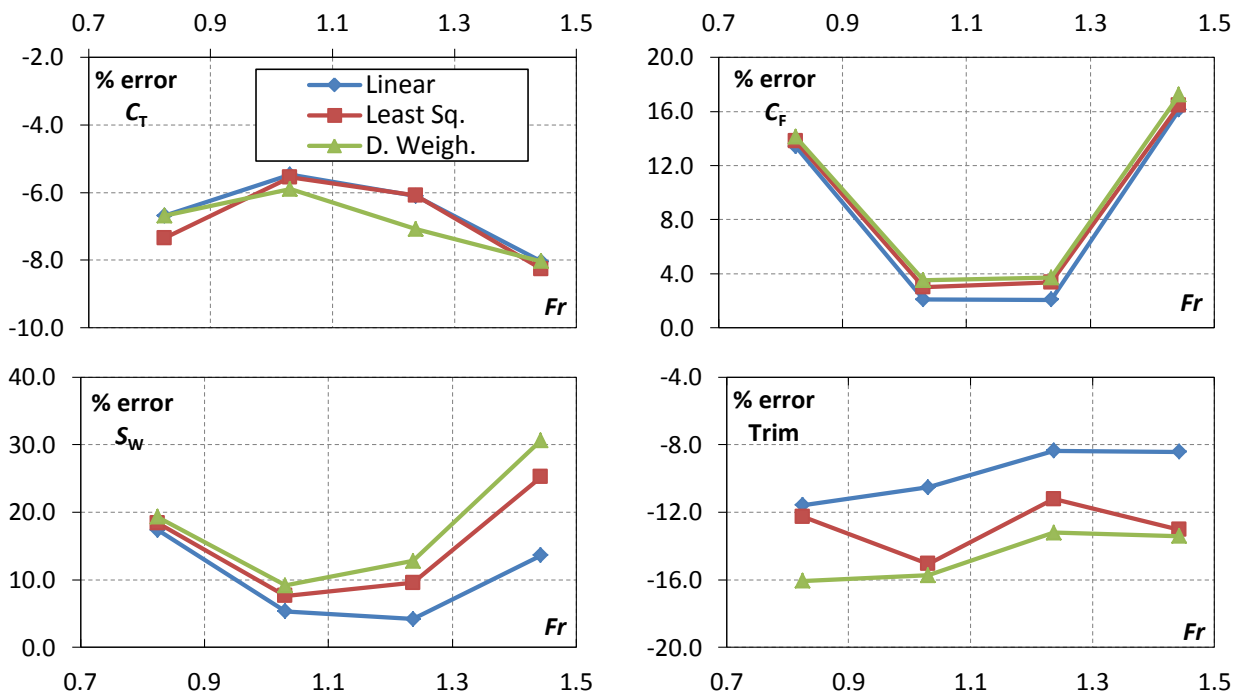


Figure 36 Percentage comparison errors between CFD simulation and EFD for the different overset interpolation schemes that are analyzed

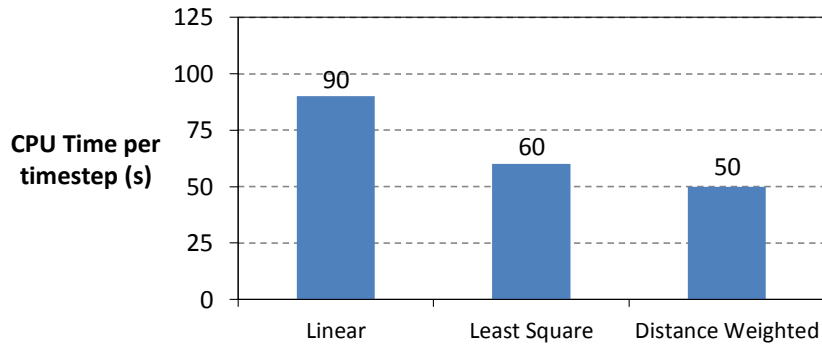


Figure 37 Calculation time required for the different interpolation schemes

Table 9 Results of OG-TP simulations with different interpolation schemes

<i>Total Resistance Coefficient</i>					<i>Frictional Resistance Coefficient</i>				
<i>Fr</i>	<i>Linear</i>	<i>Least Square</i>	<i>Distance Weighted</i>	<i>Exp.</i>	<i>Fr</i>	<i>Linear</i>	<i>Least Square</i>	<i>Distance Weighted</i>	<i>Exp.</i>
	*10 ³	*10 ³	*10 ³	*10 ³		*10 ³	*10 ³	*10 ³	*10 ³
0.824	12.41	12.32	12.41	13.30	0.824	3.40	3.41	3.42	3.00
1.031	9.82	9.81	9.78	10.39	1.031	2.98	3.00	3.02	2.92
1.237	7.80	7.80	7.72	8.30	1.237	2.90	2.94	2.95	2.84
1.443	6.99	6.97	6.99	7.60	1.443	3.21	3.22	3.24	2.77

<i>Wetted Surface</i>					<i>Trim angle</i>				
<i>Fr</i>	<i>Linear</i>	<i>Least Square</i>	<i>Distance Weighted</i>	<i>Exp.</i>	<i>Fr</i>	<i>Linear</i>	<i>Least Square</i>	<i>Distance Weighted</i>	<i>Exp.</i>
	(m ²)	(m ²)	(m ²)	(m ²)		(deg)	(deg)	(deg)	(deg)
0.824	1.62	1.64	1.65	1.38	0.824	3.93	3.89	3.73	4.44
1.031	1.38	1.41	1.43	1.31	1.031	4.89	4.64	4.60	5.46
1.237	1.23	1.30	1.34	1.19	1.237	4.52	4.38	4.28	4.93
1.443	1.15	1.27	1.33	1.02	1.443	3.94	3.74	3.72	4.29

b. VOF Schemes

As mentioned in the Chapter 5, regarding the interface capturing methods the software CD-Adapco STAR CCM+ uses the well-known VOF approach with a HRIC scheme based on the CICSAM scheme.

The standard configuration of the HRIC scheme can be modified depending on the local CFL. This modification blends the HRIC scheme and the UD scheme depending on local value of CFL_U and CFL_L.

As indicated by various authors (Andrillon and Alessandrini [60], and Ferziger and Peric [61]) the local CFL dependency scheme could be the main cause of the NV problem.

The NV problem is one of the sources of the modeling error, in particular for the planing hull simulation. The Figure 39 (c) shows the artificial mixing of the air into the water on the hull bottom, typical of the NV problem. In order to reduce the NV problem two ways are investigated:

- The first strategy takes into account the physical aspect of the resistance test. The simulation of resistance test, mimicking the towing tank procedures, seeks a steady state solution, so the robustness of the calculation is not a problem. For this reason is possible to modify the HRIC standard schemes by removing the local CFL dependency scheme, Figure 39 (b). A detailed analysis of these aspects is reported by Bohm [57].
- The second strategy is the artificial suppression of numerical diffusion, as in Viola et al. [63]. An analytical field function is defined to select only the cells that are affected by the NV problem on the bottom of the hull and to remove a percentage of the air mass from the selected cells, Figure 39 (a).

The artificial suppression, Figure 39 (a), worked well with respect to the other schemes, and it totally avoided the NV problem. However, it must be noted that this method could introduce errors in the conservation properties of mass and momentum.

The results of the three configurations of convection schemes showed that there are appreciable differences in the estimation of C_F , S_w , and τ . For the first two response variables, the artificial suppression method determined an over prediction of as much as 2.5 %, but dynamic trim is underestimated by as much as 1.5 %. This is mainly due to the total elimination of the NV problem.

No significant differences in terms of calculation time are detected among the three schemes.

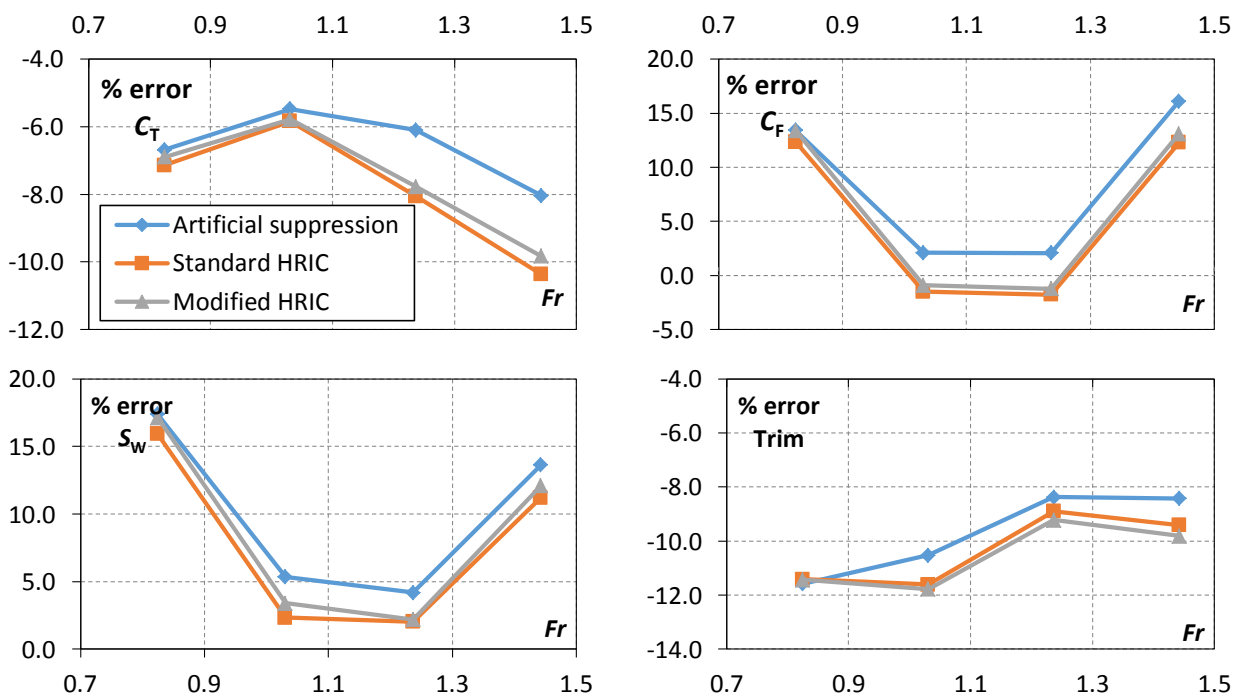


Figure 38 Percentage comparison errors between CFD simulation and EFD for the different overset interpolation schemes that are analysed (C1 model)

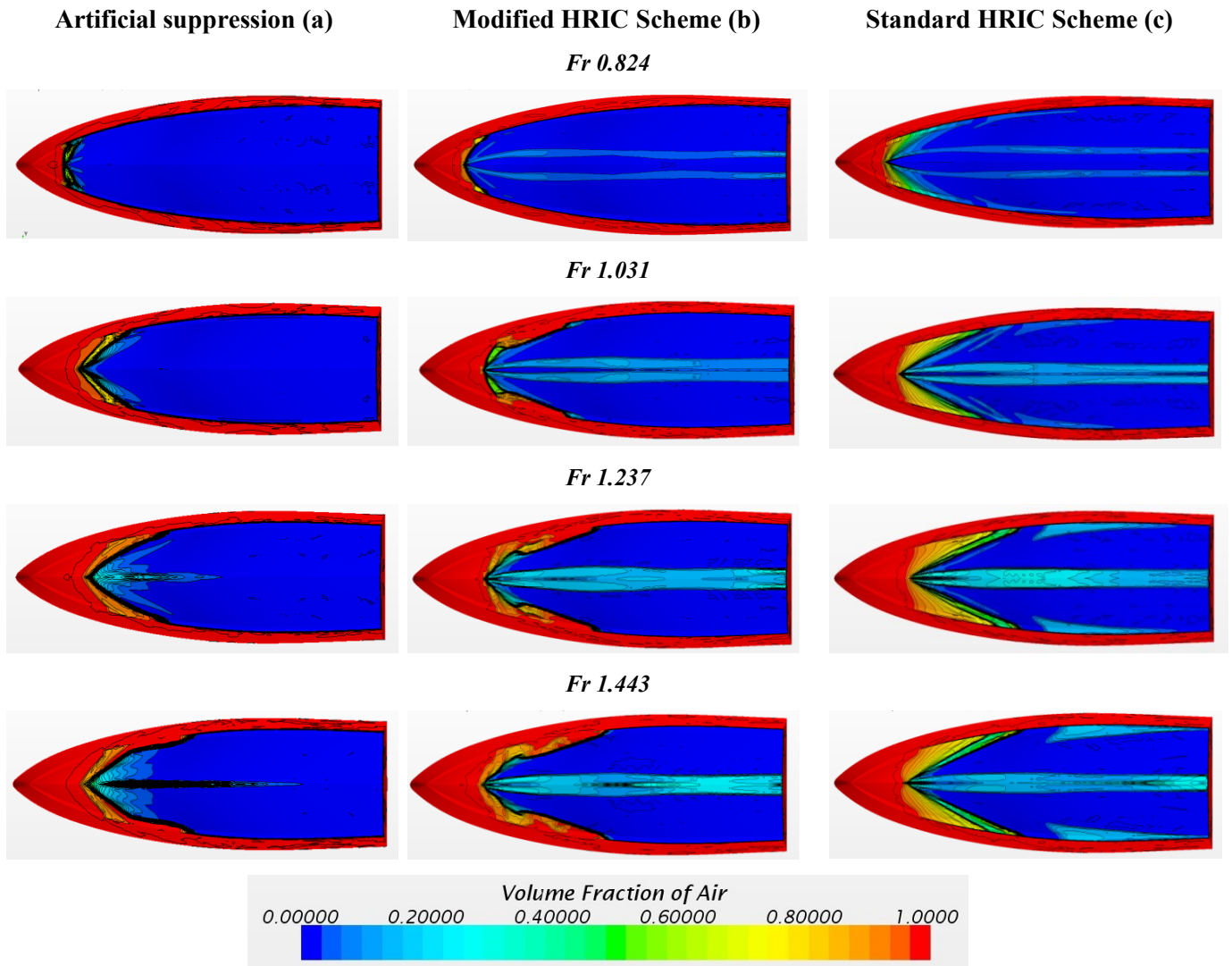


Figure 39 Representation of the VOF on the bottom hull of the C1 model for the different VOF schemes examined for the OG-TP grid case: (a) HRIC scheme with artificial suppression of air mass fraction, (b) HRIC scheme without dependence on the local CFL number, (c) HRIC scheme with dependence on the local CFL number

Table 10 Results of OG-TP simulations with different VOF schemes

Total Resistance Coefficient					Frictional Resistance Coefficient				
<i>Fr</i>	<i>Artificial suppression</i>	<i>Standard HRIC</i>	<i>Modified HRIC</i>	<i>Exp.</i>	<i>Fr</i>	<i>Artificial suppression</i>	<i>Standard HRIC</i>	<i>Modified HRIC</i>	<i>Exp.</i>
	$\cdot 10^3$	$\cdot 10^3$	$\cdot 10^3$	$\cdot 10^3$		$\cdot 10^3$	$\cdot 10^3$	$\cdot 10^3$	$\cdot 10^3$
0.824	12.41	12.35	12.38	13.30	0.824	3.40	3.37	3.40	3.00
1.031	9.82	9.78	9.79	10.39	1.031	2.98	2.87	2.89	2.92
1.237	7.80	7.64	7.66	8.30	1.237	2.90	2.79	2.81	2.85
1.443	6.99	6.81	6.85	7.60	1.443	3.21	3.11	3.13	2.77

<i>Trim</i>				
<i>Fr</i>	<i>Artificial suppression</i>	<i>Standard HRIC</i>	<i>Modified HRIC</i>	<i>Exp.</i>
	(deg)	(deg)	(deg)	(deg)
0.824	3.93	3.93	3.93	4.44
1.031	4.89	4.83	4.82	5.46
1.237	4.52	4.50	4.48	4.94
1.443	3.93	3.89	3.87	4.30

<i>Wetted Surface</i>				
<i>Fr</i>	<i>Artificial suppression</i>	<i>Standard HRIC</i>	<i>Modified HRIC</i>	<i>Exp.</i>
	(m ²)	(m ²)	(m ²)	(m ²)
0.824	1.62	1.60	1.62	1.38
1.031	1.38	1.34	1.35	1.31
1.237	1.24	1.21	1.21	1.19
1.443	1.15	1.13	1.14	1.02

c. Turbulence Model Analysis

In order to determine the suitable turbulence model for planing hull simulation, the comparison is conducted between the most widely used turbulence models: the Realizable k-ε and the k-ω SST. This comparison is performed for all response variables analyzed for the C1 model.

The percentage errors between the results calculated with the two turbulence models was reported in Figure 40.

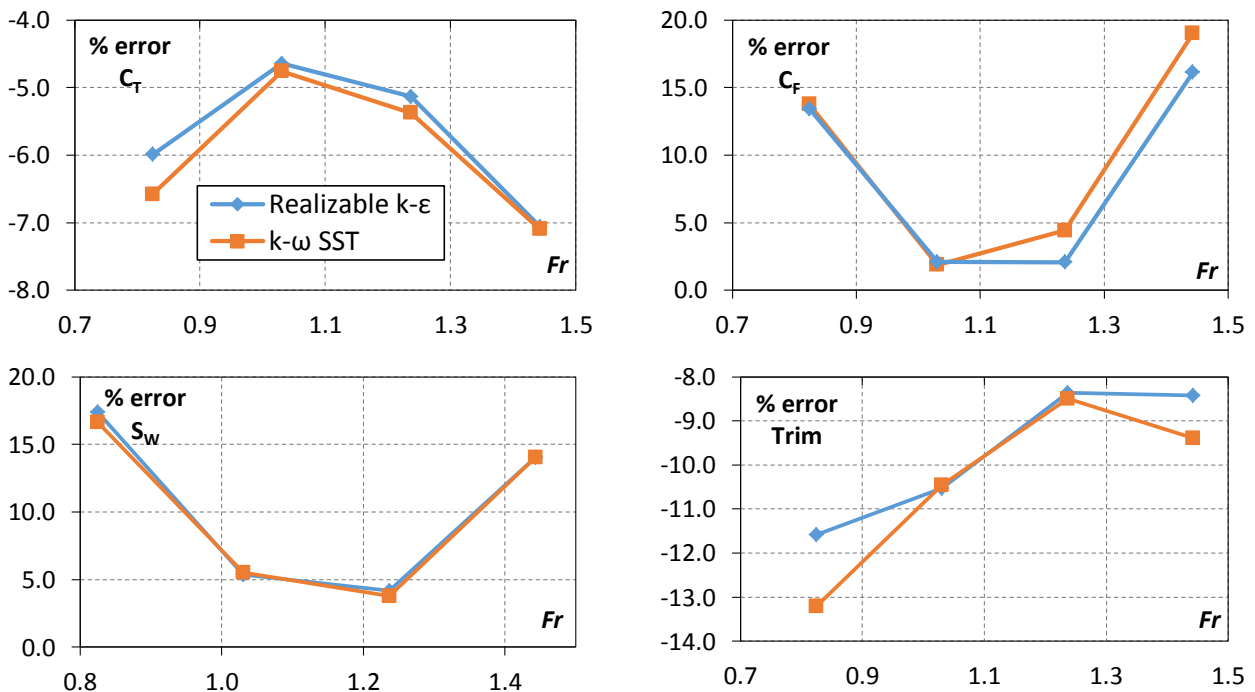


Figure 40 Percentage comparison errors between CFD simulation and EFD data for the two different turbulence models

As shown in Figure 40, no appreciable differences were detected among the most used two-equations turbulence models in ship hydrodynamics. This conclusion is consistent with the report of ITTC specialist committee on CFD in marine hydrodynamics [6], the standard turbulence models has a little effect on the prediction accuracy as far as in particular the resistance coefficients and wetted surface.

8. Summary of modeling analysis results

The results of modeling analysis show that the OG technique is the best solution for the planing craft simulation in terms of accuracy and computational effort, in particular the configuration with coupled structured mesh (background region) and polyhedral mesh (overset region).

However the morphing grid technique provides more accurate results than OG case but with a higher computational effort. For this reason the numerical analysis is performed using the OG configuration. The OG-TP results showed a well agreement with the experimental data, with a percentage error between the EFD and the CFD data lower than 8.0% for the total resistance coefficient and 11.6% for the dynamic trim angle.

The OG case implied an interpolation scheme and the comparison of the different interpolation schemes available showed that the linear interpolation is the best solution.

The NV problem is reduced/avoided using the artificial suppression scheme of the artificial mixing of air and water.

About the turbulence models, the analysis performed confirmed that no appreciable differences between Realizable $k-\epsilon$ and $k-\omega$ SST are detected, as indicated in ITTC specialist committee on CFD in marine hydrodynamics [6].

In summary the setup chosen is the following:

- OG-TP case - structured mesh (background region) and unstructured mesh (overset region).
- Linear interpolation scheme.
- Artificial suppression scheme for avoid the NV problem.
- Turbulence model: Realizable $k-\epsilon$.

7

NUMERICAL ANALYSIS

In this section are reported the main results of the verification and validation study for the three models of SSN using the simulation setup evaluated through the modeling analysis.

1. Introduction

The verification study is conducted in order to assess the simulation numerical uncertainty, U_{SN} , which is composed mainly of the iterative uncertainty, U_I ; the time-step uncertainty, U_{TS} ; the grid uncertainty, U_G , and the statistical error, U_{ST} . The U_G and U_{ST} is calculated for all of the models that are tested, but U_{TS} and U_I are evaluated only for the C1 model and these values are extended to the other models.

The verification study is conducted for the response variables, *i.e.*, C_T , C_F , τ and S_W at four velocities, *i.e.*, $Fr = 0.824, 1.031, 1.237, 1.443$. All simulations are performed using the OG-TP mesh case and the planning of the simulations is reported in Figure 41.

The validation of the solution is assessed by comparing U_V and E , as indicated in equations 33 and 34.

The V&V study is performed according to the methodology and procedures prescribed by ITTC's guidelines [21] and the recent improvements reported in Xing and Stern [27] and Eça and Hoekstra [29].

All simulations are performed using 64 CPU at the high performance computing center (SCoPE) of the Università degli Studi di Napoli "Federico II".

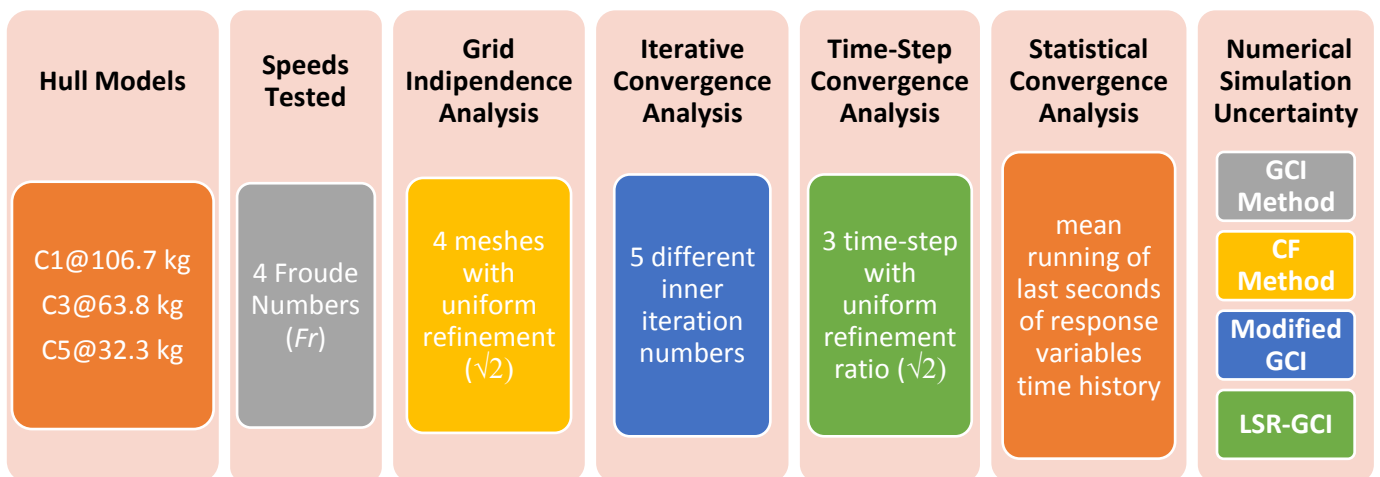


Figure 41 Summary of the tests for the numerical analysis

2. Iterative convergence analysis

The inner iterations for each time step enable the iterative convergence at each time step, so, at the end of last iteration, the simulation can advance to the next time step. Iterative convergence analysis is assessed through graphical approach, as reported in Stern et al. [9]. This analysis is performed only for the C1 model.

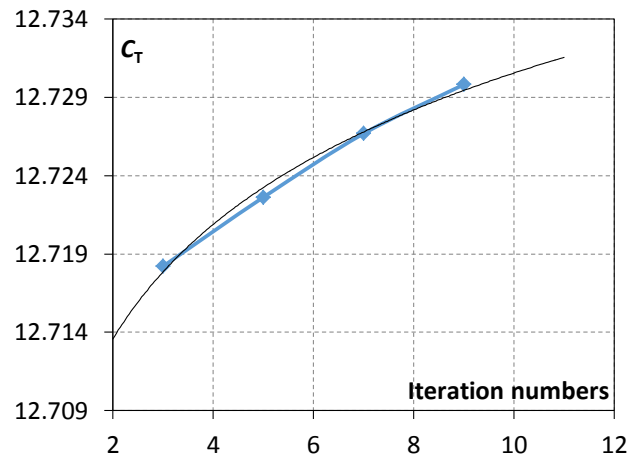


Figure 42 Example of graphical assessment of iterative convergence analysis for C_T

Table 11 shows the iterative uncertainty of the response variables. The results indicated that the change of C_T and C_F is less than 1 % as the number of iterations increased from 3 to 9. However, the dynamic trim angle and the wetted surface had a different trend in that they are far more sensitive to the variation of the number of iterations, as reported in Table 11.

Table 11 Iterative convergence study for the C1 model and one grid case at different Fr values
(The U_I values are a percentage of the solution with 9 inner iterations)

	C_T	C_F	<i>Trim</i>	S_w
<i>Fr</i>	U_I	U_I	U_I	U_I
	(%)	(%)	(%)	(%)
0.824	0.37	0.24	0.18	0.94
1.031	0.79	1.33	2.95	1.30
1.237	0.66	0.21	1.16	1.81
1.443	0.65	0.91	0.60	0.91

The U_I values have the same order of magnitude for all Fr values, with the exception of $Fr = 1.031$, which is a critical motion condition (pre-planing condition). This suggests that there may be a conditioning of the flow regime in the U_I values, beyond the iterative schemes that are applied. Moreover, as indicated in Xing et al. [76], the U_I is not mainly influenced by the resolution of the grid.

3. Time-step convergence analysis

Referring to the time-step convergence study, this analysis provided for the C1 model by decreasing gradually the value of the time step by the $\sqrt{2}$ ratio, *i.e.* 0.0199 s, 0.0146 s, and 0.0100 s. The U_{TS} is obtained using the four methods, *i.e.*, GCI, CF, modified GCI [20], and GCI-LSR [21].

The C_T , C_F , S_W , and trim angle converged monotonically in every cases except for the trim angle at $Fr=1.031$, at which diverged in an oscillatory fashion.

All the results of this study are shown in Appendix A. In Figure 43 the U_{TS} values, as percentage of the finest solution, are shown for the examined response variables.

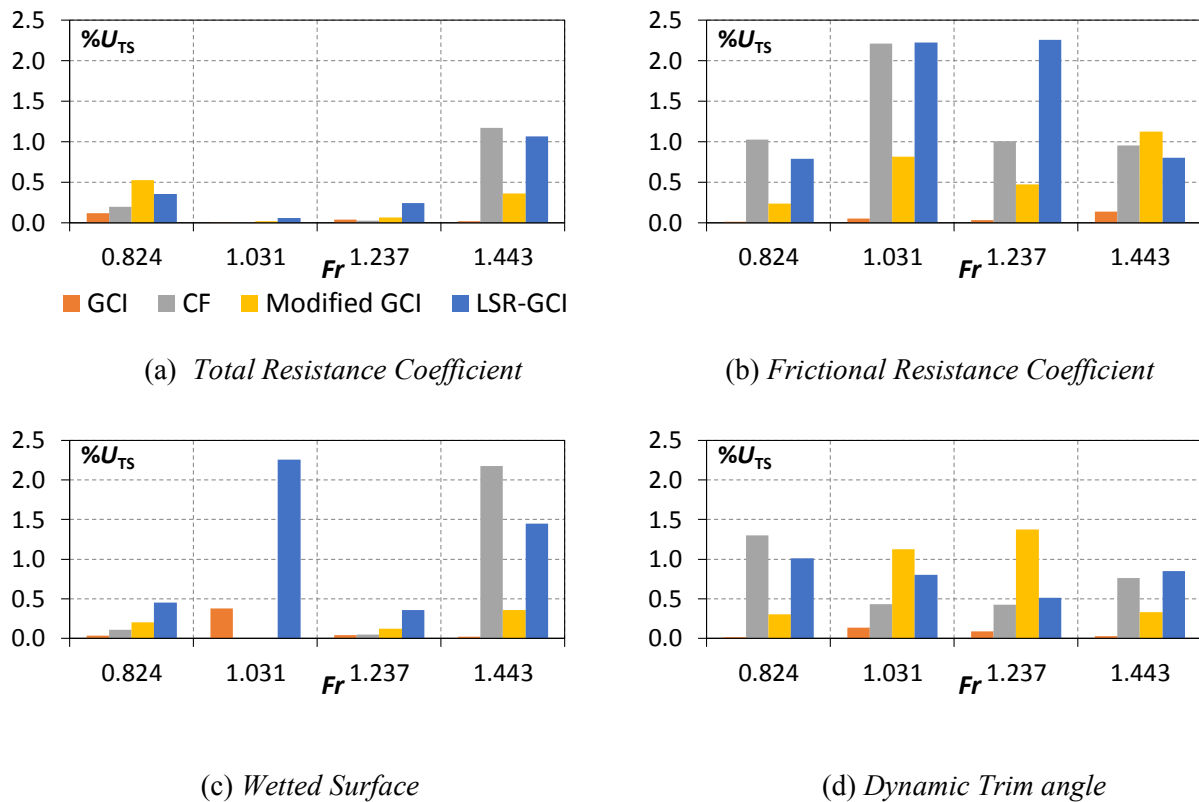


Figure 43 Time-step uncertainty for the different response variables on the C1 model

In all of the cases and for all of the response variables, the values of the U_{TS} percentage are less than 2.3 %. The GCI-LSR method provided uncertainty estimation similar to the CF method and is an order of magnitude greater than those provided by the GCI method. The modified GCI provided values of uncertainty intermediate between GCI and LSR-GCI method.

When the GCI-LSR method is used, U_{TS} was estimated using $p_{TS} = 2$ when $p_{TS} > 2$. This is the reason of the higher values of time-step uncertainty for the LSR-GCI than the other methods, in fact the p_{TS} is in the most cases higher the theoretical order of accuracy ($p_{th} = 2$) and, as indicated in Chapter 2, this is the cause of the underestimation of the uncertainty by the GCI, CF and modified GCI methods. As said, the LSR-GCI method is considered the most reliable method for the U_{TS} estimation.

4. Grid independence analysis

The assessment of grid uncertainty, when the monotonic convergence is reached, is performed using the above mentioned four methods. The four grids, as shown in Table 12, are generated with $r_k = \sqrt{2}$, which is applied to both the overset and background regions.

Table 12 Base size and total number of cells of the grids that were examined

	Cells	Base Size Background	Base Size Overset
Grid D	759046	0.958 L_{WL}	0.375 L_{WL}
Grid A	1073453	0.916 L_{WL}	0.333 L_{WL}
Grid C	1518092	0.875 L_{WL}	0.291 L_{WL}
Grid B	2146900	0.833 L_{WL}	0.250 L_{WL}

The resolution of the mesh near-wall is changed using the uniform refinement ratio. Hence different values of wall y^+ were obtained for the grids that are tested. Table 13 gives the average values of wall y^+ that are observed on the hull for the four velocities and the three models tested.

Figure 44 shows the wall y^+ range for the three models that were tested at maximum speed and for the coarsest and finest grids used. These settings of the near-wall mesh resulted in the y^+ values on the hull in the range of 30 to 130. This is the recommended range on the wall function application for the high y^+ wall treatment model [54].

Table 13 Average values of wall y^+ on the hull for the coarsest and finest grids

Fr	C1		C3		C5	
	Grid D	Grid B	Grid D	Grid B	Grid D	Grid B
	Avg. y^+					
0.824	25.1	25.0	45.9	40.8	25.7	25.0
1.031	28.0	26.3	54.0	48.9	32.9	30.4
1.236	32.8	30.1	62.0	55.3	35.1	35.3
1.442	36.8	34.2	70.0	62.7	40.1	38.3

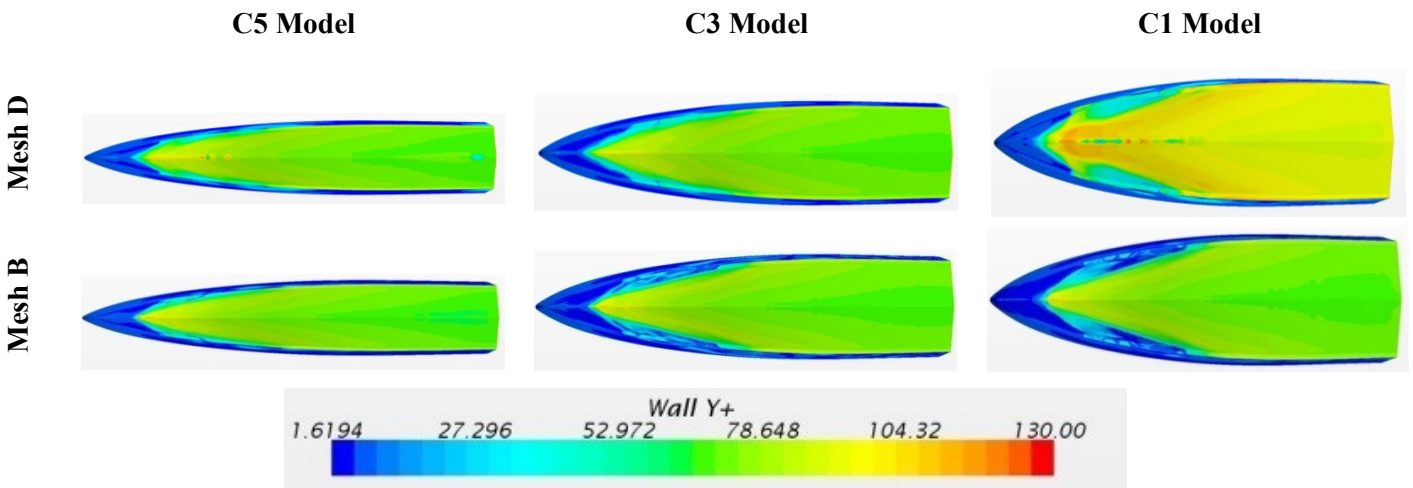


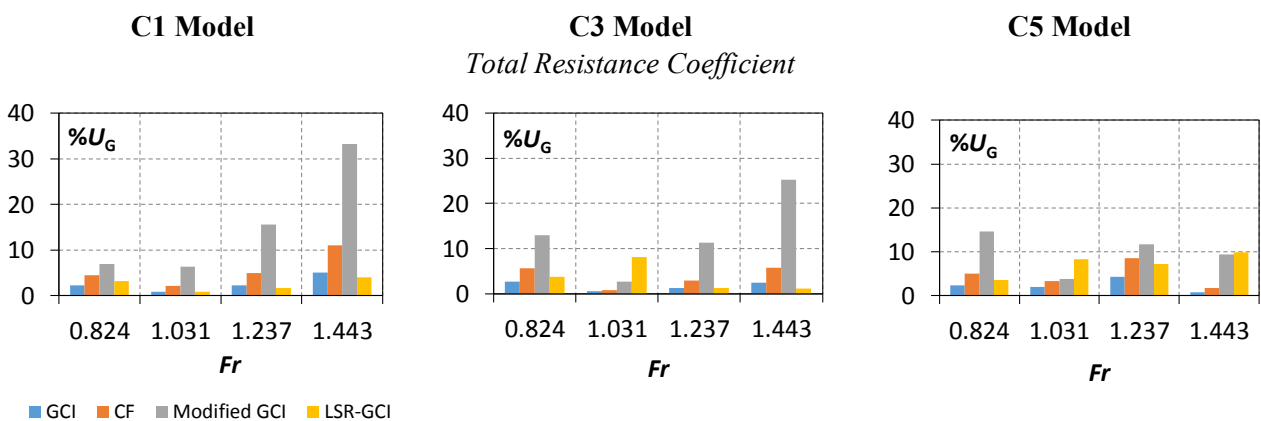
Figure 44 Ranges of wall y^+ values for the models at $Fr = 1.442$ at on grid cases D and B: (a) C5 model, (b) C3 model, and (c) C1 model

The results of the simulations in terms of comparison error related to the mesh density are reported in Appendix D and, observing the graphs in Appendix D, it should be noted that, in general for all response variables, increasing the cells number reduces the comparison error.

Using the four grids (D, A, C, and B), two different convergence studies are performed, *i.e.*, the D-A-C and the A-C-B cases. All results of the grid independence analysis for the three models tested at four speeds are shown extensively in the tables reported in Appendix B, and in Figure 45.

The tables in Appendix B show the R_G , the p_G estimated by ITTC and LSR approaches, the $1 - C_G$ values and the U_G delivered by the four different methods used to estimate the grid uncertainty.

The Figure 45 shows the values of the grid uncertainty for the different models and for the different response variables. These are the mean values of the U_G estimated for the D-A-C and A-C-B grid studies by the GCI, CF, and GCI modified methods. Using the LSR-GCI method only one value was obtained for the four grids used.



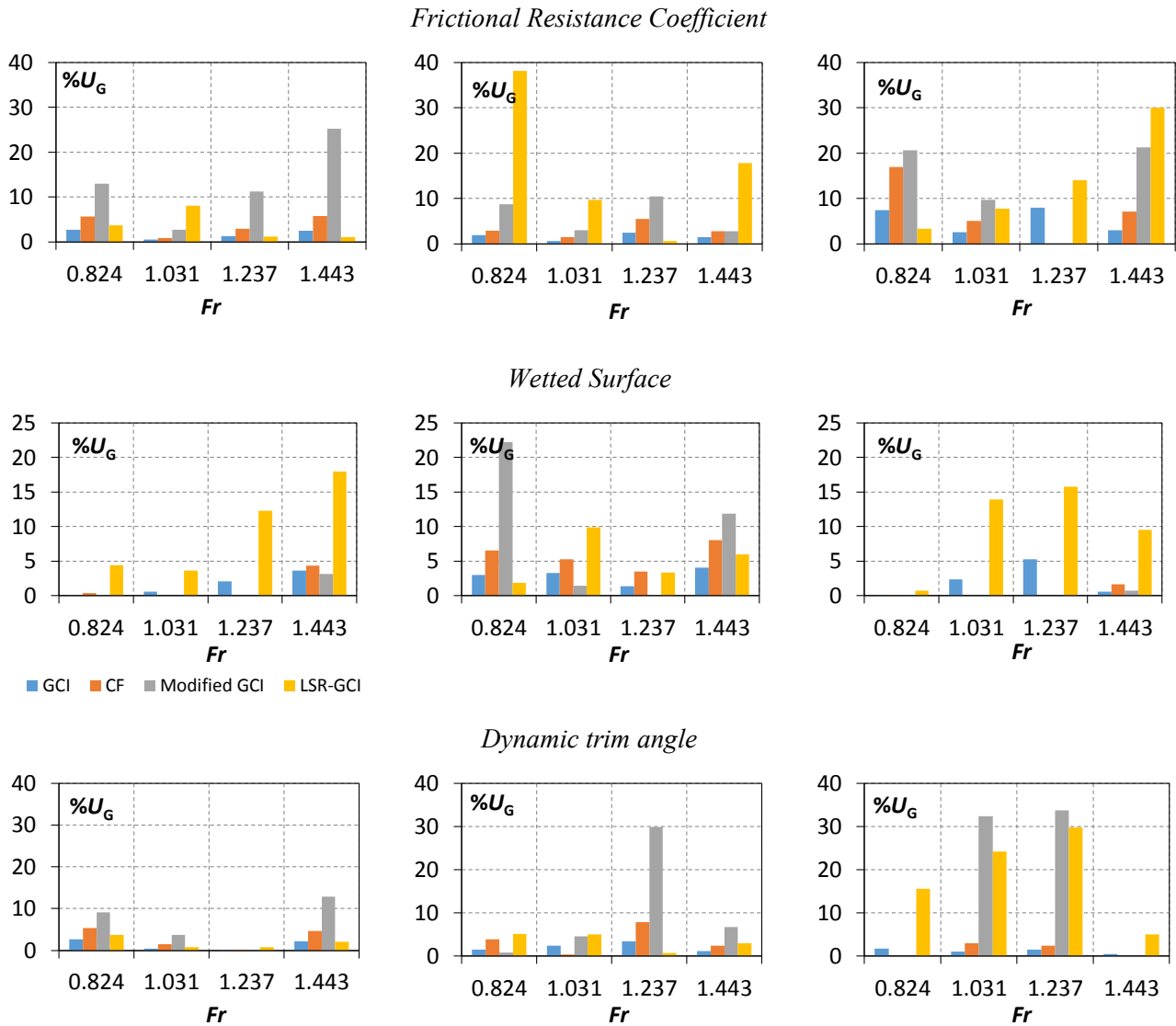


Figure 45 Grid uncertainty values for the different models tested, for the GCI, CF and modified GCI the values reported are a mean between the two studies: D-A-C and A-C-B

The results indicated that the monotonic convergence is not achieved in a few cases. However, for all of the models, the trends of the response variables are far from the asymptotic range in most of the cases that are studied, as indicated by the $1 - C_G$ values (asymptotic range: $1 - C_G \rightarrow 0$). In particular the C_F , S_W and dynamic trim are globally not in line with the asymptotic condition and exhibited more scatter than the other variables.

Moreover, in the majority of the cases, the values of p_G were either less than 1 or greater than 2. As shown by Eça & Hoekstra [28], the estimated order of accuracy determines a δ_{RE} over-conservative estimation, when $p_G < 1$. When $p_G > 2$ (the value of the theoretical order of accuracy), δ_{RE} was not reliable because it underestimated U_G . For these reasons the GCI, CF and modified GCI methods tended, in general, to give an unreliable evaluation of the grid uncertainty (as for the time-step convergence analysis).

When the LSR-GCI method is used, the problems reported above are accounted for and it is possible to observe a trend of uncertainty in relation to the grid, using the LSR approach.

The grid uncertainty values for the models, as estimated by the LSR-GCI method, are reported in the Appendix B, and below are shown only the U_G for the total resistance coefficient.

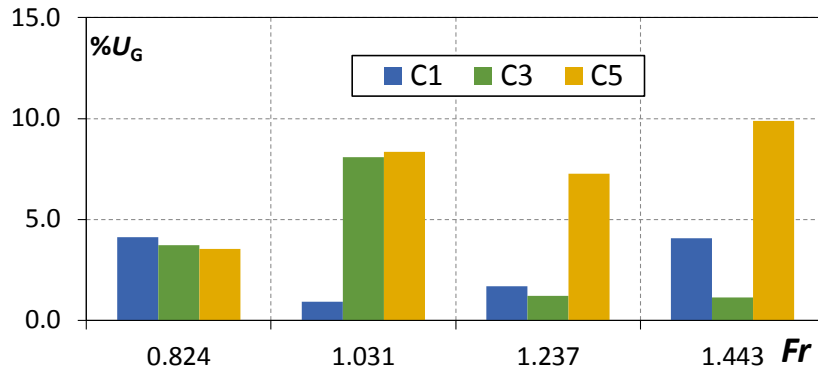


Figure 46 Grid uncertainties for C_T evaluated by LSR-GCI method for the different hull models

5. Statistical convergence analysis

Concerning the statistical convergence study, the evaluation is conducted using the oscillations of the mean running data in the last seconds of the time history of the response variables, as proposed by Xing et al. [76]. The statistical errors obtained for the finest grid are less than 0.40 % for all cases and all response variables, as shown in Figure 48. In particular for the dynamic trim angle the statistical error is less than 0.20 % for all mesh cases tested.

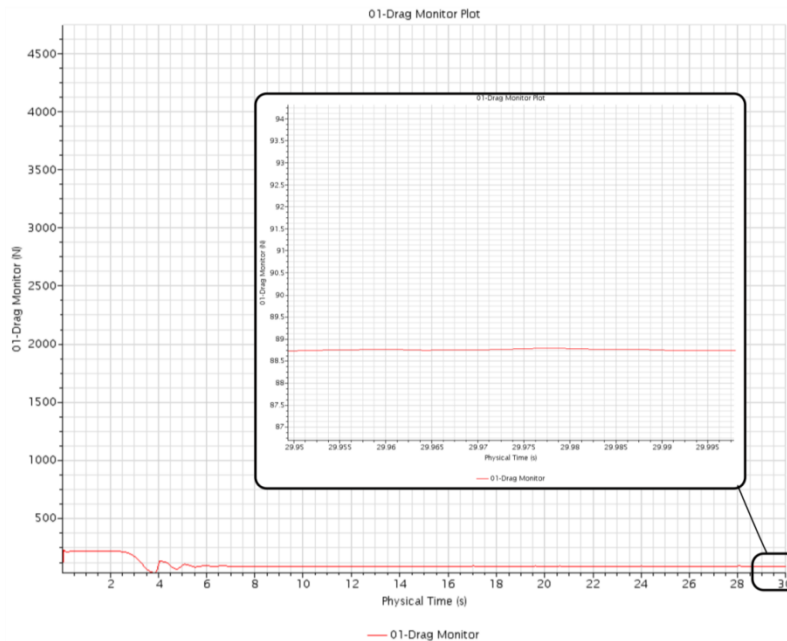


Figure 47 Example of time history of the drag of the C1 model at $Fr = 1.443$

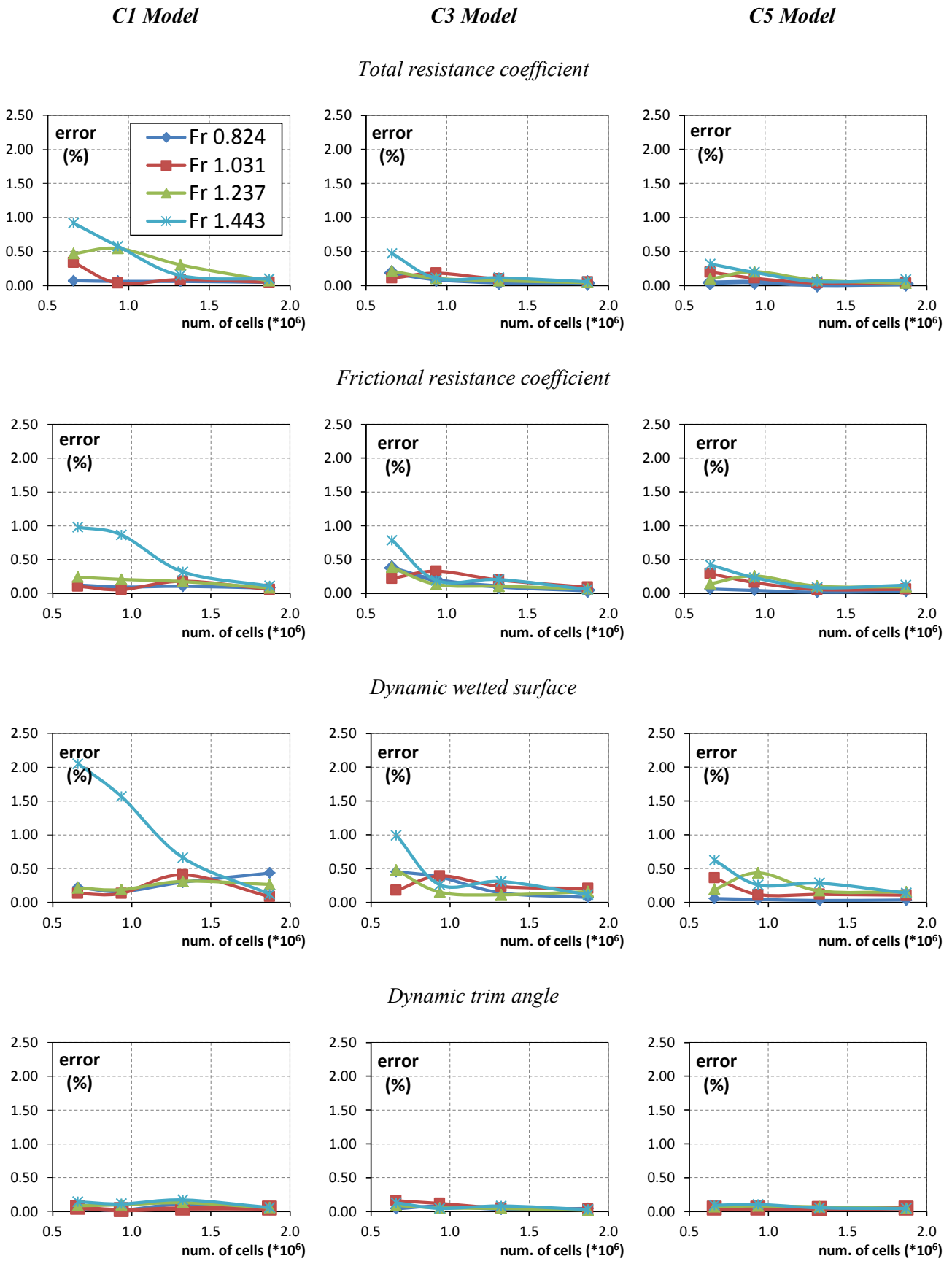


Figure 48 Statistical errors of the response variables for the different models and the different Fr tested

6. Response variables validation

The solution validation process assessed the modelling uncertainty, according to the procedure that is described previously. This analysis required E , U_{SN} and U_D . All data are reported in Appendix B. The distribution of E and U_V for the C1, C3 and C5 models versus Fr are shown in Figure 49.

The U_V is composed by the different sources of uncertainty, as reported in equations 7 and 34. The U_D is evaluated according to the information reported in Chapter 4. The grid and time-step uncertainty are evaluated following the LSR-GCI method. The U_G and U_{ST} are calculated for all models instead of the U_I and U_{TS} , which are evaluated only for the C1 model and the results are extended to C3 and C5 models.

The comparison error shown in Figure 49 is related to the finest triplet (A-C-B); the percentage value of the comparison error and uncertainty are referred to the solution of the finest grid simulation.

The graphs below reported show that the validation process for C_T is achieved only for the C3 model at $Fr = 0.824$ and 1.031 and for the C5 model at $Fr = 1.031$ and 1.443 .

The C_F is validated for C1 at $Fr = 1.031, 1.237,$ and 1.443 , for C3 at $Fr = 0.824$ and 1.031 and for C5 only for $Fr = 1.443$.

The S_W is validated for C1 and C3 in the whole range of Fr values and for C5 at $Fr = 0.824$ and 1.443 .

Concerning the dynamic trim the validation process is achieved for C1 at $Fr = 1.237$ and 1.443 , for C3 at $Fr = 0.824$, and for C5 at $Fr = 0.824, 1.031,$ and 1.237 .

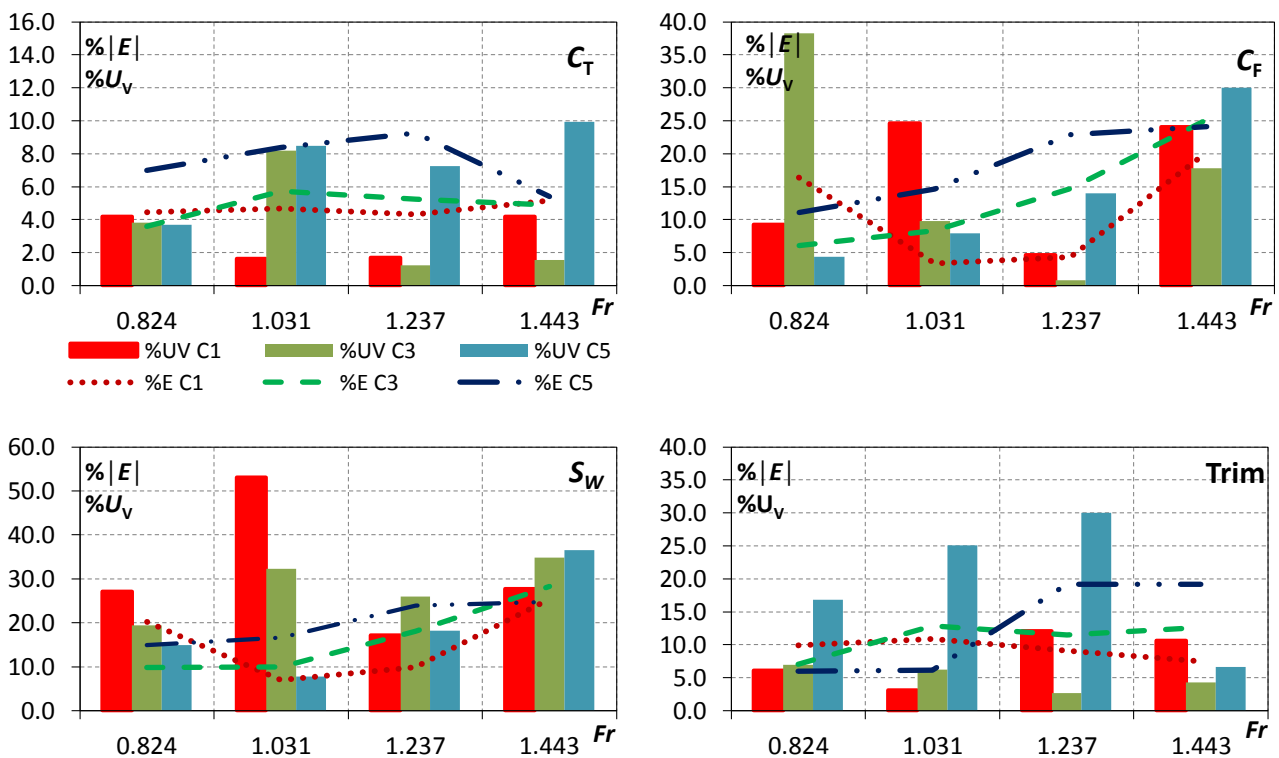


Figure 49 Validation uncertainty (bars) and comparison error (dashed lines) for the different models that were tested, the uncertainties were evaluated using the LSR-GCI method

7. Summary of numerical analysis results

The above analysis shows that the magnitude of validation uncertainty for C_F , S_W and τ is higher than the values for C_T . Hence the level of confidence of the CFD results for these response variables is less respect to the C_T results. Moreover, it can be observed that in most of the cases, when E is similar to but lower than U_V , the modeling error is hidden in the numerical and experimental noise. However, in the cases in which $|E| \gg U_V$, δ_{SM} is significant and the main challenge becomes the improvement of simulation modeling. More considerations also appear when the average values of comparison errors are observed (Figure 50), *i.e.*, there is an increasing trend when L/B increased. It is consistent with the expectations, as indicated in the Chapter 4.

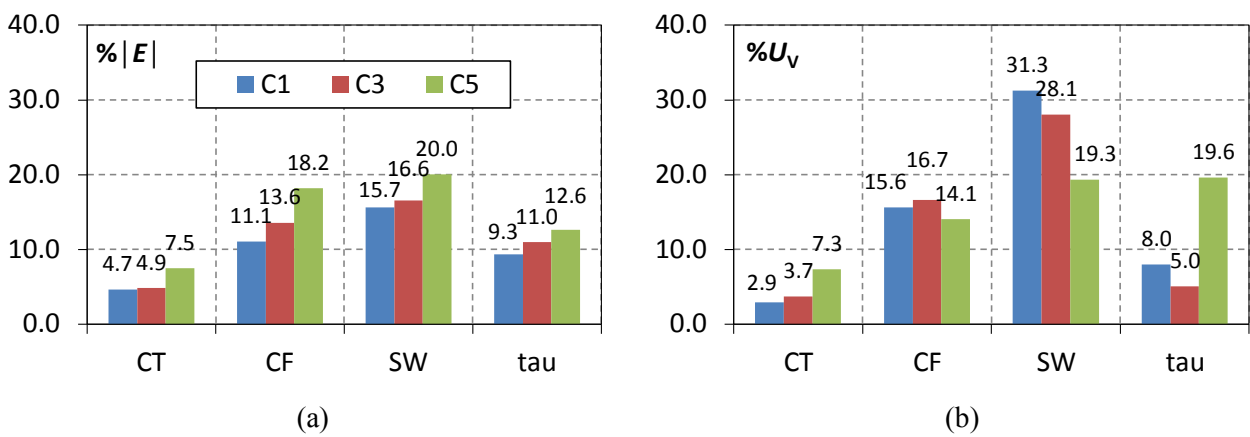
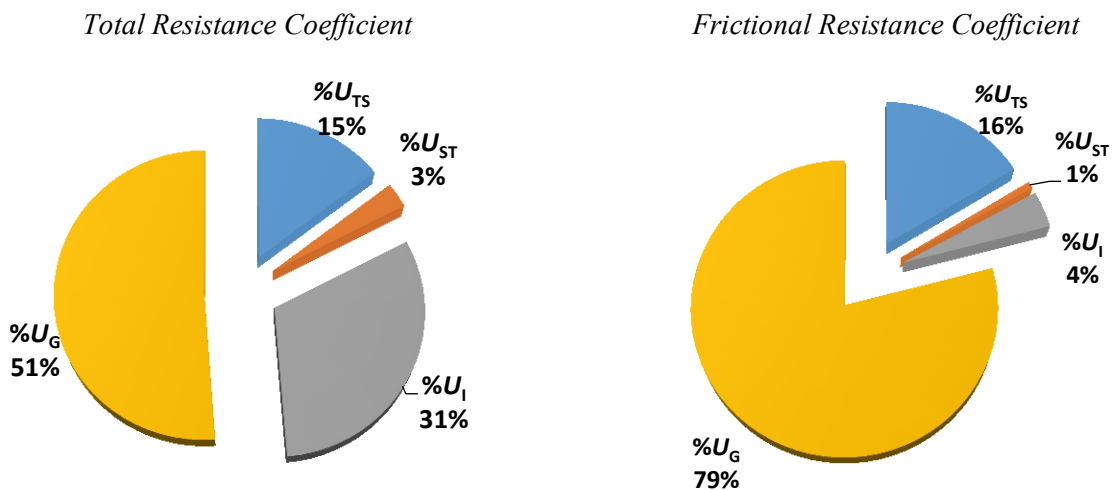


Figure 50 (a) Average comparison error and (b) average validation uncertainty for the three models that are tested

When the values of the different sources of uncertainties (shown in Appendix B) were compared, it is observed that, in all cases, the grid is obviously the main source of error in the simulations, as indicated in Wilson et al. [77]. The Figure 51 shows that U_G represents up to 89% of the U_{SN} of the response variables.



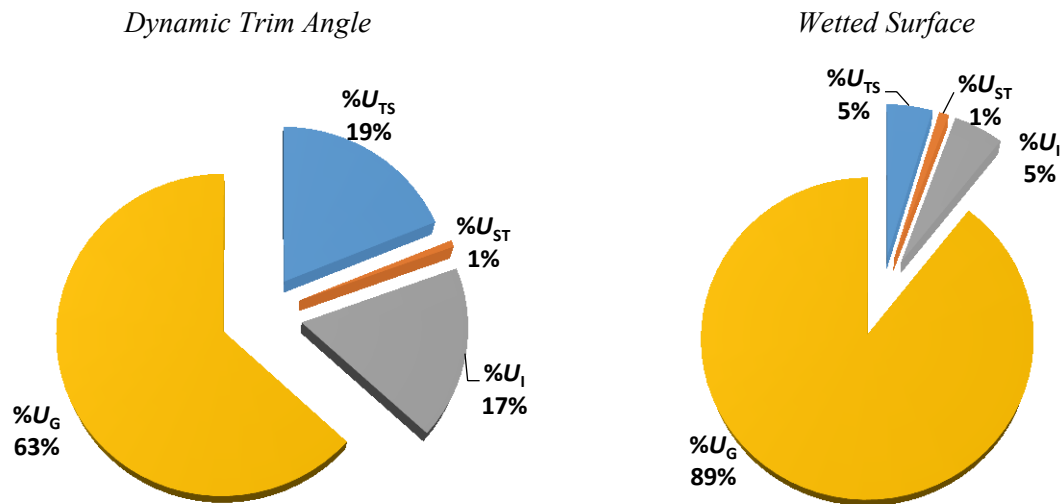


Figure 51 The U_{SN} percentage compositions
(average values respect to the three hull models and the four speeds)

In addition the percentage values of the other sources of error (U_{TS} , U_I , and U_{ST}) are quite constant and represent, in general, the 2 % of the simulation results. However the weight of the other sources increases when the U_{SN} is small, such as for C_T , and decreases increasing the U_{SN} value, *i.e.* for C_F , τ , and S_W .

Finally it is important to observe that the average comparison error of C_T for all models is less than the error values indicated by ITTC for unconventional and planing hulls, as mentioned in the Chapter 1.

8

WAVE PROFILE V&V

1. Introduction

This chapter reports the results of the V&V study conducted on the wave pattern profiles of the C1 model at four values of Fr .

Wave cuts are obtained as the intersection of the wave pattern with a cutting plane from $0 \leq x/L \leq 1$, where $L = 3.960 L_{WL}$ (*i.e.*, $L = 9.5$ m). The cutting plane is positioned at $0.469 L_{WL}$ (*i.e.*, 1.125 m) from the symmetry plane, as shown in Figure 52.

The verification study is performed in similarly fashion like the grid convergence study, following the uncertainty estimation procedures recommended in ITTC [21] and Wilson et al. [77] for the point-variables verification.

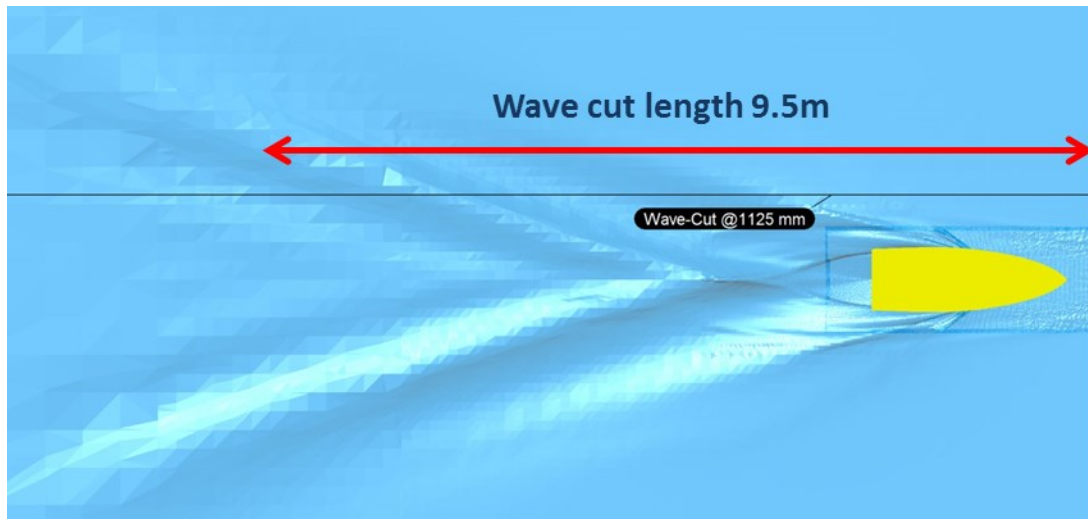


Figure 52 Visualization of wave cut length and position

2. Estimating uncertainties for point-variables

The evaluation of R_k and p_k for point-variables can be problematic, when the solution changes (ε_{ijk}) go to zero. In this case the ratio becomes ill conditioned. In order to avoid this problem, the L2 norms of the solution changes are used to define r_k and p_k , *i.e.*

$$\langle R_k \rangle = \frac{\|\mathcal{E}_{k_{21}}\|_2}{\|\mathcal{E}_{k_{32}}\|_2} \quad (56)$$

$$\langle p_k \rangle = \frac{\ln\left(\frac{\|\mathcal{E}_{k_{32}}\|_2}{\|\mathcal{E}_{k_{21}}\|_2}\right)}{\ln(r_k)} \quad (57)$$

Where $\langle \rangle$ and $\|\cdot\|_2$ is used to denote a profile-averaged value and $\|\varepsilon\|_2$ is equal to the following equation.

$$\|\varepsilon\|_2 = \sqrt{\sum_{k=1}^N \varepsilon_k^2} \quad (58)$$

Equation 58 denotes the L2 norm of solution change over the N points examined in the region of interest (in this case in $0 < x/L < 1$). Caution should be exercised when defining the convergence ratio R_k from the equation 56 because the oscillatory condition ($R_k < 0$ and $|R_k| < 1$) cannot be diagnosed since will always be greater than zero.

Good practice is to examine the local values at solution (e.g. maximums or minimums) in order to confirm the convergence condition based on an L2 norm definition.

To verify the solution, the GCI, CF, and modified GCI methods can be used to estimate distributions of U_k at each point.

It should be noted that, in this case, the GCI-LSR method is not used because it is not suitable for point analysis of the variables, due to the application of the LSR method at each variables point, in particular when the numbers of point are very high.

An alternate approach suggested by Hoekstra et al. [78] is to transform the spatial profile to wave number space and to perform a convergence study on the amplitude distribution of the Fourier modes. In principle, this approach could remove the problem of ill-conditioning of the R_k .

3. Wave cut V&V for C1 model

As indicated, the wave profile is described by a point variable defined over a distribution of grid points. The L2 norm of errors point distributions and uncertainties are used to assess the verification levels and judge whether validation is achieved globally.

The profile-averaged convergence ratio ($\langle R_G \rangle$), estimated order of accuracy ($\langle p_G \rangle$), correction factor ($\langle C_G \rangle$), global grid uncertainty U_G , and the comparison error with the experimental data are reported in Table 14. The GCI, CF, and modified GCI methods are used to estimate the distributions of U_G .

Table 14 Profile-averaged values from wave profiles in the V&V study (all of the percentage values is referred to ζ_{max} , i.e. the maximum value for each wave profile)

Fr	Grid Study	$\langle R_G \rangle$	$\langle p_G \rangle$	$\langle I-C_G \rangle$	% U_G GCI	% U_G CF	% U_G mod GCI	% U_{SN}	% U_D	% U_V	% $ E $
0.824	D-A-C	0.80	0.64	0.25	1.95	3.25	12.41	12.4	1.1	12.5	1.2
	A-C-B	0.77	0.76	0.30	1.23	1.97	7.04	7.0	1.1	7.1	1.1
1.031	D-A-C	0.37	2.87	1.71	0.26	0.07	1.50	1.5	1.0	1.8	2.0
	A-C-B	1.01	-0.03	-0.01	N.A	N.A	N.A	N.A	1.0	N.A	1.9
1.237	D-A-C	0.42	2.48	1.36	1.00	0.19	3.68	3.7	3.0	4.7	4.2
	A-C-B	0.88	0.38	0.14	8.45	15.32	65.80	65.8	3.0	65.9	3.8
1.443	D-A-C	0.72	0.93	0.38	5.51	8.23	26.38	26.4	3.2	26.6	5.1
	A-C-B	1.19	-0.51	-0.16	N.A	N.A	N.A	N.A	3.2	N.A	4.4

Table 14 reports only the grid uncertainty values because the other sources of error, such as iteration and time step, are negligible with respect to the grid. The E is evaluated by comparing the EFD data with the solution of the finest grid in each grid study. The two grid studies, i.e., (D-A-C) and (A-C-B), present a monotonic convergence at all speeds that are tested, with the exception of the divergence in the case of A-C-B at $Fr = 1.031$ and 1.443.

In all of the cases in which convergence is achieved, validation is reached at the U_V level. In order to confirm the trend identified by the average quantities, a point analysis is conducted in the crests/hollows of the wave profiles. At $Fr = 0.824$, the point analysis shows a convergence condition for the D-A-C case, whereas the A-C-B case diverges monotonically. As for the averaged trend for $Fr = 1.031$, punctual monotonic convergence condition is achieved only for the D-A-C case. At $Fr = 1.237$ and 1.443 the convergence conditions are reached for the D-A-C and A-C-B cases for the crests, but only the D-A-C case shows monotonic convergence for the hollow.

Figure 54 shows the wave profile obtained with the four grid configuration at the different Fr values and in this figure the hull is located with the transom at $x/L = 0$ and the forward perpendicular at $0.253 x/L$.

The agreement with the experimental result is quite good, but the differences exist for both amplitude and phase. In addition, these discrepancies increase as Fr increases, as highlighted by the comparison of the errors in Table 14. One of the main causes of differences in terms of phase and amplitude of the wave pattern could be related to incorrect assessment by the CFD angle between the keel line and the stagnation line.



Figure 53 Visualization of EFD (up) and CFD (down) stagnation line at $Fr = 1.237$

Regarding the evaluation of the grid uncertainty, the modified GCI also gives a U_G values that are significantly greater than the other methods for the V&V study of the wave profile.

A qualitative comparison between the wave patterns around the hull detected in towing tank tests and the CFD simulations is shown in the Appendix C.

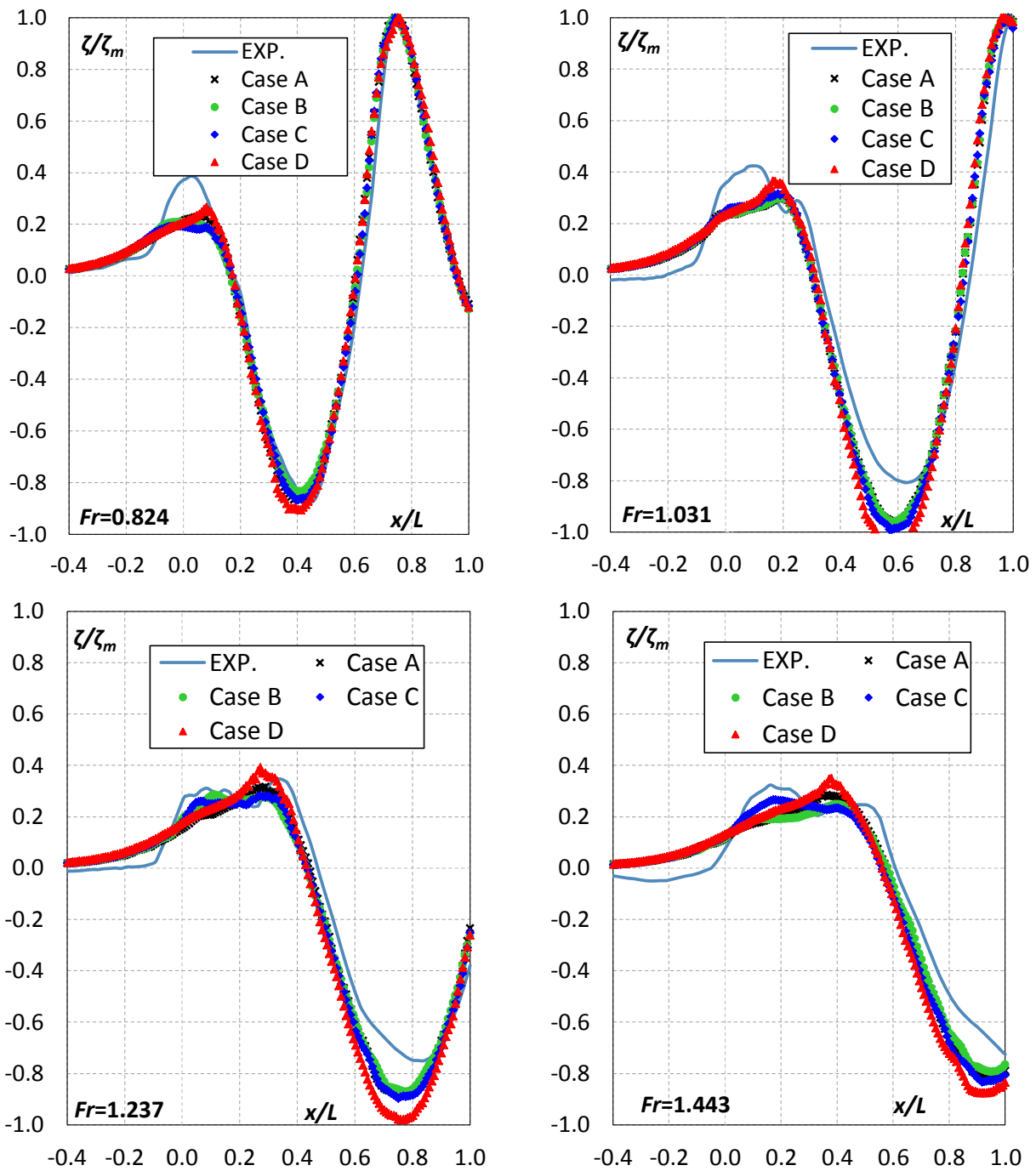


Figure 54 Comparison of the wave profiles for EFD and CFD data for the four different grids at different Fr values

4. Wake refinement extension

A further analysis was performed increasing the extension of the cutting plane from $L = 3.960 L_{WL}$ to $L = 7.920 L_{WL}$ (i.e., $L = 19.0$ m), as shown in Figure 55. The comparison is conducted between the EFD and CFD (Case B) wave profiles.

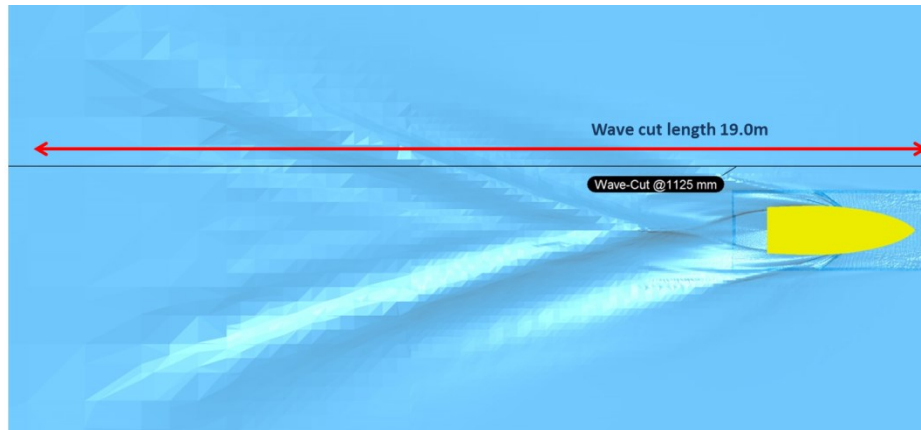


Figure 55 Visualization of extended wave cut length

Observing the comparison of EFD and CFD (Case B) wave profiles (Figure 57), it can be seen that all the CFD data agrees well with the experimental data along the majority of the surface free surface analysed. However some differences are observed at the region far from the hull. This effect is due to the extension of the wake refinement mesh.

In order to improve the resolution on the far field, the grid topology of case B is modified (Case B-Mod.) by an extended wake-refinement mesh, as shown in Figure 56.

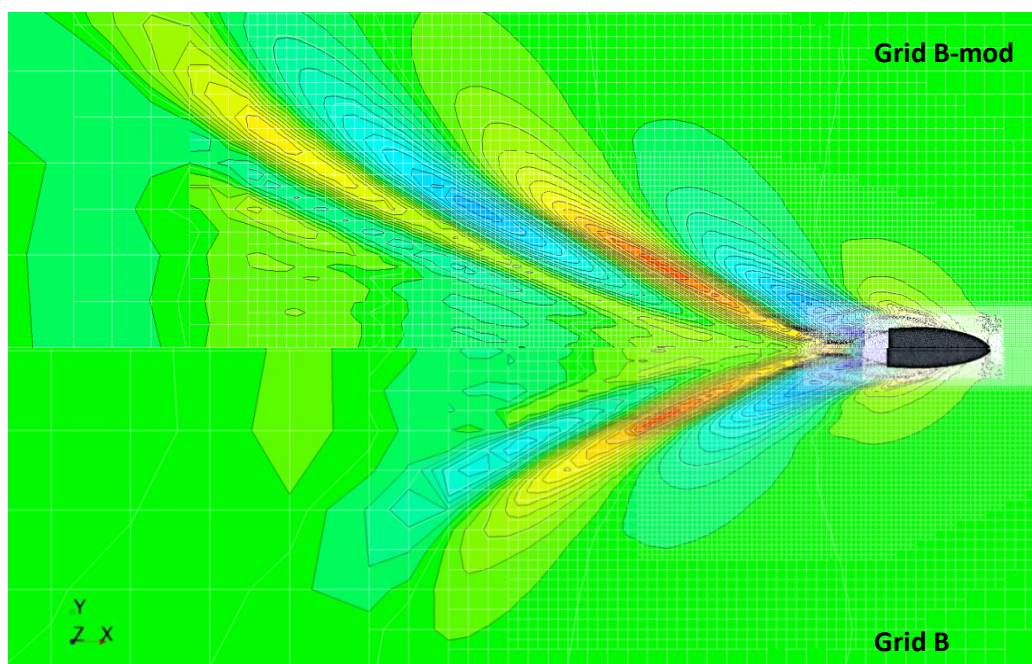


Figure 56 Effect of the extension wake-refinement mesh on the capturing of the wave

The extension of the wake-refinement mesh determined a significant improvement in the capturing of the wave. Hence in the grid Case B-mod the far field wave profile is well simulated for all Fr tested, as reported in Figure 57.

Interestingly the extension of the mesh wake-refinement does not have almost impact on the results of the response variables; despite has a significant impact on the far field of the wave cut traces.

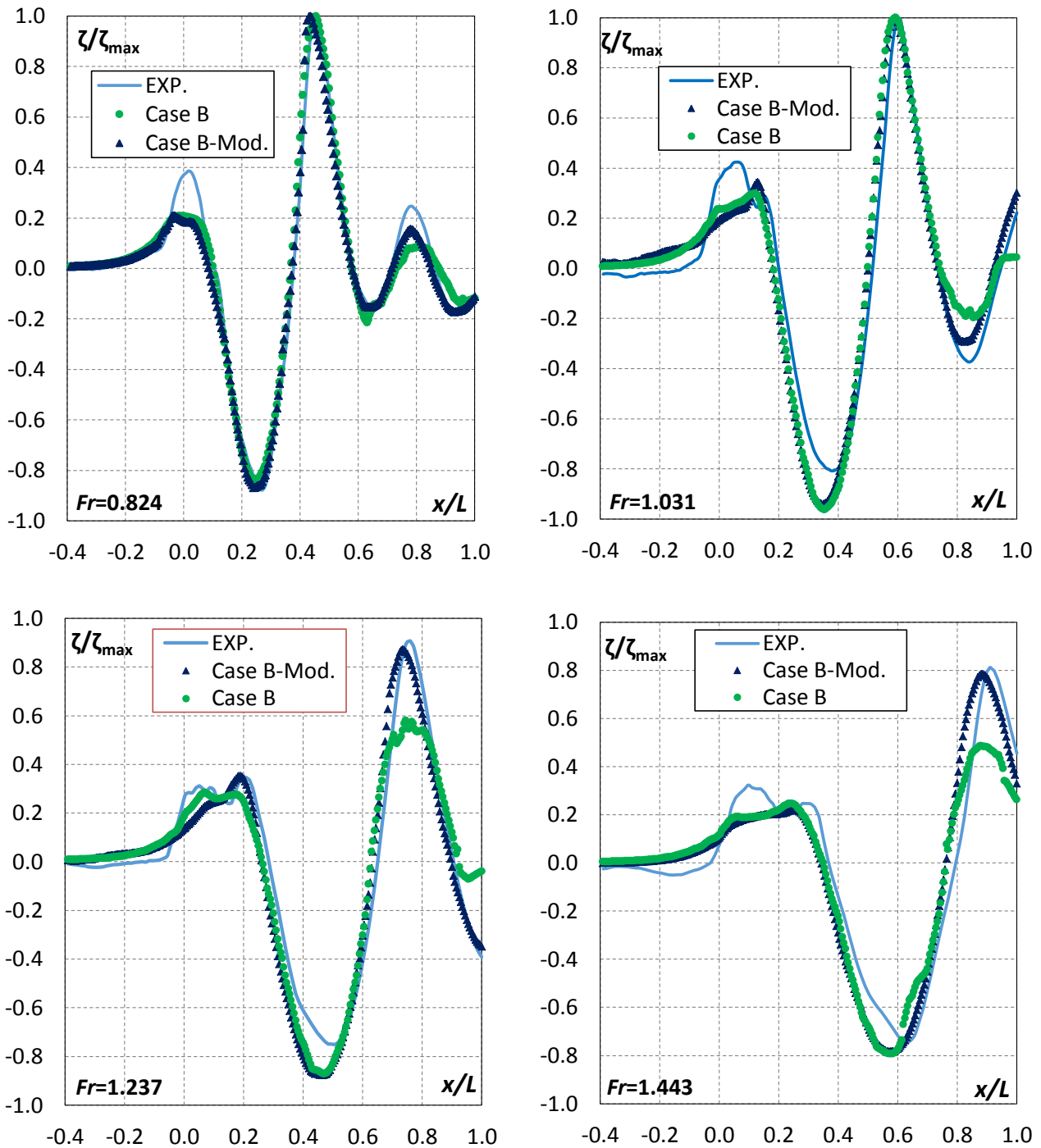


Figure 57 Comparison of the extended wave profiles for EFD and CFD data for the Case B and Case B-Modified at different Fr values

9

FURTHER ANALYSIS

After the modeling and numerical analysis conducted on the C1, C3, and C5 models using the overset grid technique, two further analyses are conducted in order to evaluate other aspects, in particular:

- The evaluation of the grid uncertainty using mesh morphing technique, although the high computational effort.
- The role of the deadrise angle (β) in the comparison error and grid uncertainty.

1. Morphing mesh-grid independence analysis

As reported in the Chapter 7, the morphing mesh technique is compared with the others dynamic mesh methods and the results showed that the MHG technique gives the best trend. However, choosing the optimum in terms of accuracy of the results and required calculation time, the OG technique is selected. Hence in order to evaluate the uncertainty provided by the MGH a grid independence analysis is conducted at $Fr = 1.031$, using five meshes with uniform refinement ratio ($\sqrt{2}$). The five grid cases used are reported in Table 15.

Table 15 C1 morphing case: base size and total number of cells of the five grids that are examined

	<i>Cells</i>	<i>Base Size</i>
Grid D	1855777	0.037 L_{WL}
Grid A	2624465	0.033 L_{WL}
Grid C	3711554	0.029 L_{WL}
Grid B	5248930	0.025 L_{WL}
Grid E	7423108	0.021 L_{WL}

The grid independence analysis is performed using the GCI-LSR method. The results of the grid are reported in Figure 58 and it can be observed that significant improvement is obtained for the U_G values of C_F and S_w , Figure 58 (a). Concerning the comparison error, the results show a reduction of E for all response variables except for the C_T , Figure 58 (b).

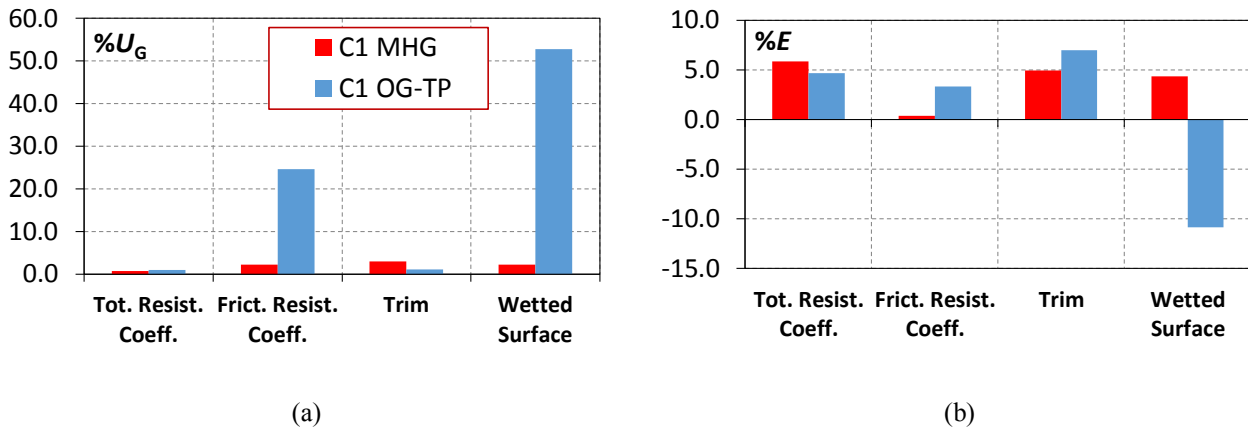


Figure 58 (a) Grid uncertainty and (b) comparison error for morphing mesh case at $Fr = 1.031$

For the purpose of validation process, only the U_G grid is estimated and for the other sources of uncertainty (U_I and U_{TS}) the data provided for the OG-TP case is used.

The results of validation process are consistent with the OG-TP case at $Fr = 1.031$ and the validation is reached for the C_F and τ . The difference is that the validation is achieved at the interval of U_G less than the OG-TP case (e.g., C_F : 2.5% instead of 24.6%).

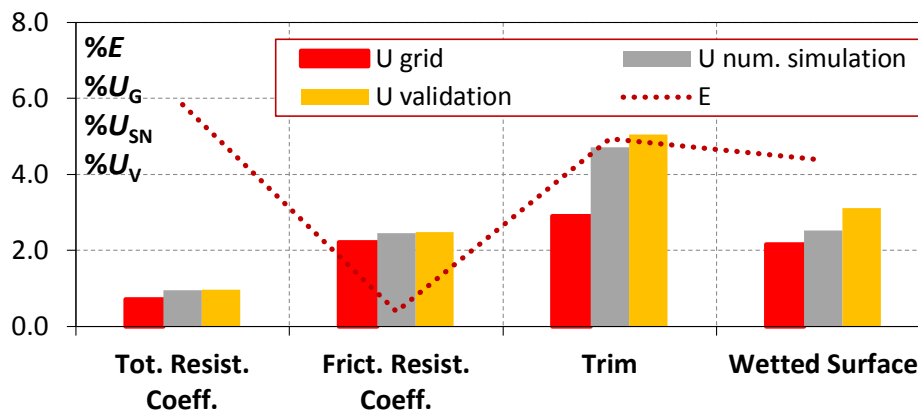


Figure 59 Grid, simulation, and validation uncertainty (bars) and comparison error (dashed line) for the C1 model at $Fr = 1.031$

Another aspect observed is the improvement in the evaluation of the wave profile, in particular in the region near the hull, in terms of the estimated wave amplitude, as shown in Figure 60.

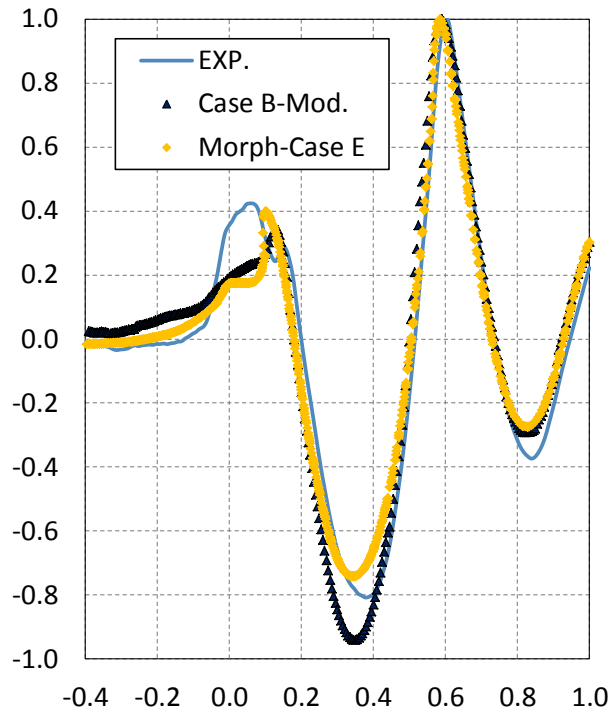


Figure 60 Comparison of the wave profile at $Fr = 1.031$ of morphing and modified-OG cases

2. Monohedral hull (SS-DIN)

The hull geometries used so far are characterized for the reduction of the deadrise angle (β) from the bow to the stern (warped hull). As previously mentioned the β is one of the two main geometrical parameters that influencing the pressure distribution on the hull bottom. The other parameter is the slenderness ratio L/B . Both of these parameters increase the divergence of the streamlines, increasing the transversal pressure gradient. The role of L/B in the generation of error and uncertainty is evaluated in the previous chapter (Chapter 7) by the three models of SSN. The warped hull geometry is more complex in particular as regards the determination of the distribution of pressure on the bottom compared to the monohedral hull (β fixed along the bottom). More details on the pressure distribution on the warped hulls are explained in many works, for example Morabito [79] and Pennino et al. [80].

For the reasons above explained, is essential to complete the V&V study analyzing an example of monohedral hull. The MONO hull of the Systematic Series DIN [32] (Chapter 4) was examined, Figure 61. This choice is significant also for the lower deadrise angle of the SS-DIN model.



Figure 61 Profile of MONO hull of SS-DIN

a. Grid independence analysis

The simulations conducted on the MONO hull are carried out using the same setup of the SSN models (OG TP mesh case). The grid independence analysis are performed using four different mesh configurations obtained by $\sqrt{2}$ uniform refinement ratio, as shown in Table 16. The tests are conducted to four speeds ($Fr = 0.788, 1.066, 1.332, \text{ and } 1.464$) and the response variables examined are the C_T, S_W and τ .

Table 16 MONO hull: base size and total number of cells of the four grids that are examined

	Cells	Base Size Background	Base Size Overset
Grid D	1004229	0.95 L_{WL}	0.35 L_{WL}
Grid A	1432240	0.90 L_{WL}	0.32 L_{WL}
Grid C	2147252	0.87 L_{WL}	0.28 L_{WL}
Grid B	3036673	0.82 L_{WL}	0.25 L_{WL}

The results of the simulations are shown in Figure 62 and are presented in terms of percentage of the comparison error between the EFD and CFD data for the four meshes and the four speeds tested.

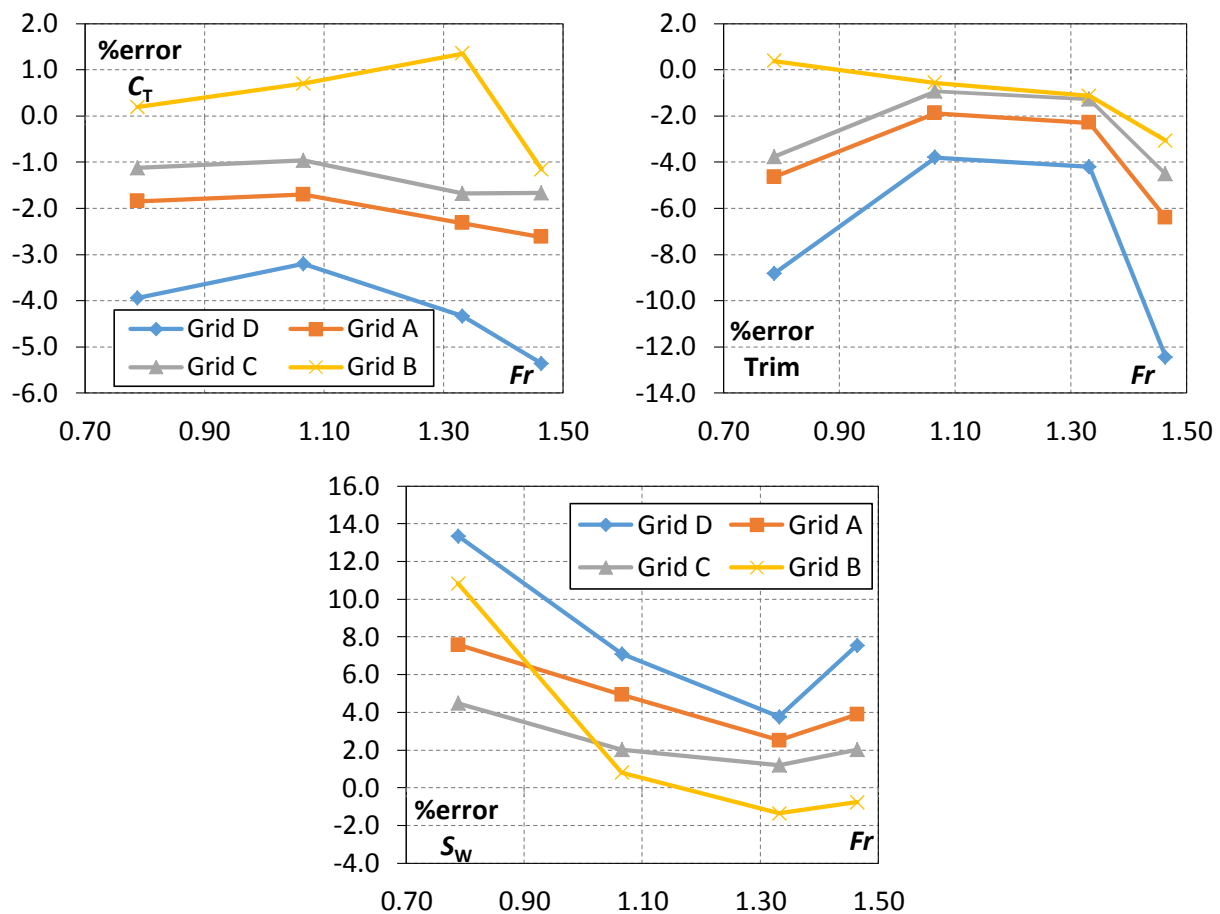


Figure 62 Percentage comparison errors between EFD and CFD data for the SS-DIN MONO model at four Fr and four grids tested

The comparison error is consistent with the grid refinement results, except for the $Fr = 0.788$ where the trend of trim error is not convergent with mesh refinement, and the numerical solution is reasonably close to the experimental data for the finest grid (Case B). It is important to note that, as for the C1, C3, and C5 models, the comparison error of C_T is less than the error values indicated by ITTC for unconventional and planing hulls [6].

Hence the U_G is assessed using the LSR-GCI method. The others sources of uncertainty were not investigated. The U_V is evaluated increasing the U_G with a value of 2% that is a reasonable estimation of the percentage mean value of the sum of U_{TS} and U_I . The U_D was evaluated according to the ITTC prescription in the similar way reported in Chapter 4. The validation, as shown in Figure 63, is achieved for all cases.

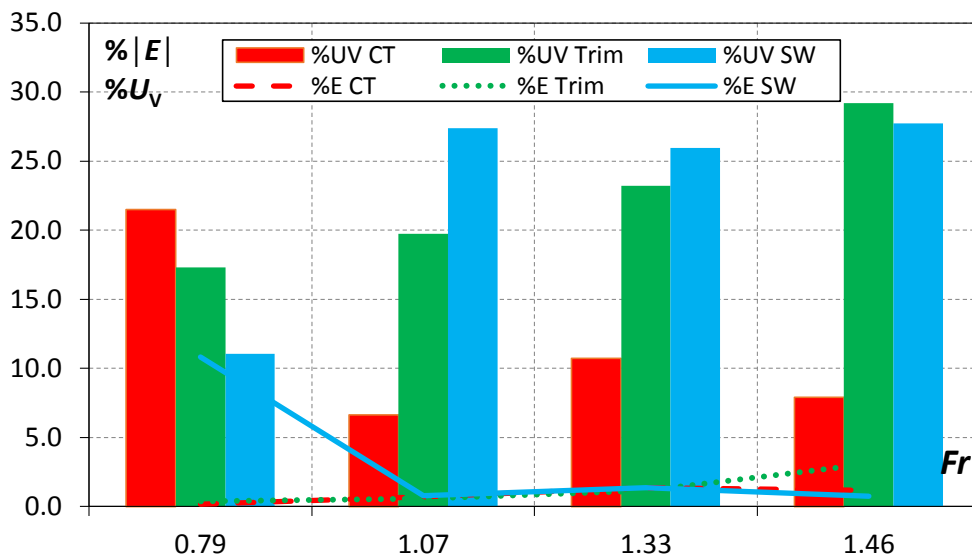


Figure 63 Validation uncertainty (bars) and comparison error (lines) for the MONO hull

b. MONO vs C5

The MONO hull is compared with the C5 model, which is the comparable hull of SSN in terms of the slenderness ratio and in particular the E of the response variables of MONO hull is compared with the E of C5. The Figure 64 suggests that the E is very geometry dependent, in spite of the U_G that is relatively constant, except for the C_T at $Fr = 0.788$. Then it is clear that the comparison error is strictly related to the L/B , as shown in Figure 50, and to the deadrise angle (Figure 64). Furthermore is interestingly to observe the difference between the warped and monohedral hull in terms of visualization of the streamlines on the hull bottom, as reported in Appendix E. It can be seen that the MONO hull shows streamlines more divergent respect to the warped hulls.

Total resistance coefficient

Dynamic trim angle

Wetted surface

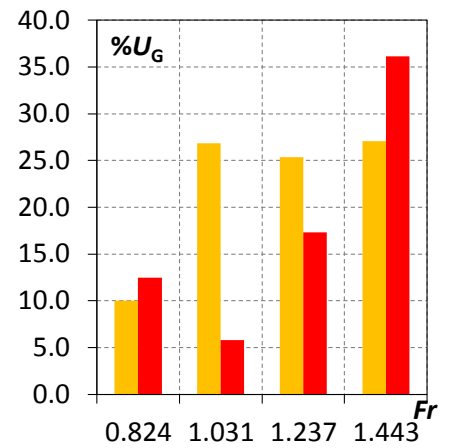
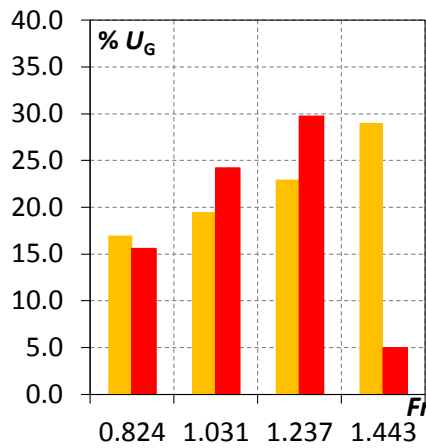
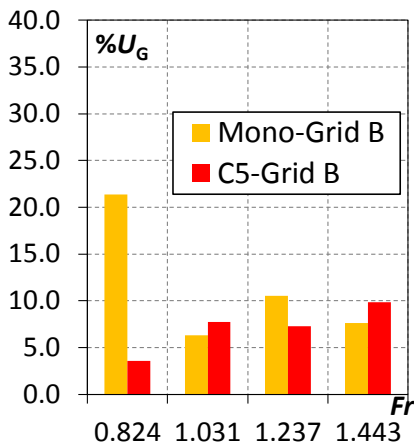
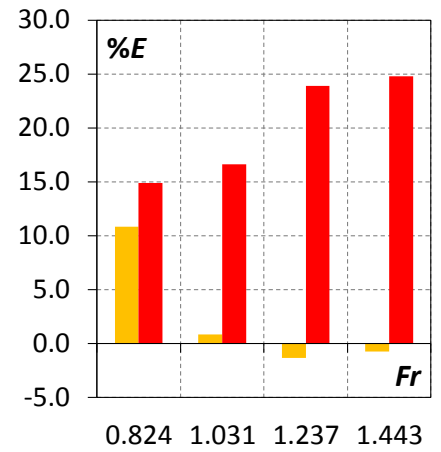
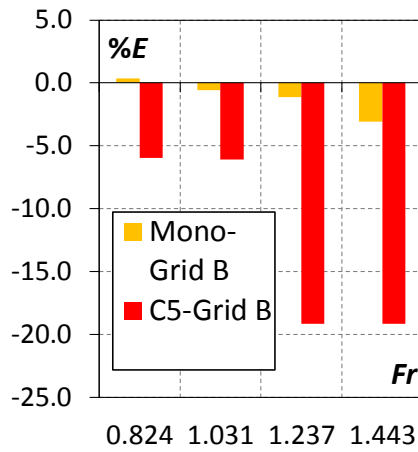
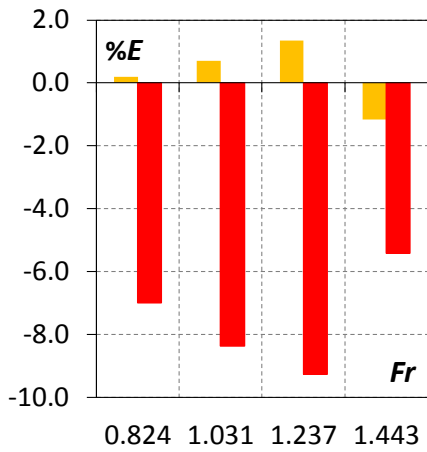


Figure 64 Comparison errors and grid uncertainty of C5 and MONO hull for the finest grid at the respectively four Fr

10

CONCLUSIONS

A comprehensive V&V study is presented in this work in order to evaluate the reliability of (U)RANS simulations applied to the estimation of planing crafts performance. As well known, the simulation of the planing hull resistance test is affected by the largest errors in the evaluations performance rather than the displacement hulls. This is strictly related to the errors in the evaluation of dynamic trim, and so in the difficulties identifying the pressure distribution on the hull bottom.

The work is conducted by simulating the resistance test of four hull models that have geometric differences essentially related to the variations of the L/B and the β . The three warped hulls of NSS (C1, C3, and C5) are characterized by increasing the values of L/B , while one hull of the SS-DIN is characterized by the constant value of β (MONO). The different degrees of slenderness of the NSS warped hulls were obtained by stretching a parent hull with the aim of ensuring the homothety of the transversal sections and isolating the influences of slenderness on the dynamic of the planing.

The V&V study is performed using the main methods and procedures available in literature (*i.e.*: GCI, CF, Modified GCI, and LSR-GCI) in order to evaluate the errors and uncertainties. The response variables that are calculated through the simulations are C_T , C_F , τ , and S_W .

This study involves two stages, *i.e.* the modeling analysis and the numerical analysis.

The results of modeling investigation confirm that the simulations of the planing crafts are critical with respect to the displacement hulls. However, the comparison error of C_T is reduced reaching values lower than 7.5 % (instead of the 10.0 % as declared in the ITTC Specialist Committee on CFD in Marine Hydrodynamics [6]). Also, greater simulation reliability is achieved by using the non-conventional approaches, such as the morphing and overset mesh techniques. Both of them ensure high-quality of the simulation results and show high-adaptability to the wide variations of trim and heave of the planing crafts. The morphing mesh obtains the best results (C_T errors lower than 5.8 %), but the overset mesh is the best compromise in terms of accuracy of the results and the computing resources required. Hence the overset mesh reduces the number of cells, in particular when the unstructured grid is used. With both of these techniques it is able to avoid the problems related to the use of a single grid with rigid body motion. Furthermore a solution for the artificial mixing of air and water on the hull bottom (NV problem) is provided.

The numerical analysis recognized that the grid, with respect the other sources of errors, is the main contributor to the numerical simulation error (δ_{SN}) and uncertainty (U_{SN}), as confirmed by Wilson et al. [77].

The other sources of error investigated, such as time-step, iteration, and statistical, are quite constant and represent, in general, the 2 % of the simulation results.

It can be observed that with the complex flow, which is typical of such hulls, the unstructured grids are more appropriate respect to the structured grids, in spite of the high dispersion of data and the greater difficulty in achieving monotonic convergence. As a consequence of these drawbacks and contrary to ITTC's suggestions, the results of the study showed that the LSR-GCI method, recently developed by Eça and Hoekstra, is the most reliable approach among those tested to evaluate the uncertainties. Furthermore the analysis of the comparison errors for the four models shows the high-dependency of E to the hull geometry (L/B and β). In some cases the errors are significantly greater than the validation uncertainties. This emphasizes the need to improve furtherly simulation models because the current models generate more errors than the numerical solution errors.

Regarding the wave profile analysis the V&V procedures are applied to a point-variables data. The improved reliability of the simulations is consistent with the good correlation between the numerical and experimental wave pattern. The estimated errors are less than 5.1 %. Moreover is tested also the extension of the wake-refinement mesh and it is observed a significant improvement in the capturing of the wave, in particular in the far field. It is interesting to note that the extension of the mesh wake-refinement does not have almost impact on the results of the response variables.

Finally it should be clear that the accuracy of a CFD result cannot be taken for granted, and verification and validation are mission-critical elements of the confidence-building process in the CFD capabilities, in particular in ship hydrodynamics field.

APPENDIX A: Time-step convergence analysis results

C1 model - Grid used: case D

Total Resistance Coefficient

<i>Fr</i>	<i>Time-step ratio</i>	<i>r_{TS}</i>	<i>p_{TS}</i>	<i>I-C_{TS}</i>	<i>%U_{TS} GCI</i>	<i>%U_{TS} CF</i>	<i>%U_{TS} mod GCI</i>	<i>%U_{TS} GCI LSR</i>
0.824	√2	0.67	1.14	0.51	0.12	0.20	0.53	0.36
1.031	√2	0.44	2.36	-0.26	0.01	0.01	0.02	0.06
1.237	√2	0.47	2.14	-0.10	0.04	0.03	0.07	0.25
1.443	√2	0.21	4.44	-2.67	0.02	0.11	0.36	1.06

Frictional Resistance Coefficient

<i>Fr</i>	<i>Time-step ratio</i>	<i>r_{TS}</i>	<i>p_{TS}</i>	<i>I-C_{TS}</i>	<i>%U_{TS} GCI</i>	<i>%U_{TS} CF</i>	<i>%U_{TS} mod GCI</i>	<i>%U_{TS} GCI LSR</i>
0.824	√2	0.19	4.82	-0.56	0.01	0.07	0.24	0.79
1.031	√2	0.23	4.23	-2.35	0.05	0.23	0.82	2.23
1.237	√2	0.25	3.95	-1.94	0.03	0.13	0.48	2.26
1.443	√2	0.34	3.06	-0.89	0.14	0.30	1.12	0.80

Trim

<i>Fr</i>	<i>Time-step ratio</i>	<i>r_{TS}</i>	<i>p_{TS}</i>	<i>I-C_{TS}</i>	<i>%U_{TS} GCI</i>	<i>%U_{TS} CF</i>	<i>%U_{TS} mod GCI</i>	<i>%U_{TS} GCI LSR</i>
0.824	√2	0.39	2.71	-0.56	0.03	0.06	0.20	0.45
1.031	√2	-1.59	N.A.	N.A.	N.A.	N.A.	N.A.	2.26
1.237	√2	0.45	2.27	-0.20	0.04	0.04	0.12	0.36
1.443	√2	0.16	5.27	-4.23	0.02	0.12	0.36	1.45

Wetted Surface

<i>Fr</i>	<i>Time-step ratio</i>	<i>r_{TS}</i>	<i>p_{TS}</i>	<i>I-C_{TS}</i>	<i>%U_{TS} GCI</i>	<i>%U_{TS} CF</i>	<i>%U_{TS} mod GCI</i>	<i>%U_{TS} GCI LSR</i>
0.824	√2	0.19	4.81	-3.30	0.01	0.09	0.30	1.01
1.031	√2	0.67	1.17	0.50	0.13	0.43	1.12	0.80
1.237	√2	0.72	0.92	0.62	0.08	0.43	1.37	0.51
1.443	√2	0.08	7.30	-2.07	0.02	0.09	0.33	0.85

U_{TS} was expressed as a percentage value of the simulation solution with the less time-step

APPENDIX B: Grid independence analysis and Validation results

C1 model – grid refinement ratio $\sqrt{2}$

Total Resistance Coefficient

<i>Fr</i>	<i>Grids</i>	r_G	p_G (RE)	p_G (LSR)	$ I-C_G $	% U_G GCI	% U_G CF	% U_G mod GCI	% U_G GCI LSR	% U_{SN}	% U_D	% U_V	% E
0.824	D-A-C	0.79	0.68	0.48	0.73	2.46	4.86	7.15	4.12	4.2	0.1	4.2	4.9
	A-C-B	0.80	0.65		0.75	2.05	4.08	6.70		4.2	0.1	4.2	4.5
1.031	D-A-C	-0.46	N.A.	-21.55	N.A.	0.91	N.A.	N.A.	0.91	1.2	0.1	1.2	4.8
	A-C-B	0.87	0.41		0.85	0.79	2.14	6.40		1.2	0.1	1.2	4.7
1.237	D-A-C	0.88	0.37	0.71	0.86	2.61	5.70	18.34	1.70	1.8	0.1	1.8	4.9
	A-C-B	0.87	0.41		0.85	1.99	4.31	12.89		1.8	0.1	1.8	4.3
1.443	D-A-C	0.87	0.41	0.68	0.85	5.39	11.62	34.81	4.06	4.3	0.1	4.3	4.8
	A-C-B	0.87	0.40		0.85	4.79	10.37	31.61		4.3	0.1	4.3	5.2

Frictional Resistance Coefficient

<i>Fr</i>	<i>Grids</i>	r_G	p_G (RE)	p_G (LSR)	$ I-C_G $	% U_G GCI	% U_G CF	% U_G mod GCI	% U_G GCI LSR	% U_{SN}	% U_D	% U_V	% E
0.824	D-A-C	0.79	0.66	0.32	0.74	4.27	8.50	13.70	8.83	8.9	0.6	8.9	15.7
	A C-B	0.65	1.25		0.46	3.45	5.28	15.92		8.9	0.6	8.9	16.4
1.031	D-A-C	0.30	3.49	0.03	1.36	0.19	0.57	6.50	33.13	24.7	0.4	24.7	3.7
	A-C-B	-1.10	N.A.		N.A.	N.A.	N.A.	N.A.		24.7	0.4	24.7	3.3
1.237	D-A-C	0.61	1.41	0.70	0.37	1.36	1.89	5.77	4.64	5.2	0.3	5.2	4.0
	A-C-B	0.52	1.89		0.08	0.88	0.81	7.17		5.2	0.3	5.2	4.3
1.443	D-A-C	0.72	0.96	0.14	0.60	3.59	6.34	2.43	24.23	24.1	0.3	24.1	19.4
	A C-B	0.60	1.42		0.34	2.32	3.12	17.03		24.1	0.3	24.1	20.2

Wetted Surface

<i>Fr</i>	<i>Grids</i>	r_G	p_G (RE)	p_G (LSR)	$ I-C_G $	% U_G GCI	% U_G CF	% U_G mod GCI	% U_G GCI LSR	% U_{SN}	% U_D	% U_V	% E
0.824	D-A-C	3.11	-3.28	0.08	1.68	N.A.	N.A.	N.A.	26.65	26.7	5.0	27.2	20.0
	A C-B	0.13	5.91		5.75	0.04	0.394	2.58		26.7	5.0	27.2	20.3
1.031	D-A-C	-0.41	N.A.	0.02	N.A.	0.85	N.A.	N.A.	52.80	52.8	5.0	53.1	6.4
	A-C-B	-0.77	N.A.		N.A.	0.35	N.A.	N.A.		52.8	5.0	53.1	7.0
1.237	D-A-C	-1.11	N.A.	-0.04	N.A.	N.A.	N.A.	N.A.	16.38	16.5	5.0	17.2	3.9
	A-C-B	-2.12	N.A.		N.A.	N.A.	N.A.	N.A.		16.5	5.0	17.2	9.9
1.443	D-A-C	0.58	1.57	0.20	0.27	4.84	6.00	42.74	27.28	27.3	5.0	27.8	23.5
	A C-B	0.55	1.70		0.20	2.40	2.69	25.04		27.3	5.0	27.8	25.4

Trim

<i>Fr</i>	<i>Grids</i>	r_G	p_G (RE)	p_G (LSR)	$ I-C_G $	% U_G GCI	% U_G CF	% U_G mod GCI	% U_G GCI LSR	% U_{SN}	% U_D	% U_V	% E
0.824	D-A-C	0.76	0.78	0.47	0.69	2.36	4.49	3.64	4.82	4.8	2.3	5.3	10.4
	A C-B	0.83	0.53		0.80	3.00	6.23	14.51		4.8	2.3	5.3	9.9
1.031	D-A-C	0.82	0.57	-0.04	0.78	0.69	1.41	3.02	1.11	3.9	1.8	4.3	10.8
	A-C-B	0.85	0.45		0.83	0.11	1.61	4.47		3.9	1.8	4.3	10.9
1.237	D-A-C	0.20	4.64	0.10	3.00	0.04	0.20	1.78	11.91	12.0	2.0	12.1	9.0
	A-C-B	1.31	-0.78		1.24	N.A.	N.A.	N.A.		12.0	2.0	12.1	9.1
1.443	D-A-C	0.76	0.79	0.10	0.68	1.29	2.45	1.90	10.31	10.6	2.3	10.8	7.7
	A C-B	0.89	0.32		0.88	3.11	6.88	23.80		10.6	2.3	10.8	7.5

C3 model – grid refinement ratio $\sqrt{2}$

Total Resistance Coefficient

<i>Fr</i>	<i>Grids</i>	r_G	p_G (RE)	p_G (LSR)	$ 1-C_G $	% U_G GCI	% U_G CF	% U_G mod GCI	% U_G GCI LSR	% U_{SN}	% U_D	% U_V	% <i>E</i>
0.824	D-A-C	0.81	0.62	0.56	0.76	2.53	5.11	9.43	3.45	3.8	0.3	3.8	4.0
	A C-B	0.85	0.47		0.82	2.91	6.16	16.57		3.8	0.3	3.8	3.6
1.031	D-A-C	0.64	1.28	0.12	0.44	0.67	1.01	3.37	2.90	8.1	0.2	8.1	5.9
	A-C-B	0.65	1.24		0.46	0.45	0.70	2.03		8.1	0.2	8.1	5.7
1.237	D-A-C	0.92	0.23	0.25	0.92	1.41	3.21	12.46	1.22	1.4	0.2	1.4	5.3
	A-C-B	0.92	0.25		0.91	1.19	2.67	10.13		1.4	0.2	1.4	5.2
1.443	D-A-C	0.96	0.11	0.24	0.96	2.63	6.14	27.17	1.13	1.8	0.2	1.8	5.0
	A C-B	0.96	0.13		0.95	2.29	5.34	23.37		1.8	0.2	1.8	4.9

Frictional Resistance Coefficient

<i>Fr</i>	<i>Grids</i>	r_G	p_G (RE)	p_G (LSR)	$ 1-C_G $	% U_G GCI	% U_G CF	% U_G mod GCI	% U_G GCI LSR	% U_{SN}	% U_D	% U_V	% <i>E</i>
0.824	D-A-C	0.73	0.92	0.03	0.62	2.50	4.49	0.55	38.17	56.6	0.7	56.6	5.6
	A C-B	0.53	1.84		0.11	1.37	1.34	0.98		56.6	0.7	56.6	6.1
1.031	D-A-C	0.11	6.42	0.65	7.27	0.06	0.76	0.15	9.70	10.0	0.5	10.1	8.0
	A-C-B	0.71	0.99		0.59	1.23	2.14	1.46		10.0	0.5	10.1	8.3
1.237	D-A-C	0.16	5.21	-0.10	4.09	4.34	9.85	20.60	2.41	2.6	0.4	20.6	14.9
	A-C-B	0.11	6.29		6.86	0.60	1.10	0.19		2.6	0.4	2.7	14.7
1.443	D-A-C	0.73	0.89	0.09	0.64	1.87	3.39	0.12	17.81	17.8	0.4	17.8	24.6
	A C-B	0.85	0.47		0.82	0.96	2.03	5.47		17.8	0.4	17.8	25.2

Wetted Surface

<i>Fr</i>	<i>Grids</i>	r_G	p_G (RE)	p_G (LSR)	$ 1-C_G $	% U_G GCI	% U_G CF	% U_G mod GCI	% U_G GCI LSR	% U_{SN}	% U_D	% U_V	% <i>E</i>
0.824	D-A-C	0.88	0.35	-0.04	0.87	2.96	6.49	21.51	18.65	18.7	5.0	19.4	9.9
	A C-B	0.90	0.31		0.89	2.97	6.58	22.99		18.7	5.0	19.4	10.2
1.031	D-A-C	0.60	1.47	0.14	0.33	2.83	3.77	2.71	31.78	31.8	5.0	32.2	10.0
	A-C-B	0.73	0.90		0.63	3.70	6.69	0.12		31.8	5.0	32.2	11.2
1.237	D-A-C	0.73	0.90	0.02	0.63	1.92	3.48	0.03	25.43	25.5	5.0	26.0	18.1
	A-C-B	-1.61	N.A.		N.A.	N.A.	N.A.	N.A.		25.5	5.0	26.0	17.0
1.443	D-A-C	0.81	0.60	0.06	0.77	5.45	11.06	21.67	34.42	34.4	5.0	34.8	28.3
	A C-B	0.75	0.85		0.66	2.73	5.06	2.01		34.4	5.0	34.8	29.3

Trim

<i>Fr</i>	<i>Grids</i>	r_G	p_G (RE)	p_G (LSR)	$ 1-C_G $	% U_G GCI	% U_G CF	% U_G mod GCI	% U_G GCI LSR	% U_{SN}	% U_D	% U_V	% <i>E</i>
0.824	D-A-C	-0.47	N.A.	-0.01	N.A.	0.87	N.A.	N.A.	5.19	5.2	3.6	6.3	7.6
	A C-B	0.74	0.87		0.65	2.13	3.92	0.83		5.2	3.6	6.3	7.0
1.031	D-A-C	1.26	-0.67	-0.22	1.21	N.A.	N.A.	N.A.	5.01	6.2	2.9	6.9	12.6
	A-C-B	0.31	3.36		1.20	0.14	0.38	0.04		6.2	2.9	6.9	12.8
1.237	D-A-C	0.93	0.22	-0.07	0.92	4.04	9.19	36.16	2.31	1.4	2.6	2.9	11.3
	A-C-B	0.91	0.28		0.90	2.88	6.44	23.51		1.4	2.6	2.9	11.5
1.443	D-A-C	0.83	0.54	-0.07	0.79	2.14	4.43	10.11	2.92	3.7	2.8	4.6	12.5
	A C-B	0.54	1.77		0.15	0.28	0.30	0.21		3.7	2.8	4.6	12.7

C5 model – grid refinement ratio $\sqrt{2}$

Total Resistance Coefficient

<i>Fr</i>	<i>Grids</i>	r_G	p_G (RE)	p_G (LSR)	$ I-C_G $	$\%U_G$ <i>GCI</i>	$\%U_G$ <i>CF</i>	$\%U_G$ <i>mod</i> <i>GCI</i>	$\%U_G$ <i>GCI</i> <i>LSR</i>	$\%U_{SN}$	$\%U_D$	$\%U_V$	$\% E $
0.824	D-A-C	0.86	0.42	0.31	0.84	2.62	5.62	16.51	3.55	16.5	0.5	16.5	7.3
	A C-B	0.86	0.44		0.83	2.12	4.53	12.81		12.8	0.5	12.8	7.0
1.031	D-A-C	0.68	1.13	0.19	0.52	2.11	3.45	6.26	8.36	8.4	0.4	8.4	8.9
	A-C-B	0.72	0.960		0.60	1.83	3.23	1.38		8.4	0.4	8.4	8.4
1.237	D-A-C	0.79	0.68	0.59	0.73	5.04	9.96	14.78	7.25	14.8	0.3	14.8	10.0
	A-C-B	0.78	0.72		0.71	3.63	7.05	8.55		8.6	0.3	8.6	9.3
1.443	D-A-C	0.18	5.02	0.99	3.69	0.24	1.58	12.71	9.87	10.0	0.3	10.0	5.9
	A C-B	0.64	1.27		0.45	1.28	1.95	6.14		10.0	0.3	10.0	5.4

Frictional Resistance Coefficient

<i>Fr</i>	<i>Grids</i>	r_G	p_G (RE)	p_G (LSR)	$ I-C_G $	$\%U_G$ <i>GCI</i>	$\%U_G$ <i>CF</i>	$\%U_G$ <i>mod</i> <i>GCI</i>	$\%U_G$ <i>GCI</i> <i>LSR</i>	$\%U_{SN}$	$\%U_D$	$\%U_V$	$\% E $
0.824	D-A-C	0.86	0.43	0.75	0.84	4.27	9.13	26.20	3.32	3.5	1.0	3.6	10.5
	A C-B	0.95	0.15		0.95	10.65	24.65	15.01		3.5	1.0	3.6	11.1
1.031	D-A-C	0.75	0.83	0.62	0.67	4.70	8.76	4.37	7.75	8.2	0.7	8.2	14.2
	A-C-B	0.29	3.56		1.44	0.43	1.33	14.98		8.2	0.7	8.2	14.6
1.237	D-A-C	-1.02	N.A.	0.53	N.A.	N.A.	N.A.	N.A.	13.97	14.2	0.6	14.2	21.0
	A-C-B	-0.67	N.A.		N.A.	6.90	N.A.	N.A.		14.2	0.6	14.2	22.9
1.443	D-A-C	0.17	5.02	-1.00	3.70	0.36	2.40	10.07	30.05	30.1	0.5	30.1	22.7
	A C-B	0.85	0.45		0.83	5.49	11.70	32.52		30.1	0.5	30.1	24.1

Wetted Surface

<i>Fr</i>	<i>Grids</i>	r_G	p_G (RE)	p_G (LSR)	$ I-C_G $	$\%U_G$ <i>GCI</i>	$\%U_G$ <i>CF</i>	$\%U_G$ <i>mod</i> <i>GCI</i>	$\%U_G$ <i>GCI</i> <i>LSR</i>	$\%U_{SN}$	$\%U_D$	$\%U_V$	$\% E $
0.824	D-A-C	-3.00	N.A.	0.02	N.A.	N.A.	N.A.	N.A.	13.96	14.1	5.0	14.9	14.8
	A C-B	0.20	4.64		3.00	0.02	0.11	0.02		14.1	5.0	14.9	14.9
1.031	D-A-C	-2.11	N.A.	2.20	N.A.	N.A.	N.A.	N.A.	5.81	6.0	5.0	7.8	17.1
	A-C-B	-0.08	N.A.		N.A.	2.325	N.A.	N.A.		6.0	5.0	7.8	16.6
1.237	D-A-C	3.10	-3.26	0.56	1.68	N.A.	N.A.	N.A.	17.35	17.5	5.0	18.2	23.9
	A-C-B	-0.01	N.A.		N.A.	2.26	N.A.	N.A.		17.5	5.0	18.2	23.9
1.443	D-A-C	0.09	6.91	0.22	8.95	0.12	1.83	0.33	36.12	36.1	5.0	36.5	24.1
	A C-B	0.60	1.46		0.34	1.10	1.48	1.06		36.1	5.0	36.5	24.8

Trim

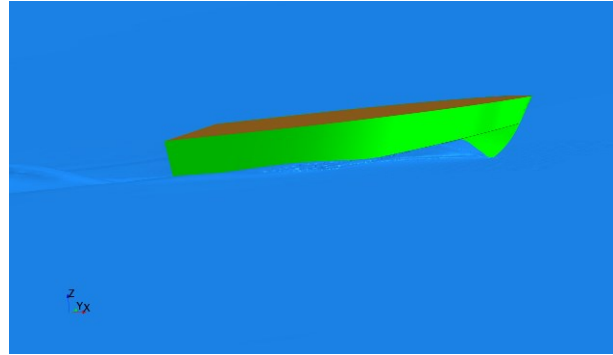
<i>Fr</i>	<i>Grids</i>	r_G	p_G (RE)	p_G (LSR)	$ I-C_G $	$\%U_G$ <i>GCI</i>	$\%U_G$ <i>CF</i>	$\%U_G$ <i>mod</i> <i>GCI</i>	$\%U_G$ <i>GCI</i> <i>LSR</i>	$\%U_{SN}$	$\%U_D$	$\%U_V$	$\% E $
0.824	D-A-C	-0.37	N.A.	-2.87	N.A.	2.56	N.A.	N.A.	15.57	15.6	6.3	15.4	4.8
	A C-B	-0.68	N.A.		N.A.	0.96	N.A.	N.A.		15.6	6.3	16.8	6.0
1.031	D-A-C	0.28	3.64	-5.10	1.54	0.90	2.93	0.47	24.17	24.4	5.8	25.0	8.5
	A-C-B	-1.44	N.A.		N.A.	N.A.	N.A.	N.A.		24.4	5.8	25.0	6.1
1.237	D-A-C	0.42	2.53	-0.84	0.40	2.33	3.36	0.56	29.73	29.7	4.3	30.1	18.4
	A-C-B	0.36	2.96		0.79	0.66	1.36	0.03		29.7	4.3	30.1	19.2
1.443	D-A-C	-1.11	N.A.	-0.05	N.A.	N.A.	N.A.	N.A.	5.00	5.5	3.8	6.6	18.5
	A C-B	-0.51	N.A.		N.A.	0.83	N.A.	N.A.		5.5	3.8	6.6	19.2

U_G was expressed as a percentage value of the simulation solution for the finest grid in the study, *i.e.*, C and B.

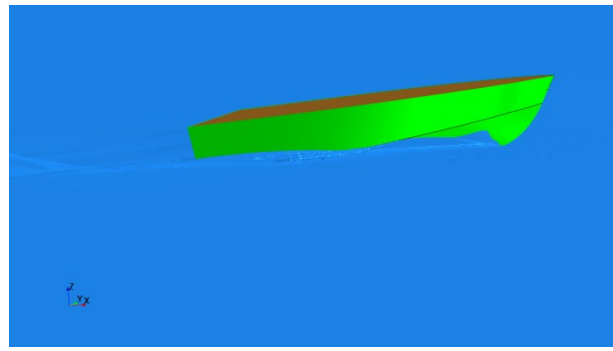
APPENDIX C: C1 model – wave pattern comparison

C1 side photographs compared to CFD simulation at four speeds tested.

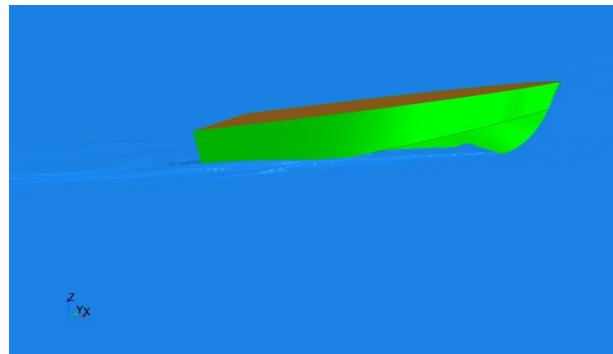
$Fr = 0.824$



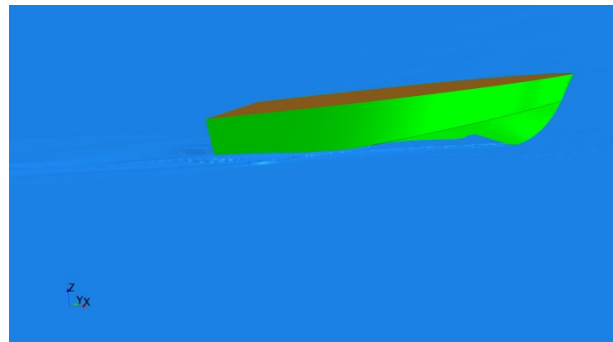
$Fr = 1.031$



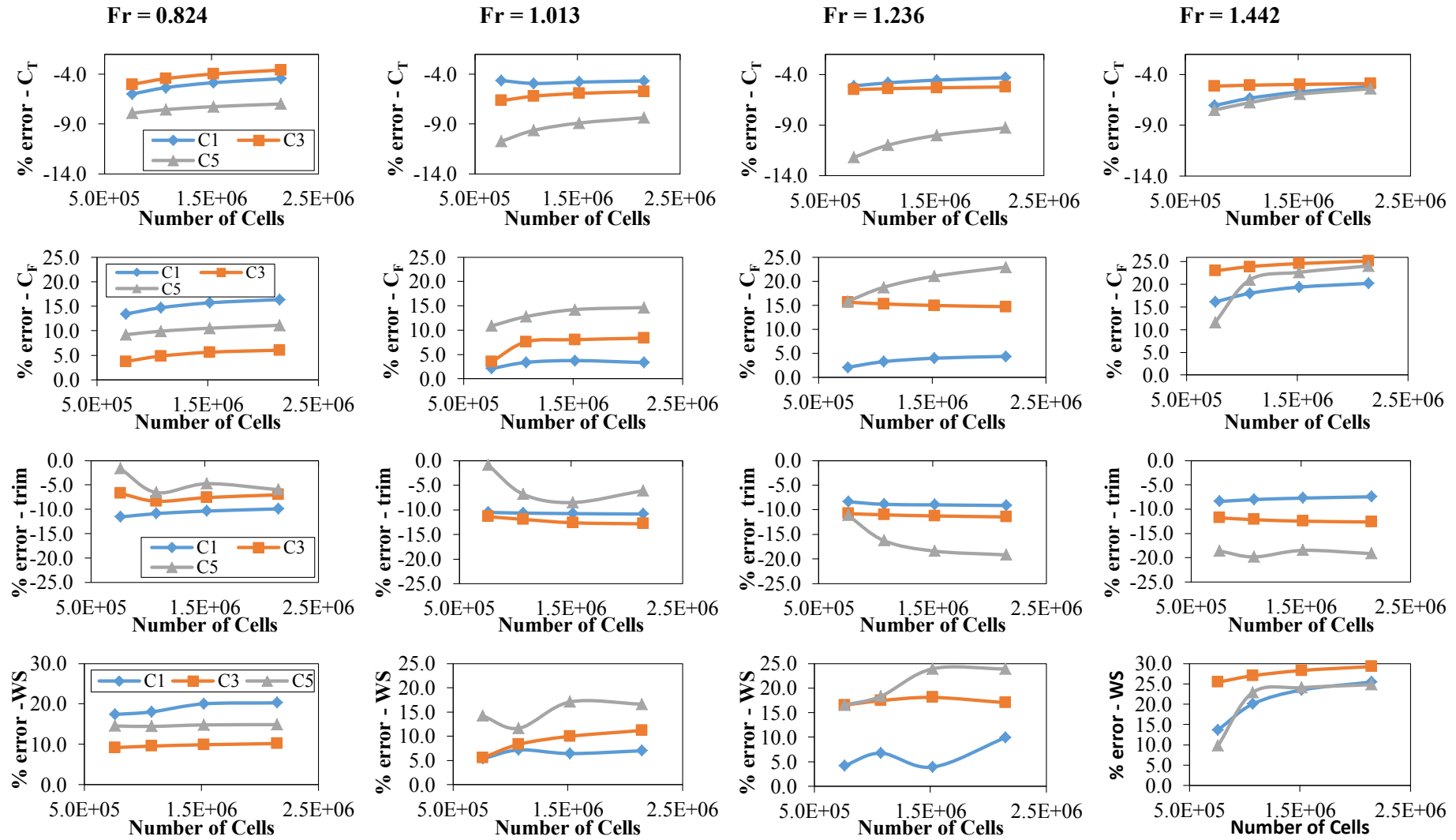
$Fr = 1.237$



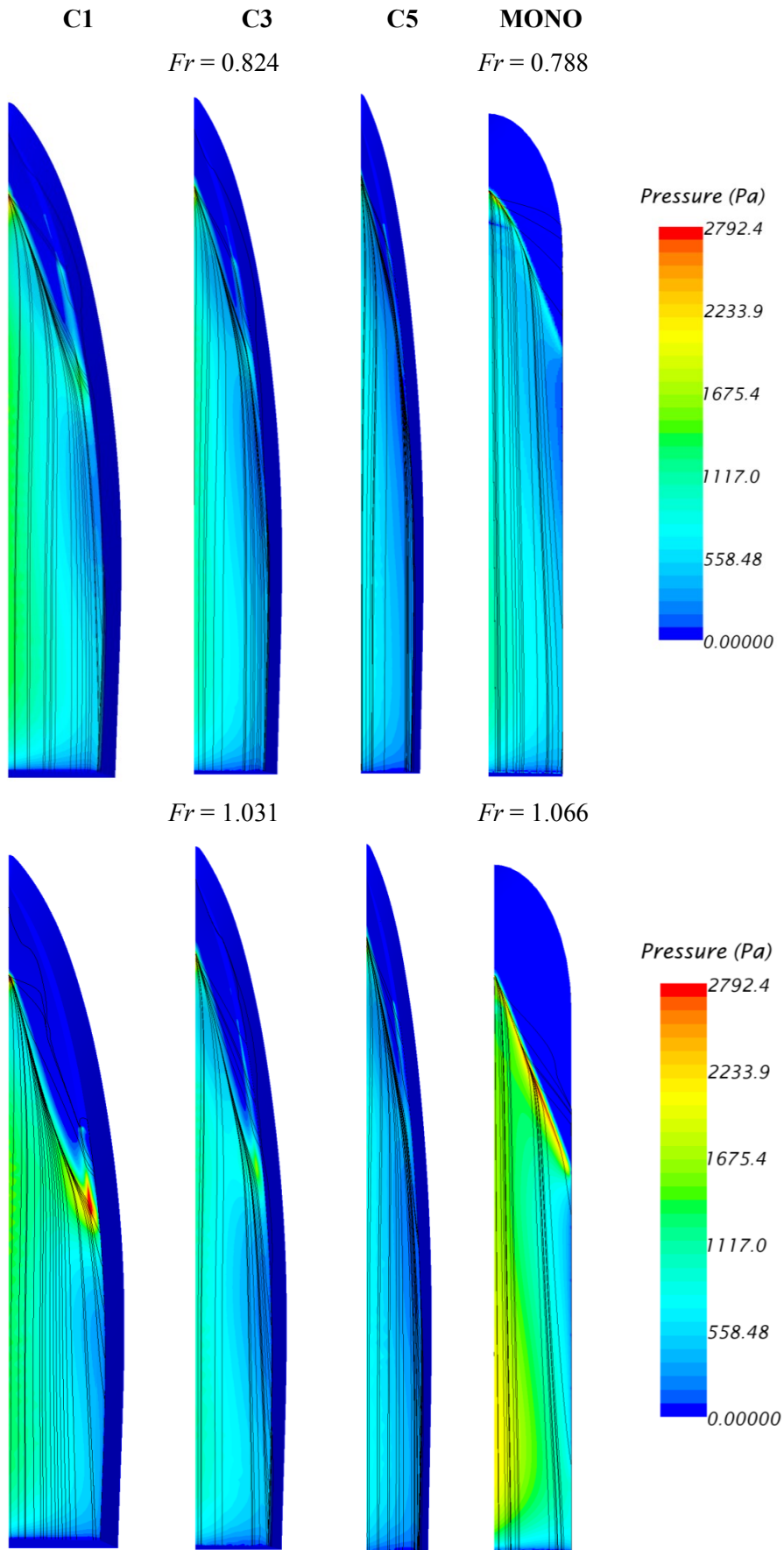
$Fr = 1.443$

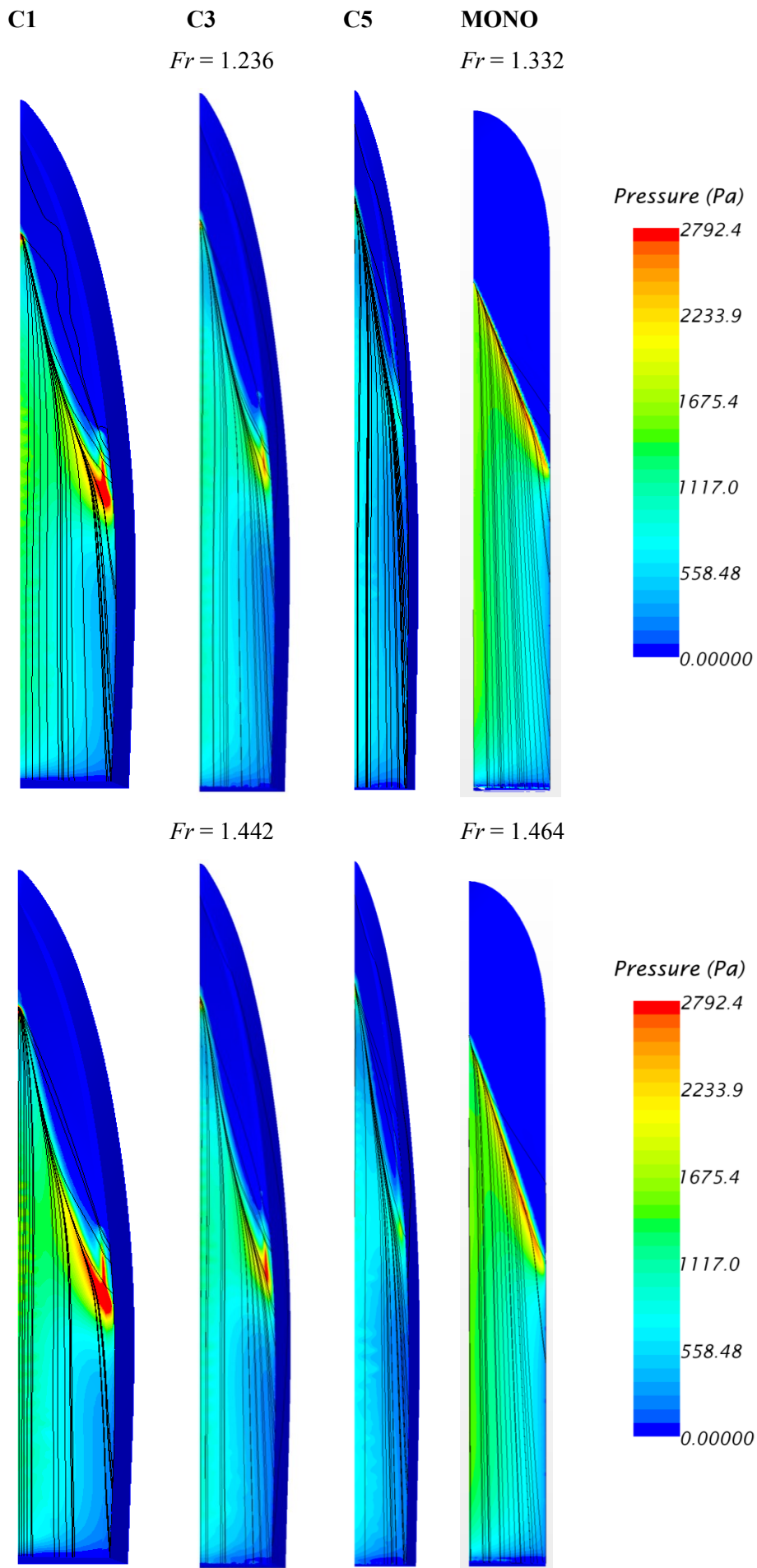


APPENDIX D: Grid independence analysis - percentage error between CFD and EFD data



APPENDIX E: Visualization of streamlines and pressure on the hull bottom





APPENDIX F: Summary of calm water resistance, sinkage and trim CFD V&V studies

Ref.	Geometry	Fr	Grid	Total Resistance			Sinkage			Trim		
				$ E \%D$	$U_{SN}\%S$	$U_D\%D$	$ E \%D$	$U_{SN}\%S$	$U_D\%D$	$ E \%D$	$U_{SN}\%S$	$U_D\%D$
[59]	DTMB 5415	0.28	$3.0 \cdot 10^6$	4.30		0.64	7.40		4.71	10.40		4.70
		0.41		1.50		0.61	1.50		2.93	1.11		0.87
[59], [74]	DTMB 5415	0.28	$1.3 \cdot 10^6$	3.70		0.64	9.50		4.71	2.21		4.70
		0.41		4.50		0.61	4.50		2.93	19.30		0.87
[71]	Athena	0.2 – 1.0	$1.0 \cdot 10^6$	2.10	2.53	1.50	7.70	1.60	29.3	9.60	15.30	8.10
[71]	Propelled appended Athena	0.2 – 0.84	$2.2 \cdot 10^6$	4.50			8.10			5.00		
[75]	HSSL-Delft catamaran	0.2 – 0.65	-	8.00			23.00			17.0		
[76]	Delft catamaran	0.18 – 0.75	$5.4 \cdot 10^6$	5.20			18.50			16.10		
[77]	DTMB 5594	0.511	$1.8 \cdot 10^6$	0.78			0.80			14.30		
[77]	DTMB 5594 self propelled waterjet	0.511	$1.8 \cdot 10^6$	4.60			9.00			13.70		
[78]	JHSS	0.34	$29 \cdot 10^6$	2.20	3.60	5.80	11.60			13.70		
[79]	KVLCC2	0.1	$4.6 \cdot 10^6$	3.45	3.79	0.70						
[2]	KVLCC2	0.143		1.70								
[4]	Surface Combatant Ship	0.50	$1.16 \cdot 10^6$	0.42	4.89							
[64]	SWATH	0.31	$1.32 \cdot 10^6$	4.64	3.32	3.65						
[80]	T-Craft (ACV)	0.2, 0.4, 0.6	$14.7 \cdot 10^6$	7.80	1.50		9.80	8.30		14.70	6.30	
[46]	Series 62 – 20 deg	0.89	$7.9 \cdot 10^6$	0.97	3.9		9.3	1.5		5.1	6.4	

Sources: Stern et al. [1], Mousaviraad et al. [46], and Zou and Larsson [3]

REFERENCES

- [1] F. Stern, J. Yang, Z. Wang, H. Sadat-Hosseini, M. Mousaviraad, S. Bhushan e T. Xing, «Computational Ship Hydrodynamics: Nowadays and Way Forward,» *International Shipbuilding Progress*, pp. 3-105, 2013.
- [2] G2010, «Gothenburg 2010 A Workshop on CFD in Ship Hydrodynamics,» Gothenburg, 2010.
- [3] L. Zou e L. Larsson, «A Verification and Validation Study Based on Resistance Submissions to the Gothenburg 2010 Workshop on Numerical Ship Hydrodynamics,» in *proceedings of 14th Numerical Towing Tank Symposium*, Southampton, 2011.
- [4] F. De Luca, S. Mancini, A. Manfredini, C. Pensa e R. Scognamiglio, «Interceptor Device for a High-Speed Displacing Craft (Comparison Between CFD Simulation and Experimental Data),» in *18th International Conference on Ships and Shipping Research (NAV 2015)*, Lecco, Italy, 2015.
- [5] C. Bertorello, E. Begovic e S. Mancini, «Hydrodynamic Performances of Small Size Swath Craft,» *Brodogradnja Shipbuilding*, vol. 66, n. 4, December 2015.
- [6] ITTC, «Specialist Committee on CFD in Marine Hydrodynamics - 27th ITTC,» 2014.
- [7] W. Sottorf, «Experiments with Planing Surfaces,» 1934.
- [8] W. L. Oberkampf e F. G. Blottner, «Issues in Computational Fluid Dynamics Code Verification and Validation,» *AIAA Journal*, vol. 5, n. 36, pp. 687-695, May 1998.
- [9] F. Stern, R. V. Wilson, H. W. Coleman e E. G. Paterson, «Comprehensive Approach to Verification and Validation of CFD Simulations - Part 1: Methodology and Procedures,» *Journal of Fluids Engineering*, vol. 123, pp. 793-802, December 2001.
- [10] L. L. Green, P. A. Newman e K. Haigler, «Sensitivity Derivatives for Advanced CFD Algorithm and Viscous Modeling Parameters Via Differentiation,» *Journal of Computational Physics*, vol. 125, pp. 313-324, 1996.
- [11] D. Pelletier, E. Turgeon e J. Borggaard, «Sensitivity and Uncertainty Analysis for Variable Property,» in *Proceedings of the 39th AIAA Aerospace Sciences Meeting and Exhibit*, Reno, 2001.
- [12] R. A. Perez, «Uncertainty Analysis of Computational Fluid Dynamics Via Polynomial Chaos,» PhD Thesis, Blacksburg, 2008.

- [13] R. W. Walters e L. Huyse, «Stochastic Methods for Fluid Mechanics - an Introduction,» ICASE, Hampton, 2001.
- [14] M. D. McKay, «Latin Hypercube Sampling as a Tool in Uncertainty Analysis,» *Proceedings of the Winter Simulation Conference*, December 1992.
- [15] J. A. Witteveen, K. Duraisamy e G. Iaccarino, «Uncertainty Quantification and Error Estimation in Scramjet Simulation,» in *Proceedings of 17th AIAA International Space Planes and Hypersonic Systems and Technologies Conference*, 2011.
- [16] J. A. Witteveen e G. Iaccarino, «Simplex Elements Stochastic Collocation for Uncertainty Propagation in Robust Design Optimization,» in *Proceedings of 48th AIAA Aerospace Sciences Meeting Including the New Horizons Forum and Aerospace Exposition*, Orlando, 2010.
- [17] L. Huyse, «Free-Form Airfoil Shape Optimization Under Uncertainty Using Maximum Expected Value and Second-Order Second-Moment Strategies,» ICASE Report 2001-18/NASA CR 2001-211020, 2001.
- [18] R. Ghanem e P. D. Spanos, «Polynomial Chaos in Stochastic Finite Elements,» *Journal of Applied Mechanics*, n. 57, pp. 197-202, March 1990.
- [19] D. Xiu e G. E. Karniadakis, «Modeling Uncertainty in Flow Simulation Via Polynomial Chaos,» *Journal of Computational Physics*, 2001.
- [20] P. Patterson, G. Iaccarino e J. Nordstrom, «Numerical Analysis of the Burgers' Equation in the Presence of Uncertainty,» *Journal of Computational Physics*, vol. 228, n. 22, pp. 8394-8412, 2009.
- [21] ITTC, «Uncertainty Analysis in CFD Verification and Validation 7.5-03-01-01,» 2008.
- [22] F. Stern, R. Wilson e J. Shao, «Quantitative V&V of CFD simulations and certification of CFD codes,» *Int.J.Numer.Methods Fluids*, vol. 50, pp. 1335-1355, 2006.
- [23] C. J. Roy, «Review of Code and Solution Verification Procedures for Computational Simulation,» *Journal of Computational Physics*, n. 205, p. 131–156, 2005.
- [24] P. J. Roache, *Verification and Validation in Computational Science and Engineering*, New Mexico: Hermosa Publishers, 1998.
- [25] P. J. Roache, «Code Verification by the Method of Manufactured Solutions,» *Journal of Fluids Engineering*, vol. 1, n. 124, pp. 4-10, 2002.
- [26] R. Wilson, J. Shao e F. Stern, «Discussion: Criticism of the Correction Factor,» *Journal of Fluids Engineering*, vol. 126, July 2004.

- [27] T. Xing e F. Stern, «Factors of Safety for Richardson Extrapolation,» *Journal of Fluids Engineering*, vol. 132, pp. 061403 1-13, June 2010.
- [28] L. Eça e M. Hoekstra, «Discretization Uncertainty Estimation Based on Least Squares Version of the Grid Convergence Index,» in *2nd Workshop on CFD Uncertainty Analysis*, Lisbon, 2006.
- [29] L. Eça e M. Hoekstra, «A Procedure for the Estimation of the Numerical Uncertainty of CFD Calculations Based on Grid Refinement Studies,» *Journal of Computational Physics*, pp. 104-130, 2014.
- [30] T. Xing e F. Stern, «Comment on “A procedure for the estimation of the numerical uncertainty of CFD calculations based on grid refinement studies” (L. Eça and M. Hoekstra, *Journal of Computational Physics* 262 (2014) 104–130),» *Journal of Computational Physics*, n. 301, pp. 484-486, 2015.
- [31] D. Savitsky, M. F. De Lorme e R. Datla, «Inclusion of Whisker Spray Drag in Performance Prediction Method for High-Speed Planing Hulls,» *Marine Technology*, vol. 44, n. 1, pp. 35-36, 2007.
- [32] E. Begovic e C. Bertorello, «Resistance Assessment of Warped Hullform,» *Ocean Engineering*, n. 56, pp. 28-42, 26 September 2012.
- [33] M. Caponneto, «Practical CFD Simulations for planing Hulls,» in *High Performance Marine Vehicles (HIPER)*, Hamburg, 2001.
- [34] R. Azcueta, «Steady and Unsteady RANSE Simulations for planing Crafts,» in *International Conference on Fast Sea Transportation FAST 2003*, Ischia, 2003.
- [35] V. Anantha Subramanian, P. V. Subramanyam e N. Sulficker Ali, «Pressure and drag influences due to tunnels in high-speed planing craft,» *International Shipbuilding Progress*, vol. 54, pp. 25-44, 2007.
- [36] S. Brizzolara e F. Serra, «Accuracy of CFD Codes in the Prediction of Planing Surfaces Hydrodynamic Characteristics,» in *2nd International Conference on marine Research and Transportation ICMRT 2007*, Ischia, 2007.
- [37] D. Savitsky, «Hydrodynamic design of planing hull,» *Marine Technology*, vol. 1, n. 1, p. 71–95, 1964.
- [38] C. L. Shuford, «A theoretical and Experimental Study of Planing Surfaces Including Effects of Cross Section and Plan Form,» 1956.
- [39] S. Brizzolara e D. Villa, «CFD Simulation of Planing Hulls,» in *Seventh International Conference On High-Performance Marine Vehicles*, Melbourne, Florida, USA, 2010.
- [40] Y. Su, Q. Chen, H. Shen e L. Wei, «Numerical Simulation of a Planing Vessel at High Speed,» *Journal of Marine Science and Application*, vol. 11, pp. 178-183, 2012.

- [41] Y. H. Ozdemir, B. Barlas, T. Baris e S. Bayraktar, «Numerical and Experimental Study of Turbulent Free Surface Flow for a Fast Ship Model,» *Journal of BRODOGRADNJA/SHIPBUILDING*, vol. 65, n. 1, pp. 40-54, 2014.
- [42] P. Ghadimi, S. M. Mirhosseini, A. Dashtimanesh e M. Amini, «RANS Simulation of Dynamic Trim and Sinkage of a Planing Hull,» *Applied Mathematics and Physics*, vol. 1, n. 1, 2013.
- [43] T. C. Fu, K. A. Brucker, S. M. Mousaviraad, M. C. Ikeda, E. J. Lee, T. T. O'Shea, Z. Wang, F. Stern e C. Q. Judge, «An Assessment of Computational Fluid Dynamics Predictions of the Hydrodynamics of High-Speed Planing Craft in Calm Water and Waves,» in *30th Symposium on Naval Hydrodynamics*, Hobart, Tasmania, 2014.
- [44] M. Kandasamy, S. K. Ooi, P. Carrica, F. Stern, E. F. Campana, D. Peri, P. Osborne, J. Cote, N. Macdonald e N. de Wall, «CFD Validation Studies for a High-Speed Foil-Assisted Semi-Planing Catamaran,» *Journal of Marine Science and Technology*, vol. 16, pp. 157-167, June 2011.
- [45] R. Yousefi, R. Shafaghat e M. Shakeri, «Hydrodynamic Analysis Technique for High-Speed Planing Hulls,» *Applied Ocean Research*, vol. 42, pp. 105-113, 2013.
- [46] S. M. Mousaviraad, Z. Wang e F. Stern, «URANS Studies of Hydrodynamic Performance and Slamming Loads on High-Speed Planing Hulls in Calm Water and Waves for Deep and Shallow Conditions,» *Applied Ocean Research*, vol. 51, pp. 222-240, 2015.
- [47] G. Fridsma, «A Systematic Study of the Rough-Water Performance of Planing Boats,» Davidson Laboratory Report 1275, Stevens Institute of Technology, 1969.
- [48] ITTC, «Recommended Procedures and Guidelines 7.5-02-02-01,» 2011.
- [49] ITTC, «Recommended Procedures and Guidelines 7.5-02-02-02,» 2002.
- [50] ITTC, «Recommended Procedures and Guidelines 7.5-01-01-01,» 2002.
- [51] F. De Luca e C. Pensa , «Experimental Investigation on conventional and Unconventional Interceptors,» *Transactions of the Royal institution of Naval Architects - Part B International Journal of Small Craft Technology*, 2012.
- [52] H. K. Versteeg e W. Malalasekera, *An Introduction to Computational Fluid Dynamic The Finite Volume Method*, Longman Scientific & Technical, 1995.
- [53] F. Menter, «Two-equation Eddy-viscosity Turbulence Model for Engineering Applications,» *AIAA Journal*, vol. 30, pp. 2066-2072, 1994.
- [54] CD-Adapco , «STAR CCM+ User's Guide Version 9.06,» 2014.

- [55] J. Wackers, B. Koren, H. C. Raven, A. van der Ploeg, A. R. Starke, G. B. Deng, P. Queutey, M. Visonneau, T. Hino e K. Ohashi, «Free-Surface Viscous Flow Solution Methods for Ship Hydrodynamics,» *Archive of Computational Methods in Engineering*, n. 18, pp. 1-41, 2011.
- [56] C. W. Hirt e B. D. Nichols, «Volume of Fluid (VOF) Method for the Dynamics of Free Boundaries,» *Journal of Computational Physics*, n. 39, p. 201–225, 1981.
- [57] C. Bohm, «A Velocity Prediction Procedure for Sailing Yachts Based on Integrated Fully Coupled RANSE-Free-Surface Simulations,» Delft, 2014.
- [58] O. Ubbink, «Numerical predictions of two fluid systems with sharp interfaces,» 1997.
- [59] S. Muzaferija e M. Peric, «Computation of Free Surface Flows Using Interface-Tracking and Interface-Capturing methods,» in *Nonlinear Water Wave Interaction*, Southampton, WIT Press, 1999.
- [60] V. Andrillion e B. Alessandrini, «A 2D+T VOF Fully Coupled Formulation for Calculation of Breaking Free Surface Flow,» in *Proceedings of the 24th Symposium on Naval Hydrodynamics*, 2003.
- [61] J. Ferziger e M. Peric, *Computational Method for Fluid Dynamics*, Springer-Verlaag, 2003.
- [62] A. Federici, «Design and Analysis of Non-Conventional Hybrid High Speed Hulls with Hydrofoils by CFD Methods,» University of Genoa, Genoa, 2014.
- [63] I. M. Viola, R. G. Y. Flay e R. Ponzini, «CFD Analysis of the Hydrodynamic Performance of Two Candidate America's Cup AC33 Hulls,» *International Journal of Small Craft Technology*, vol. 154, n. B1-B12, 2012.
- [64] P. M. Carrica, R. V. Wilson, R. W. Noack e F. Stern, «Ship Motions Using Single-Phase Level Set with Dynamic Overset Grids,» *Computers & Fluids*, vol. 36, n. 9, pp. 1415-1433, 2007.
- [65] T. Tezdogan, Y. K. Demirel, P. Kellet, M. Khorasanchi e A. Incecik, «Full-Scale Unsteady RANS-CFD Simulations of Ship Behaviour and Performance in Head Seas due to Slow Steaming,» *Ocean Engineering*, n. 97, pp. 186-206, 2015.
- [66] E. Begovic, A. H. Day, A. Inceçik, S. Mancini e D. Pizzirusso, «Roll Damping Assesment of Intact and Damaged Ship by CFD and EFD Methods,» in *Proceedings of the 12th International Conference on the Ship Stability of Ship and Ocean Vehicles*, Glasgow, 2015.
- [67] A. Swidan, W. Amin, D. Ranmuthugala, G. Thomas e I. Penesis, «Numerical Prediction of Symmetric Water Impact Loads on Wedge Shaped Hull Form Using CFD,» *World Journal of Mechanics*, n. 3, pp. 311-318, Novemeber 2013.

- [68] J. Y. Kang e B. S. Lee, «Mesh-Based Morphing Method for Rapid Hull Form Generation,» *Computer-Aided Design*, n. 42, pp. 970-976, 2010.
- [69] M. E. Biancolini e I. M. Viola, «Sails Trim Optimisation Using CFD and RBF Mesh Morphing,» *Computers & Fluids*, n. 93, p. 46–60, 2014.
- [70] A. de Boer, M. S. Schoot e H. Bijl, «Mesh Morphing Based on Radial Function Interpolation,» *Computers and Structures*, vol. 85, pp. 784-795, 2007.
- [71] M. E. Biancolini, *Mesh Morphing and Smoothing by Means of Radial Basis Functions (RBF): A Practical Example Using Fluent and RBF Morph*, IGI Global, 2012.
- [72] F. De Luca, S. Mancini, C. Pensa e G. Staiano, «Numerical evaluation (CFD) of Wake and Thrust deduction fraction of a Warped Hard Chine Hulls Systematic Series,» in *10th High Speed Marine Vehicles Symposium (HSMV 2014)*, Naples, Italy, 2014.
- [73] ITTC, «Recommended Procedures and Guidelines 7.5-03-02-03,» *Practical Guidelines for Ship CFD Applications*, 2011.
- [74] ITTC, «Recommended Procedures and Guidelines 7.5-03-02-03,» 2011.
- [75] D. Savitsky e M. Morabito, «Surface Wave Contours Associated With the Forebody Wake of Stepped Planing Hulls,» *Marine Technology*, vol. 47, n. 1, pp. 1-16, January 2010.
- [76] T. Xing, P. Carrica e F. Stern, «Computational Towing Tank Procedures for Single Run Curves of Resistance and Propulsion,» *Journal of Fluids Engineering*, vol. 130, pp. 101102 1-14, 2008.
- [77] R. V. Wilson, F. Stern, H. W. Coleman e E. G. Paterson, «Comprehensive Approach to Verification and Validation of CFD Simulations - Part 2: Application for RANS Simulation of a Cargo/Container Ship,» *Journal of Fluids Engineering*, vol. 123, pp. 803-810, 2001.
- [78] M. Hoekstra, L. Eça, J. Windt e H. C. Raven, «Viscous Flow Calculations for KVLCC2 AND KCS Models Using the PARNASSOS Code,» in *Proceedings Gothenburg 2000 "A Workshop on Numerical Ship Hydrodynamics"*, Gothenburg, 2000.
- [79] M. G. Morabito, «Empirical Equations for Planing Hull Bottom Pressures,» *Journal of Ship Research*, vol. 58, n. 4, pp. 185-200, 2014.
- [80] S. Pennino, S. Mancini, E. Begovic, H. Klymenko e A. Scamardella, «Three-dimensional Pressure Distribution on Planing Hulls,» in *Proceedings of 3rd International Conference on Maritime Technology and Engineering*, Lisbon, 2016.

- [81] T. Xing, P. Carrica e F. Stern, «Developing Streamlined Version of CFDShip-Iowa-4.5,» IIHR, 2011.
- [82] F. Stern, P. Carrica, M. Kandasamy, J. Gorski, J. O'Dea, M. Hughes, R. Miller, D. Kring, W. Milewski, R. Hoffman e C. Cary, «Computational Hydrodynamic Tools for High-Speed Sealift,» *Transactions of The Society of Naval Architects and Marine Engineers*, vol. 114, pp. 55-81, 2007.
- [83] T. Castiglione, F. Stern, S. Bova e M. Kandasamy, «Numerical Investigation of the Seakeeping Behavior of a Catamaran Advancing in Regular Head Waves,» *Ocean Engineering*, vol. 38, n. 16, pp. 1806-1822, 2011.
- [84] M. Kandasamy, S. K. Ooi, P. Carrica e F. Stern, «Integral Force/Moment Waterjet Model for CFD Simulations,» *Journal of Fluids Engineering*, vol. 132, n. 10, p. 9 pp, 2010.
- [85] T. Takai, M. Kandasamy e F. Stern, «Verification and Validation Study of URANS Simulations for an Axial Waterjet Propelled Large High-Speed Ship,» *Journal of Marine Science and Technology*, vol. 16, n. 4, pp. 434-447, 2011.
- [86] F. Ismail, P. Carrica, T. Xing e F. Stern, «Evaluation of linear and nonlinear convection schemes on multidimensional non-orthogonal grids with applications to KVLCC2 tanker,» *International Journal Numerical Methods Fluids*, vol. 64, pp. 850-886, 2010.
- [87] S. Bhushan, P. Carrica, J. Yang e F. Stern, «Verification and Validation for Captive Model-Scale Surface Effect Ship Resistance, Seakeeping and Maneuvering,» *Applied Ocean Research*, 2015.
- [88] ITTC, «Guidelines for Uncertainty Analysis in Resistance Towing Tank Tests,» in *Recommended Procedure and Guidelines*, 2008.
- [89] M. D. Coleman D.E., «A systematic approach to planning for a design industrial experiment,» vol. 35, 1993.
- [90] J. Wackers, «Surface capturing and multigrid for steady free-surface water flows,» PhD Thesis, Delft University of Technology, 2007.
- [91] P. Gallagher, C. Berhault, R. Marcer, C. de Jouette, H. C. Raven, L. Eça, L. Broberg, C. E. Janson, Q. X. Gao, S. Toxopeus, B. Alessandrini, T. van Terwisga, M. Hoekstra, H. Streckwall e F. Salvatore, «Best Practice Guidelines for the application of Computational Fluid Dynamics in Marine Hydrodynamics,» VIRTUE - The Virtuel Tank Utility in Europe, 2009.
- [92] I. B. Celik, U. Ghia, P. J. Roache, C. J. Freitas, H. Coleman e P. E. Raad, «Procedure for estimation and reporting of uncertainty due to discretization in CFD applications,» vol. 130, 2008.

- [93] T. Xing e F. Stern, «Comment on “A procedure for the estimation of the numerical uncertainty of CFD calculations based on grid refinement studies” (L. Eça and M. Hoekstra, *Journal of Computational Physics* 262 (2014) 104–130),» *Journal of Computational Physics*, n. 301, pp. 484-486, 2015.
- [94] R. Azcueta, «Steady and Unsteady RANSE Simulations for planing Crafts,» in *International Conference on Fast Sea Transportation FAST 2003*, Ischia, 2003.
- [95] S. Brizzolara e F. Serra, «Accuracy of CFD Codes in the Prediction of Planing Surfaces Hydrodynamic Characteristics,» in *2nd International Conference on marine Research and Transportation ICMRT2007*, Ischia, 2007.
- [96] M. Haase, F. Iliopoulos, G. Davidson, S. Friezer, G. Thomas, J. Binns e M. R. Davis, «Application of RANSE-based simulations for resistance prediction of medium-speed catamarans at different scales,» in *18th Australasian Fluid Mechanics Conference*, 2012.
- [97] M. Caponnetto, «Practical CFD Simulations for planing Hulls,» in *High Performance Marine Vehicles (HIPER)*, Hamburg, 2001.
- [98] R. Azcueta, M. Caponnetto e H. Soding, «Motion simulations for planing boats in waves,» *Ship Technology Research / Schiffstechnik*, vol. 4, n. 50, pp. 182-198, 2003.
- [99] ITTC, «Recommended Procedures 7.5-01-01-01,» 2002.

FIGURES INDEX

Figure 1 (a) Visualizations of Surface Combatant Ship, source: De Luca et al. [4]; and (b) SWATH hull, source: Begovic et al. [5].....	7
Figure 2 Simulation workflow with sources of error	9
Figure 3 Examples of discretization by the MC and SC methods, source: Witteveen et al. [16]	14
Figure 4 Forces applied on the flat plate.....	25
Figure 5 Transversal flow on the flat plate	26
Figure 6 The projected area of a planing hull, source: Savitsky [31].....	26
Figure 7 (a) The projected area of a planing hull, source: Begovic et al. [32]; (b) Blisters spray visualization	27
Figure 8 Comparison errors for whole Fr-range and for the finest grid used ($16.9 \cdot 10^6$ cells), source: Mousaviraad et al. [44].....	29
Figure 9 Transversal and longitudinal sections of the C1 model	30
Figure 10 The five models of NSS	31
Figure 11 Towing Tank of Naval division of DII	31
Figure 12 The profiles of Systematic Series DIN models, source: Begovic et al. [24]	33
Figure 13 Example of structured (green) and unstructured (blue) mesh	37
Figure 14 Time Step Setup	39
Figure 15 Gothenburg Workshop 2010 – free surface models in the widely used CFD codes, source: Bohm [57].....	40
Figure 16 Visualization of air and water volume fractions and related free-surface, source: CD-Adapco User’s Guide [54].....	41
Figure 17 Upwind, downwind, and central cells that are used in the analysis	42
Figure 18 The NVD with the linear schemes: Central Differencing (CD) and Linear Upwind Differencing (LUD): the shaded area shows the zone for which the CBC is valid.	43
Figure 19 Example of numerical ventilation problem on the bottom of the planing hull	45
Figure 20 Workflow of rigid body motion.....	47
Figure 21 Resistance test simulation of planing hull using moving grid with free-surface and mesh visualization	48
Figure 22 Schematic drawing of the free surface perturbation and “fake-wave” due to the moving grid for inlet boundary, source: Viola et al. [63]	48
Figure 23 The overset/chimera grid with the two regions: moving region (overset) and stationary region (background)	49
Figure 24 Particular of overset region in two different test cases: (a) Roll damping assessment [52] and (b) resistance in still water for SWATH hull [50]	50
Figure 25 Connectivity between the background and the overset regions, source:	51

Figure 26 Examples of application of smoothing/morphing mesh in marine hydrodynamics application: (left) sail yacht, source: Bohm [45]; (right) planing hull simulation.....	52
Figure 27 Summary of the tests for the modelling analysis	54
Figure 28 Morphing and moving grid case. Front (left) and side (right) view of the dimensions of the domain (L is waterline length of the ship).....	56
Figure 29 Boundary conditions for the morphing and moving grid cases.....	57
Figure 30 Overset grid: Front (left) and side (right) view of the dimensions of the domain (B: half beam of the ship, L: waterline length of the ship, D: height of the ship)	57
Figure 31 General view of OG Case of the two regions with the boundary conditions	58
Figure 32 The background and overset regions with polyhedral (unstructured) mesh and trimmed (structured) mesh respectively.....	58
Figure 33 Comparison of CFD free surface elevation and centerline free surface profile evaluated according to Savitsky and Morabito [75].....	59
Figure 34 Calculation time required for the different moving mesh techniques	61
Figure 35 Percentage comparison errors between CFD simulation and EFD for the different configurations that are tested.....	62
Figure 36 Percentage comparison errors between CFD simulation and EFD for the different overset interpolation schemes that are analyzed	63
Figure 37 Calculation time required for the different interpolation schemes	64
Figure 38 Percentage comparison errors between CFD simulation and EFD for the different overset interpolation schemes that are analysed (C1 model).....	65
Figure 39 Representation of the VOF on the bottom hull of the C1 model for the different VOF schemes examined for the OG-TP grid case: (a) HRIC scheme with artificial suppression of air mass fraction, (b) HRIC scheme without dependence on the local CFL number, (c) HRIC scheme with dependence on the local CFL number	66
Figure 40 Percentage comparison errors between CFD simulation and EFD data for the two different turbulence models	67
Figure 41 Summary of the tests for the numerical analysis	69
Figure 42 Example of graphical assessment of iterative convergence analysis for C_T	70
Figure 43 Time-step uncertainty for the different response variables on the C1 model.....	71
Figure 44 Ranges of wall y^+ values for the models at $Fr = 1.442$ at on grid cases D and B: (a) C5 model, (b) C3 model, and (c) C1 model.....	73
Figure 45 Grid uncertainty values for the different models tested, for the GCI, CF and modified GCI the values reported are a mean between the two studies: D-A-C and A-C-B	74
Figure 46 Grid uncertainties for C_T evaluated by LSR-GCI method for the different hull models	75
Figure 47 Example of time history of the drag of the C1 model at $Fr = 1.443$	75
Figure 48 Statistical errors of the response variables for the different models and the different Fr tested	76

Figure 49 Validation uncertainty (bars) and comparison error (dashed lines) for the different models that were tested, the uncertainties were evaluated using the LSR-GCI method..... 77

Figure 50 (a) Average comparison error and (b) average validation uncertainty for the three models that are tested 78

Figure 51 The U_{SN} percentage compositions 79

Figure 52 Visualization of wave cut length and position 80

Figure 53 Visualization of EFD (up) and CFD (down) stagnation line at $Fr = 1.237$ 82

Figure 54 Comparison of the wave profiles for EFD and CFD data for the four different grids at different Fr values 83

Figure 55 Visualization of extended wave cut length 84

Figure 56 Effect of the extension wake-refinement mesh on the capturing of the wave 84

Figure 57 Comparison of the extended wave profiles for EFD and CFD data for the Case B and..... 85

Figure 58 (a) Grid uncertainty and (b) comparison error for morphing mesh case at $Fr = 1.031$ 87

Figure 59 Grid, simulation, and validation uncertainty (bars) and comparison error (dashed line) for the C1 model at $Fr = 1.031$ 87

Figure 60 Comparison of the wave profile at $Fr = 1.031$ of morphing and modified-OG cases 88

Figure 61 Profile of MONO hull of SS-DIN 88

Figure 62 Percentage comparison errors between EFD and CFD data for the SS-DIN MONO model at four Fr and four grids tested..... 89

Figure 63 Validation uncertainty (bars) and comparison error (lines) for the MONO hull 90

Figure 64 Comparison errors and grid uncertainty of C5 and MONO hull for the finest grid at the respectively four Fr 91

TABLE INDEX

Table 1 Main data of the five models of NSS	31
Table 2 Towing point positions for the three models that are analyzed; T_H is the distance between the towing point and the base line; T_L is the longitudinal position equal to the longitudinal position of center of buoyancy (LCB).....	32
Table 3 Main data of the SS-DIN models, source: Begovic et al. [24]	34
Table 4 Pros and cons of the structured and unstructured mesh type, source CD-Adapco User's Guide [54]38	
Table 5 Pros and cons of the overset and morphing mesh, source CD-Adapco User's Guide [54].....	53
Table 6 Grid base size dimension and total number of cells for the four different configurations of the grids that are tested.....	55
Table 7 Summary of the numerical simulation setup	61
Table 8 Results of simulations with different moving mesh solutions	62
Table 9 Results of OG-TP simulations with different interpolation schemes.....	64
Table 10 Results of OG-TP simulations with different VOF schemes.....	66
Table 11 Iterative convergence study for the C1 model and one grid case at different Fr values.....	70
Table 12 Base size and total number of cells of the grids that were examined	72
Table 13 Average values of wall y^+ on the hull for the coarsest and finest grids	72
Table 14 Profile-averaged values from wave profiles in the V&V study (all of the percentage values is referred to ζ_{\max} , <i>i.e.</i> the maximum value for each wave profile)	82
Table 15 C1 morphing case: base size and total number of cells of the five grids that are examined	86
Table 16 MONO hull: base size and total number of cells of the four grids that are examined	89

ACRONYMS

In the following table, expansions of the acronyms used in the work are presented.

ACV	Air Cushion Vehicles
AMG	Algebraic Multi-Grid
CBC	Convection Boundedness Criterion
CD	Central Differencing
CF	Correction Factor
CFD	Computational Fluid Dynamic
CFL	Courant Friedrichs Lewy Number
CICSAM	Compressive Interface Capturing Scheme for Arbitrary Meshes
DFBI	Dynamic Fluid Body Interaction
DII	Dipartimento d'Ingegneria Industriale
DIN	Dipartimento d'Ingegneria Navale
DNS	Direct Navier Stokes
DOF	Degrees of Freedom
EFD	Experimental Fluid Dynamics
FOFM	First Order First Moment
FOSM	First Order Second Moment
FVM	Finite Volume Method
GCI	Grid Convergence Index
HRIC	High-Resolution Interface Capturing
HSC	High Speed Craft
ITTC	International Towing Tank Conference
LES	Large Eddy Simulation
LHS	Latin Hypercube Sampling
LSR	Least Square Root
LUD	Linear Upwind Differencing
MC	Monte Carlo
MG	Moving grid
MHG	Morphing Grid
NS	Navier - Stokes
NSS	Naples Systematic Series
NV	Numerical Ventilation
NVD	Normalized Variable Diagram
OG	Overset Grid
OG-TP	Overset Grid Trimmed – Polyhedral
OG-TT	Overset Grid Trimmed – Trimmed
PDE	Partial Differential Equation
PDF	Probability Density Function
(U)RANS	(Unsteady) Reynolds Average Navier Stokes
RBF	Radial Basis Functions
RE	Richardson Extrapolation
SC	Stochastic Collocation

SIMPLE	Semi Implicit Method for Pressure Linked Equations
SS-DIN	Systematic Series DIN
UD	Upwind Differencing
V&V	Verification and Validation
VOF	Volume of Fluid

NOMENCLATURE

In the following tables, the nomenclature used in this work is explained.

Greek Symbols

α		Volume fraction
β	[deg]	Deadrise angle
δ_I		Iteration error
δ_{ij}		Kronecker delta
δ_G		Grid error
δ_{SM}		Modelling error
$\delta_{SN}, \delta_{SN}^*$		Simulation error, corrected
δ_P		Other sources error
δ_{RE}		Error evaluated by generalized RE method
δ_{TS}		Time-step error
Δ	[kg]	Displacement
∇	[m ³]	Volume
ε_{ij}		Solution change
ζ		Wave height value
φ		General flow variable
μ	[kg/m s]	Dynamic viscosity
μ_t	[m ² /s]	Turbulent viscosity
ν	[m ² /s]	Kinematic viscosity
ρ	[kg/m ³]	Density
ξ		Normalized flow variable
τ	[deg]	Dynamic trim
τ_s	[deg]	Static trim
ω	[rad]	Angular velocity

Roman symbols and dimensionless numbers

B_{WL}	[m]	Maximum waterline breadth
C_F		Frictional resistance coefficient:
C_k		Correction factor
C_T		Total resistance coefficient:
C_V		Speed coefficient
D		Experimental data
E		Comparison error
Fr, Fr_V		Froude Number, volumetric
F_S		Factor of safety
H	[m]	Height of refinement of air-water interface
H_1	[m]	Stern wake height
I		Inertia moment tensor
L	[N]	Hydrodynamic lift force
L/B		Length – beam ratio
LCB	[m]	Longitudinal position of center of buoyancy
LCG	[m]	Longitudinal position of centre of gravity
LCP	[m]	Longitudinal position of center of pressure
L_K	[m]	Wetted keel length
$L2$		norms $\ x\ _2 = \left(\sum_{k=1}^N x_k^2 \right)^{1/2}$
L_{OA}	[m]	Length overall
L_{WL}	[m]	Waterline length
$L/V^{1/3}$		length-displacement ratio
m	[kg]	mass
n_g		Number of grids
p_k		Estimated order of accuracy
p_{th}		Theoretical order of accuracy
k		Turbulent kinetic energy
Re		Reynolds number
r_K		Constant refinement ratio
R_F	[N]	Frictional resistance
R_x	[N]	Longitudinal component of the integral of the pressures
R_y	[N]	Vertical component of the integral of the pressures
R_t	[N]	Tangent plate component of the integral of the pressures

R_k		Convergence ratio
R_T	[N]	Total resistance
R_V	[N]	Viscous resistance
U		Uncertainty
U_{SN}, U_{SN}^*		Simulation uncertainty, corrected
U_D		Experimental data uncertainty
U_V, U_V^*		Validation uncertainty, corrected
U_G		Grid uncertainty
U_I		Iteration uncertainty
U_{TS}		Time-step uncertainty
U_P		Other sources uncertainty
V		Reynolds averaged flow velocity vector
V	[m/s]	Hull speed
q		Richardson extrapolation constant
S		Simulation result
S_W	[m ²]	Dynamic wetted surface
S_{WS}	[m ²]	Static wetted surface
S_U		Maximum value for simulation result
S_L		Minimum value for simulation result
T		Truth
T_H	[m]	Vertical towing point position
T_L	[m]	Longitudinal towing point position
T_{AP}	[m]	Draft at aft perpendicula
\mathbf{T}_{Re}		Reynolds Stresses Tensor
W	[N]	Weight force
y^+		Dimensionless wall distance

ACKNOWLEDGEMENTS

I would like to express my deepest gratitude to my tutor, Prof. Claudio Pensa, for his excellent guidance, caring, patience, and providing me with an excellent atmosphere for doing research. My sincere thanks go to Prof. Ermina Begovic for her encouragement, comments, and research opportunities, which have allowed me to try my hand in different and interesting areas.

I would like to thank Prof. Agostino De Marco, Prof. Salvatore Miranda, and Eng. Fabio De Luca (researcher) for helping me to develop my background in experimental and numerical hydrodynamic.

I would also like to thank all the others Professors of the naval section of DII of the Università degli Studi di Napoli "Federico II" (in particular: Prof. Flavio Balsamo, Prof. Carlo Bertorello, Prof. Ernesto Fasano, and Prof. Franco Quaranta) for all the support and opportunities provided to me.

Finally, I would like to thank my girlfriend, Maria De Carlini. She was always there cheering me up and stood by me through the good times and bad.

I wish to acknowledge the following organizations:

The Italian Navy for providing me with the opportunity to attend the PhD course and the SCoPE academic staff for the given support and the availability of 64 processors at high performance computing Centre SCoPE of Università degli Studi di Napoli "Federico II"

Page Left Intentionally Blank